Double-Sided Arc Welding of AA5182 Sheet in the Lap-Joint Configuration

by

Nandan S. Joshi

A thesis

presented to the University of Waterloo

in fulfillment of the

thesis requirement for the degree of

Master of Applied Science

in

Mechanical Engineering

Waterloo, Ontario, Canada, 2010

AUTHOR'S DECLARATION

I hereby declare that I am the sole author of this thesis. This is a true copy of the thesis, including any required final revisions, as accepted by my examiners.

I understand that my thesis may be made electronically available to the public.

Abstract

Automakers are increasingly using aluminum for structural applications in order to reduce vehicle weight and improve fuel efficiency. However, aluminum bodied cars have largely been confined to lower-volume, niche markets due in part to the number of challenges associated with welding of aluminum in comparison with steel. Therefore, a need exists for new joining processes which can produce high-quality welds in thin aluminum sheet at high production rates and low cost. The recently invented double-sided arc welding (DSAW) process is one such joining process. It has been shown to be capable of producing high quality butt-joint configuration welds in thin aluminum sheet and thick steel plate. In DSAW, an arc is initiated across two torches that are mounted on either side of the workpiece, allowing it to be welded from both sides. The objective of this research was to determine the feasibility and merits of using the DSAW process to produce seam and spot welds in thin aluminum sheet in the lap-joint configuration.

The double-sided arc welding (DSAW) apparatus used in the present study was powered by a single square wave alternating current variable polarity power supply to produce an arc across two liquid cooled, plasma arc welding torches. This equipment was used to produce a series of conduction-mode DSAW seam and spot welds in 1 mm thick and 1.5 mm thick AA5182-O and AA6111 sheet in the lap-joint configuration. Metallographic analysis was used to characterize the microstructure of the welds, while microhardness and tensile tests were used to characterize the mechanical properties.

Since hydrogen is easily absorbed by molten aluminum, all weld specimens must be cleaned prior to welding in order to produce high quality, pore-free welds. Although previous studies had shown that the specimens could be sufficiently cleaned by degreasing and wire brushing them prior to welding, this cleaning procedure was not found to be adequate for the specimens used in this study

and a more aggressive cleaning technique was required. A number of different specimen pre-cleaning techniques were examined, and a combination of degreasing, deoxidizing, and manual wire brushing was found to produce the least amount of porosity in bead-on-plate welds produced in 1.5 mm thick AA5182-O sheet. Further reductions in porosity were accomplished by redesigning the shielding gas cup of the top Thermal Arc torch to promote more laminar gas flow and generate a more evenly distributed shielding gas plume. Using the redesigned shielding gas cup, a shielding gas flow rate of 10 lpm was found to provide good coverage of the weld pool and produce virtually pore-free welds.

The feasibility of using the DSAW process to produce spot welds in 1 mm thick AA5182-O sheet in the lap-joint configuration was examined by producing a series of spot welds over a range of welding powers and weld times. Weld nuggets were produced using a welding current as low as 50 A with a cycle time of one second. However, all of the welds exhibited a pinhole at the centre of the nugget which penetrated through the entire thickness of the specimen, regardless of welding current and cycle time used. Solidification shrinkage porosity and crater cracking were also observed near the centerline of the welds. Hydrogen gas porosity and oxide tails were also observed in the welds. These defects were found to decrease the strength and quality of the spot welds made between 1 mm thick AA5182-O sheets in the lap-joint configuration.

A series of welds were made to determine if the DSAW process could be used to produce seam welds in 1 mm thick AA5182-O sheet in the lap-joint configuration. Visually acceptable, crack-free welds were produced using welding powers ranging from 2.0 kW to 5.1 kW, at welding speeds between 10 mm/s and 70 mm/s. Welds produced within this range of welding conditions were found to possess excellent cathodic cleaning on both sides of the workpiece, a smooth weld bead, and a columnar-to-equiaxed grain transition. However, transverse cross-sections of the specimens revealed varying amounts of oxide entrainment in the weld metal which was seen most frequently as unbroken interface oxide sheets or tails at the fusion boundaries. Often times, small clusters of porosity were

found to nucleate along the oxide tails. This suggested that there was insufficient fluid flow in the weld to disrupt the pre-existing oxide sheets at the interface between the sheets. Careful specimen pre-cleaning using a combination of degreasing, deoxidizing, and manual stainless steel wire brushing was found to reduce, but not eliminate the oxide tails. Microhardness testing revealed that the microhardness was relatively consistent across the weld metal, heat-affected zone (HAZ), and base metal. In a series of tensile-shear tests, all of the welded specimens were observed to fail in the weld metal, within 1 mm of the fusion boundary.

Another series of seam welds were produced between 1 mm thick AA6111 and 1 mm thick AA5182 sheets in the lap-joint configuration to explore the nature and intensity of fluid flow in the molten weld pool responsible for breaking oxide tails. The difference in magnesium content between the two alloys produces a different microstructure and response to chemical etching, thereby revealing any effects of fluid motion in the weld pool. Relatively weak buoyancy driven fluid flow was observed when the AA6111 sheet was placed on top of the AA5182 sheet, and some minor stirring was seen between the two sheets. When the slightly less dense AA5182 sheet was placed above the AA6111 sheet, very little fluid flow was observed and the two alloys remained unmixed. Overall, the weld pool formed during DSAW was found to be very quiescent. This suggests that the normally strong Marangoni and Lorentz force induced flow seen in other arc welding processes does not occur in the double-sided arc weld pool. This leaves only a very weak buoyancy driven fluid flow which is incapable of disrupting the pre-existing oxide at the interface between the sheets immediately adjacent to the fusion zone boundary.

Overall the DSAW process was found to be capable of producing visually acceptable lap-joint configuration seam welds in AA5182-O sheet over a wide range of welding speeds and welding powers, provided that the pre-existing oxide and any other surface contaminants were chemically removed prior to welding.

Acknowledgements

I would like to thank my supervisor, Dr. D. Weckman for the guidance that he provided while conducting the research for this project and while writing this thesis. I would also like to thank my fellow graduate students for providing me with advice over the last two years. Financial support for this project was provided by the Natural Sciences and Engineering Research Council of Canada (NSERC).

Dedication

Dedicated to my parents and my sister, for providing me with support and encouragement over the last two years while working on this project.

Table of Contents

List of Figures

List of Tables

Chapter 1: Introduction

As regulatory pressure and consumer demand for more fuel-efficient vehicles increases, automakers will require new technologies and materials that will allow them to improve mileage without sacrificing safety, comfort, or performance. One method for improving fuel economy and performance is to reduce the weight of the vehicle. In an average steel-bodied car, the body-in-white (BIW) accounts for 27% of the vehicle's total mass [1]. For example, by using aluminum instead of steel, Jaguar Cars Ltd., a manufacturer of luxury cars, has reduced the weight of the BIW for the XJ Series by 40% while improving stiffness by 60% compared to the older steel-bodied model [2], [3]. Fuel economy is also expected to increase with one study predicting a fuel economy improvement of 12.5-20% with a 19-31% weight reduction [4]. Another study has calculated an energy savings of 13.6 MJ/100 km for every 100 kg weight reduction for a gasoline powered car [5].

Generally, aluminum alloys have a high strength-weight ratio, excellent corrosion resistance, and good formability. In particular, the AA5182 aluminum alloy, which has a nominal composition of 4.5 wt-% Mg for solid solution strengthening, is known for its excellent formability and strength and is used in automotive body panels and reinforcement members [6]. However, welding aluminum presents a number of challenges relative to steel such as: a tenacious, high melting point oxide layer, low absorptivity to laser beams, high thermal conductivity, high coefficient of thermal expansion, and a high solubility of hydrogen in the liquid state relative to the solid state that can result in hydrogen porosity. In addition, the Mg alloying element in AA5182 has a low boiling point and low vapour pressure. As a result, Mg is preferentially vaporized during high-temperature welding processes such as keyhole-mode

laser welding, reducing the strength of the weld and producing keyhole instability and spikey weld bead geometry.

1.1 Lap-Joint Configuration Welding in Automobiles

Lap-joint configuration welds are one of the most commonly used types of weld joints in the automotive industry and are often joined using continuous seam welds or resistance spot welds. For example, the aluminum-bodied Audi A2 contains 35 m of laser seam welds and 20 m of mash seam welds that are used to join the sheet metal components in the lap-joint configuration [1]. Currently, the most commonly used welding processes for producing seam welds are gas metal arc welding (GMAW), laser beam welding (LBW), and resistance welding. However, new joining technologies will be required to facilitate the increased use of aluminum alloys in the mass-production of light-weight automotive structures.

1.2 Viable Welding Processes for Lap-Joint Welds

CO_2 and Nd:YAG laser beam welding (LBW) systems are the two most commonly used laser welding systems. CO_2 lasers have been successfully used for welding steel sheet, but are not normally used for welding aluminum [7]. The characteristic wavelength of a CO_2 laser is 10.6 μm compared to a characteristic wavelength of 1.06 μm for Nd:YAG lasers [8]. The higher wavelength of the CO_2 laser and the low absorptivity of aluminum at this wavelength prevent the laser beam energy from being readily absorbed by the highly reflective surface of the aluminum workpiece. This means that a larger heat input is required to melt the base metal. As a result, previous studies have shown that CO_2 lasers have a very small range of suitable welding conditions [9], [10]. On the other hand, Nd:YAG lasers have a higher absorptivity and can produce welds in aluminum sheet over a wide range of operating parameters.

Nd:YAG lasers are also desirable due to their high welding speed, energy density, and power output [8] - [10]. A number of studies have been conducted on the feasibility of welding aluminum sheet using a Nd:YAG laser welding system. Deutsch *et al.* [11] reported that single beam welds on 1.6 mm AA5182 sheet exhibited large amounts of undercutting and underfilling on the top surface of the bead, while the bottom surface of the bead had a very rough, spiky appearance with significant drop-through and undercutting. The dual-beam LBW technique, which was studied by Deutsch *et al.* [11], Punkari *et al.* [12], and Shibata *et al.* [13], was found to be capable of producing sound welds with a good surface appearance and minimal or even zero porosity at weld speeds of up to 166 mm/s with a welding power of 2-2.5 kW. However, the magnesium alloying element is easily vaporized during laser welding due to its high vapour pressure and low boiling point. There is a linear relationship between yield strength and magnesium content and studies have shown a significant decrease in the strength and hardness of laser welds due to a decrease in magnesium content [10], [14], [15]. The vaporization of alloying elements such as magnesium can also produce occluded gas porosity as the vaporized metal becomes trapped in the solidifying weld metal. Porosity has also been shown to be caused by the collapse of an unstable keyhole which results in the entrapment of metal vapours and shielding gas [8], [10], [16].

Friction stir welding (FSW) is a relatively new solid-state joining process in which a rotating cylindrical tool is plunged into the workpiece to generate frictional heat which softens the material. The softened material is transferred from the leading edge of the tool to the trailing edge by massive solid-state plastic deformation and the two workpieces are forged together [17]. Since there is no melting involved in FSW, defects such as solidification cracking, liquation cracking, hydrogen gas porosity, magnesium vaporization, and weld bead instability are uncommon. In addition, the specimens do not require any precleaning and the threads on the pin can assist in breaking up the oxide layer [18].

Although FSW appears to have several advantages compared to traditional fusion welding processes, there are some defects that are unique to FSW [18], [19]. Firstly, the surface oxide layer cannot be completely broken up due to the low temperature and is frequently entrained in the weld nugget. The entrained oxide has been shown in a previous study to reduce joint strength in lap-joint configuration welds [19]. Secondly, the rotating tool bit causes material on the advancing side to fold upwards along the weld nugget, and fold inwards toward the nugget along the retreating side as shown in Figure 1.1. These defects are known as hooking defects and cold lap defects, respectively. Failure has been found to occur along these defects in previous research [20]. Lastly, thinning of the workpiece is a defect which occurs as a result of excessive tool plunge depth, excessive rotation speed, and a slow travel speed, and has been found to decrease the strength of the joint [21], [22]. Recent studies by Yadava *et al.* [18], Cantin *et al.* [19], Cederquist *et al.* [22], and Soudarjan *et al.* [23] found that the FSW process was capable of producing good quality welds in the lap joint configuration between thin aluminum sheets. However, the maximum welding speed achieved in these studies was 6.35 mm/s which is normally insufficient for the high production rates required by the automotive industry.

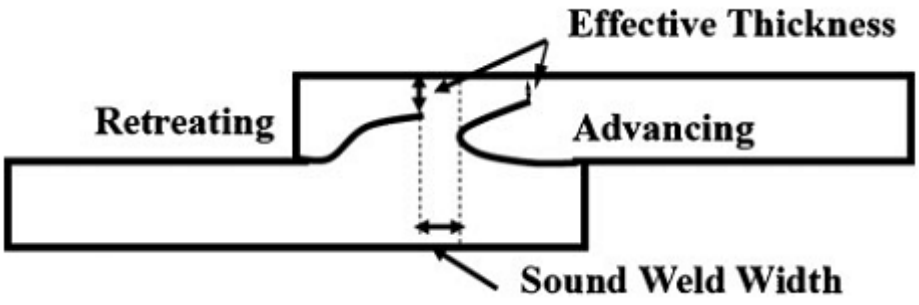

Figure 1.1: Schematic of defects in FSW (taken from Yadava *et al*. [18]).

Resistance spot welding (RSW) is one of the most commonly used joining techniques for joining sheet metal products and is widely used in the automotive industry [24]. RSW is a welding technique, shown

schematically in Figure 1.2, which uses the simultaneous application of localized resistive heating and mechanical pressure to join two sheets together by creating a weld "nugget" at the point of contact between the electrodes and the workpiece [17].

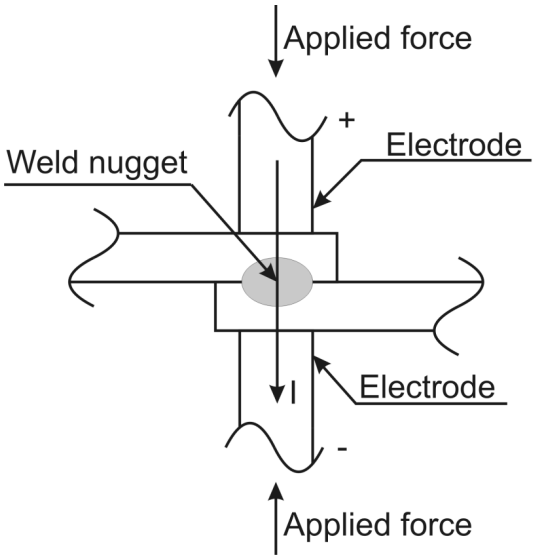

Figure 1.2: Schematic representation of the RSW process

The amount of heat generated by the process is governed by the formula shown in Equation 1.1, where Q is the heat generated, I is the electrical current, R is the workpiece resistance, and t is the welding time.

$$Q = I^2Rt \tag{1.1}$$

In addition to total heat input, the force applied by the electrodes is another factor that influences weld nugget formation. For example, as the amount of applied force increases, the contact resistance between the two sheets decreases [17]. Equation 1.1 shows that a decrease in resistance will lead to a reduction in heat input.

RSW of aluminum has a number of challenges compared to RSW of plain carbon steel. The main problem encountered during RSW of aluminum is the rapid rate of electrode wear which results in short electrode life and inconsistent weld quality [25], [26]. The primary cause of rapid electrode wear is the large amount of current required during RSW of aluminum which can range from 15 kA to 32 kA for 2 mm thick AA5182 sheet, depending on the desired nugget diameter [27]. Very large currents are required to generate the required heat because aluminum alloys have very low resistivity.

There are two mechanisms which cause electrode degradation during RSW of aluminum. Firstly, aluminum is readily soluble in copper and as a result, aluminum from the workpiece is easily deposited onto the electrode surface [28]. This is undesirable since, as shown in Figure 1.3, a change in the tip geometry will affect the heat distribution in the weld nugget and reduce process consistency [25], [29]. Secondly, the tenacious oxide layer acts as an electrical insulator which necessitates a larger amount of current to weld the workpiece. The force applied by the electrode can cause the brittle oxide layer to fracture in a non-uniform fashion, creating small pockets of exposed aluminum which has a higher conductivity than the oxide. When the current is applied it is forced to travel through the constricted areas, causing excessive heating and localized melting and alloying of the copper and aluminum [30].

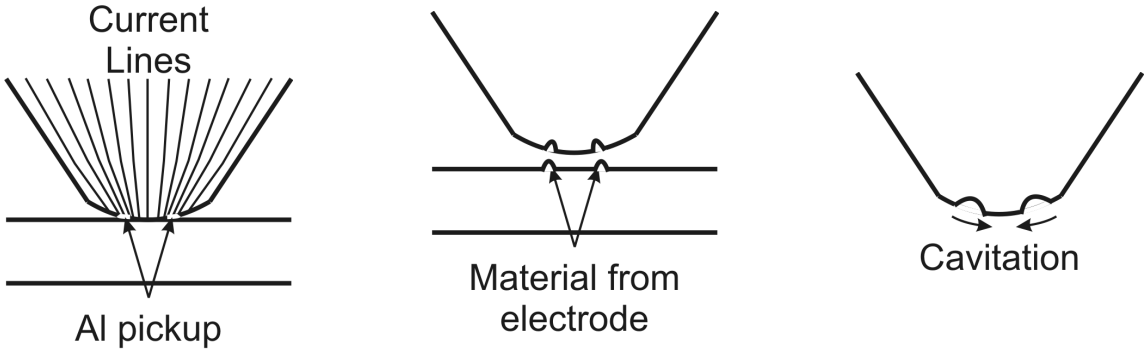

Figure 1.3: Pitting process in RSW of aluminum showing: ***a)*** Al pickup and alloying on electrode; ***b)*** pitting due to material loss from electrode; ***c)*** pit growth and cavity formation; taken from Lum *et al.* [28].

In a study performed by Fukumoto *et al.* [25] on RSW of 1.5 mm thick AA5182, the electrode life was found to range from 400 to 900 welds. In addition, electrode degradation was found to increase the contact tip area, decrease the corresponding current density, and produce undersized weld nuggets with lower joint strength. Some researchers have studied the use of coatings or lubricants on the electrode tip to improve electrode life. In a study by Rashid *et al.* [31], several different lubricants were used to coat 1.5 mm thick AA5182 sheet in an attempt to alter the contact resistance at the electrode-workpiece surface and prevent alloying between the copper electrode and aluminum workpiece. One lubricant was found to double the electrode life from 393 welds using an as-received surface to 730 welds using the lubricated surface. However, the effect of the lubricants on weld nugget porosity was not studied. In another study on electrode life, Lum *et al.* [28] used a Scotchbrite™ flap wheel to periodically clean the electrode surface to remove any aluminum contamination. Excessive electrode cleaning was found to alter the tip geometry and distort the electrode surface profile. However, cleaning the electrode every 50 welds was found to significantly improve tip life and reduce the variation in weld strength. The optimum cleaning interval was believed to be between 30 and 40 welds. However, a large aluminum-bodied car such as the Audi A8 contains 500 resistance spot welds and such frequent electrode cleaning may not be feasible in automotive production environments [27].

A number of arc welding processes such as gas tungsten arc welding (GTAW), gas metal arc welding (GMAW), and variable polarity plasma arc welding (VPPAW) have been used to weld aluminum sheet [32] - [37]. The variable polarity plasma arc welding (VPPAW) process has the highest energy density compared to other arc welding processes and is simpler and less expensive than LBW systems [24]. VPPAW is capable of producing high-speed, full penetration welds with a small HAZ. One of the main advantages of VPPAW versus LBW or FSW when welding aluminum alloys is the ability of the arc to remove the aluminum oxide layer through a phenomenon known as cathodic etching in which electrons

tunnel through and disrupt the oxide layer [17], [24]. Previous studies have shown VPPAW to produce good quality welds in 1.6 mm AA5182 at speeds up to 50 mm/s when using a stainless steel backing bar to reduce drop-through. However, the welded workpiece exhibited significant angular distortion due to an asymmetrical weld bead [11], [12].

Double-sided arc welding (DSAW) is a relatively new arc welding process which uses two torches mounted on opposite sides of the workpiece. Both torches are connected to a common power supply and the welding arc flows from one torch, through the workpiece, and into the other torch to create a symmetrical weld bead on both sides of the workpiece as shown in Figure 1.4.

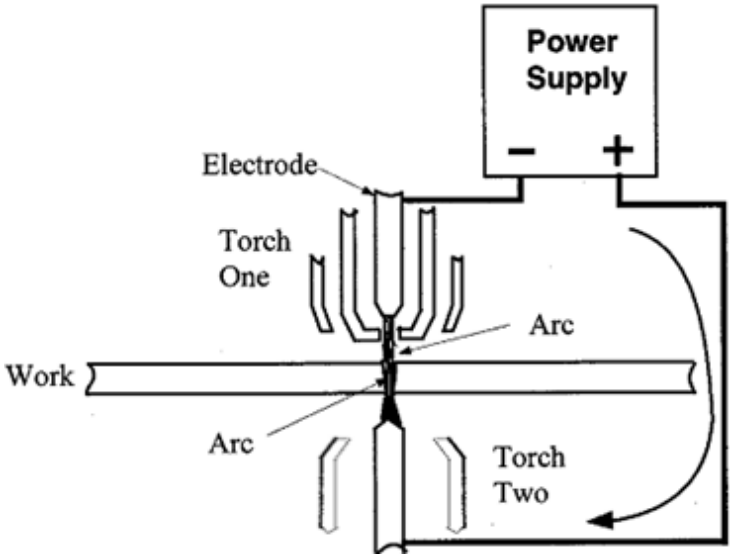

Figure 1.4: DSAW Schematic (taken from Zhang *et al.* [38]).

This process was invented by Y. Zhang and S.B. Zhang in 1999 and since then, the inventors have studied the application of this process to the keyhole-mode DSA welding of 6-12 mm thick carbon steel, aluminum, and stainless steel plates in the butt-joint configuration for applications such as ship hull

fabrication [38] - [43]. Their studies revealed that the higher energy density of the arc resulted in greater penetration and a smaller HAZ compared with VPPAW. The symmetry of the process also reduced the amount of angular thermal distortion. The inventors also found that the grain structure of the weld contained a large percentage of equiaxed grains which can reduce the risk of solidification cracking and improve mechanical properties such as strength and toughness [44].

More recently, the conduction-mode DSAW process has been successfully applied to the welding of 1 – 1.5 mm thick AA5182-O sheet in the butt-joint configuration by Kwon and Weckman [45], and Moulton and Weckman [46]. Kwon and Weckman were able to produce good quality welds with excellent cathodic cleaning on both sides of the workpiece at speeds of up to 60 mm/s at a welding power of up to 3.4 kW. The grain structure was found to exhibit a large percentage of equiaxed grains. Moulton and Weckman [46] were able to produce good quality welds between sheets of dissimilar thickness at speeds up to 70 mm/s at a welding power of 4.6 kW. Mechanical properties of welds made between sheets of dissimilar thickness were found to be comparable to the base metal and had excellent formability. However, welds produced at speeds greater than 25 mm/s were found to contain solidification micro-porosity. The amount of micro-porosity was found to increase with welding speed. This phenomenon was explained by the observation that welds produced at high speeds had a high length/width ratio which resulted in a longer mushy region. This decreased the flow of molten metal to the dendrite roots and voids were left due to solidification shrinkage. The micro-porosity was found to cause a significant decrease in weld ductility and formability. However, welds produced at speeds less than 25 mm/s were found to have excellent ductility and formability. Based on previous studies, the DSAW process is capable of producing good quality butt-joint configuration welds of thin aluminum sheet at high speed [45], [46]. In addition, this process has been shown in previous research to be capable of producing full penetration welds with fewer defects than LBW and at faster welding speeds compared

to FSW. However, the DSAW process has not yet been applied to lap-joint configuration welding of thin aluminum sheet. Therefore, the main goal of the present study was to examine the feasibility of using the DSAW process for spot and seam welding of aluminum sheet in the lap-joint configuration.

1.3 Research Objectives

The objectives of the present study were as follows:

1. Explore the feasibility of using conduction-mode DSAW for seam welding aluminum sheet in the lap-joint configuration
2. Identify and characterize the range of suitable welding conditions for producing lap-joint configuration seam welds between 1 mm thick sheets of AA5182 alloy
3. Investigate the causes of defects such as gas porosity in DSA welds and identify solutions to minimize porosity
4. Determine whether the DSAW process can be used to produce spot welds between 1 mm thick sheets of AA5182 alloy
5. Characterize the mechanical properties of DSAW seam welds

Chapter 2: Literature Review

2.1 Double-Sided Arc Welding Process

The double-sided arc welding process is a relatively new type of welding process that uses two welding torches to weld the workpiece from both sides. This process was invented by Y.M. Zhang and S.B. Zhang [39] to increase weld joint penetration by means of a highly concentrated arc that travels across the two torches. The important process parameters during DSAW of aluminum sheet are the polarity fraction, operating mode, shielding gas selection, shielding gas flow rate, and electrode geometry. The importance of these parameters is explained in the following sections.

2.1.1 Plasma Arc Welding of Aluminum

Plasma arc welding is a gas-shielded arc welding process in which a narrow copper orifice is used to constrict the normally bell-shaped arc and produce a high velocity, collimated plasma jet [24]. A schematic of the PAW torch is shown in Figure 2.1. The plasma jet is created when the orifice gas is heated to a high temperature by the electric arc, producing an electrically conductive, ionized gas [17]. The high energy density associated with the plasma jet can allow the PAW torch to operate in keyhole mode and penetrate through thick materials at high speeds. The PAW process uses a nonconsumable electrode and is similar to the GTAW process. However, since the plasma and the arc travel through a constricted nozzle, the PAW arc is stiffer and has a higher energy density [17]. The distance that the electrode is recessed in the orifice is known as the setback distance. This distance must be large enough to prevent the electrode from shorting with the orifice cup. The torch-to-workpiece distance is known as the standoff. Since the arc takes a largely cylindrical shape, the standoff distance does not have a strong effect on the energy distribution of the arc [17].

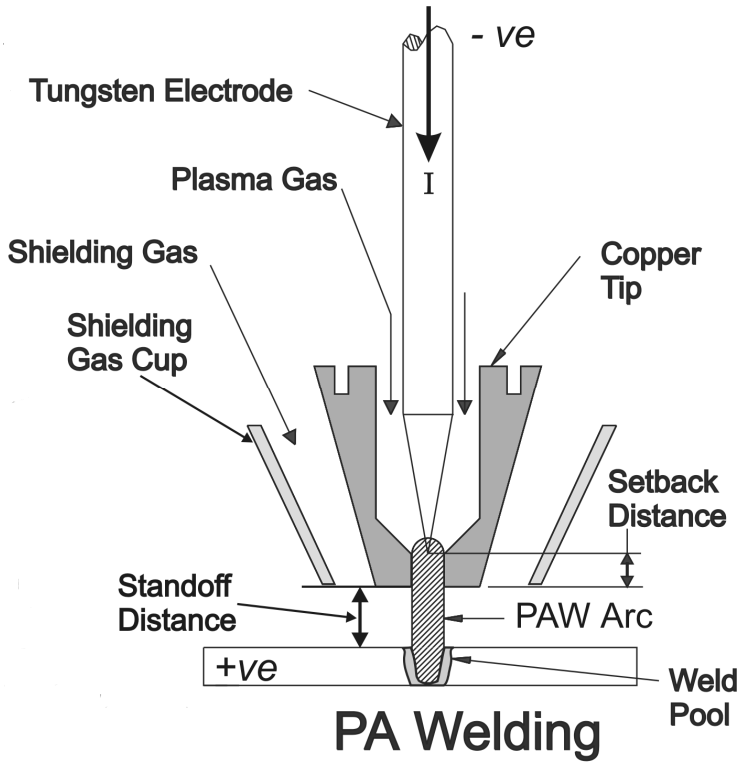

Figure 2.1: PAW torch schematic (taken from Kwon [47]).

Before the welding sequence is initiated, the plasma and shielding gases are set to the required flow rates. Argon is typically used for the orifice gas since its low ionization potential produces a reliable pilot arc [17]. Next, a high frequency voltage is induced between the tungsten electrode and the inner part of the copper orifice to start a pilot arc. Once the main arc is activated, the arc is transferred from the electrode to the workpiece and a molten weld pool is formed.

The PAW process can be operated in keyhole-mode or conduction-mode. A schematic comparing the two welding modes is shown in Figure 2.2. In keyhole-mode welding, the plasma jet creates a vapour cavity which penetrates through the thickness of the workpiece to produce a tall, narrow weld pool [24]. Keyhole-mode welding is generally performed at high currents and is used to weld thick plate at high

speeds. Welds produced using the keyhole process are narrower, exhibit less thermal distortion, and contain a smaller heat affected zone compared to GTA welds [24]. In conduction-mode welding, a bowl-shaped weld pool is formed by the arc and is generally similar to the weld pool formed when using the GTAW process [24]. Conduction-mode welding is performed at low currents and produces a smooth weld bead.

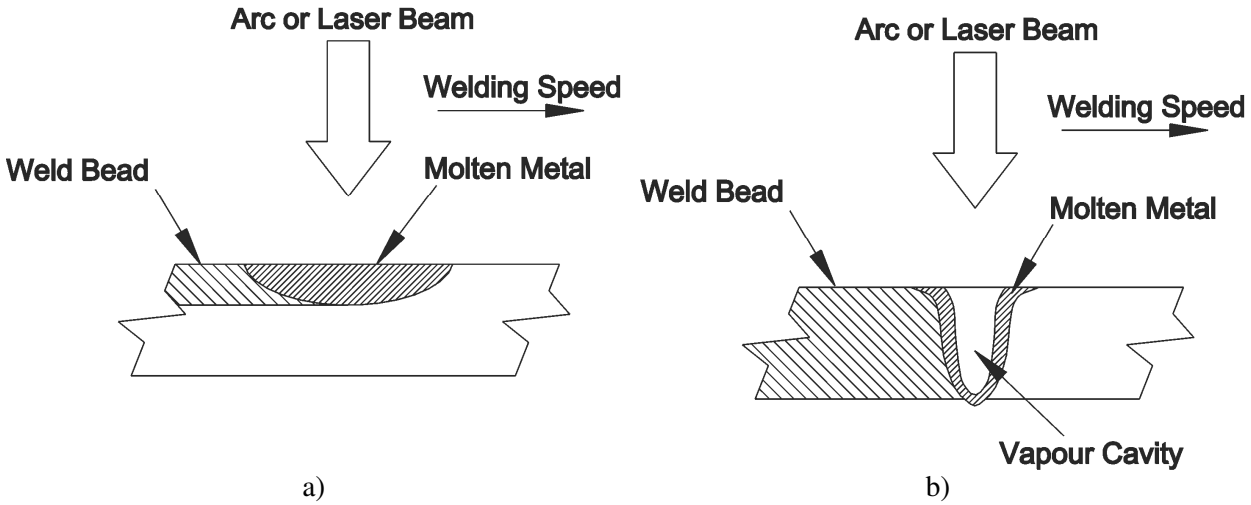

Figure 2.2: Comparison of: ***a)*** conduction-mode and ***b)*** keyhole-mode welding (taken from Punkari [12]).

Electrode geometry also plays an important role during plasma arc welding. Electrodes can either be used with a conical profile or a blunt profile. In GTA welding, the arc becomes more constricted as the electrode profile changes from a conical shape to a blunt tip [44]. In addition, blunt electrodes tend to have a longer electrode life since the blunt tip has a greater cross-sectional area compared to the conical tip. This increases heat transfer away from the tip and prevents the formation of a molten ball during welding [46]. Deutsch [11] and Punkari [12] investigated electrode degradation during VPPAW of AA5182 and AA5754 sheet and found high rates of degradation when using conical tips. However, blunt electrodes require higher setbacks, resulting in a higher torch voltage, lower process efficiency, and decreased heat transfer to the workpiece [46]. Moulton and Weckman [46] found that a conical electrode

truncated to a 3.2 mm diameter provided the best compromise between process efficiency and electrode life during DSAW of 1.5 mm thick AA5182 sheet.

2.1.2 PAW Power Supply

PAW torches are normally powered by constant current power supplies. A constant current, variable polarity, square-wave alternating current power supply is used most often when cathodic cleaning of the oxide is required. This form of PAW is called Variable Polarity Plasma Arc Welding (VPPAW) and is used for welding alloys which have tenacious, high-melting point oxides such as aluminum alloys [17]. A variable polarity power supply has the ability to alter the magnitude of each half cycle and the amount of time spent in each half cycle, as shown in Figure 2.3. The fraction of time spent in DCEN and the DCEN polarity fraction are denoted by θ and β, respectively, and can be calculated using Equation 2.1 and Equation 2.2.

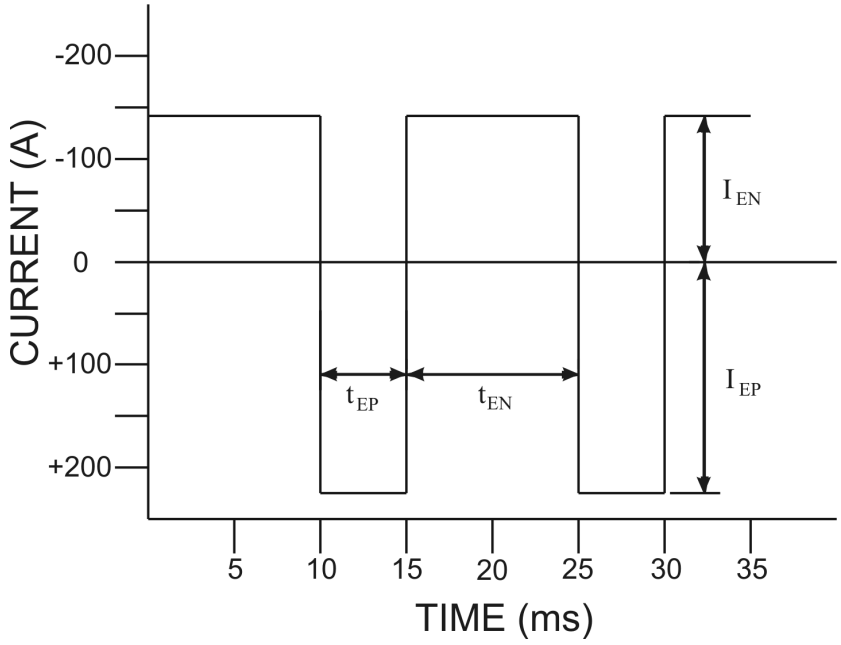

Figure 2.3: Adjustable parameters of the welding current waveform (taken form Kwon [45]).

$$\theta = \frac{|t_{EN}|}{|t_{EN}| + |t_{EP}|} \tag{2.1}$$

$$\beta = \frac{|I_{EN}|}{|I_{EN}| + |I_{EP}|} \tag{2.2}$$

These parameters were initially studied by Okada *et al.* [48] in a study of polarity in tungsten inert gas (TIG) welding of aluminum, and by Fuerschbach [49] during a study of cathodic cleaning in VPPAW of aluminum. A study by Kwon and Weckman [45] on DSAW of thin aluminum sheet found that a balanced, symmetrical waveform produced the best combination of cathodic cleaning and penetration. Therefore, the values for θ and β were kept at 0.5 during this study.

2.1.3 Fluid Flow in the Weld Pool

The three main forces responsible for driving fluid flow in the molten weld pool are: Lorentz forces, Marangoni forces, and buoyancy forces [44], [50]. These forces generate flow in the cross-section of the weld. Although the following paragraphs present the individual effects of each force, all three forces can interact with each other to produce complex fluid flow in the weld pool.

The Lorentz force, F, can be expressed by the following equation,

$$\vec{F} = \vec{\mathrm{J}} \times \vec{\mathrm{B}} \tag{2.3}$$

where $\vec{\mathrm{J}}$ is the current density vector in the direction of the current, and $\vec{\mathrm{B}}$ is the magnetic flux vector. In DCEN arc welding processes where the workpiece is connected to the positive power supply terminal, the Lorentz force creates a stirring effect with molten fluid circulating down along the centerline of the weld pool and back up along the fusion zone as shown in Figure 2.4a. Penetration increases as the Lorentz force pushes the molten metal downwards and transfers heat to the bottom of the weld pool. Since the

Lorentz force is proportional to the current density, higher welding currents will produce stronger Lorentz forces.

Marangoni convection occurs due to differences in surface tension on the surface of the weld pool because surface tension depends on temperature. The force exerted by the difference in surface tension, F_γ, is given by

$$\overrightarrow{F_\gamma} = -\frac{d\gamma}{dT}\nabla T \tag{2.4}$$

where γ is the surface tension of the molten metal, T is the temperature, and ∇T is the temperature gradient at the weld pool surface [50]. For most alloys, the cooler fluid at the edge of the weld pool has a higher surface tension than the hotter fluid in the centre of the weld pool which is directly under the arc. This causes the fluid at the centre of the weld pool to be pulled outwards toward the edge of the weld pool as shown in Figure 2.4b. The outward flow of weld metal caused by Marangoni convection produces wide, shallow welds.

Buoyancy driven fluid flow is generally the weakest driving force in a weld pool and occurs due to a change in density with respect to temperature. The buoyancy force, F_B, is defined as

$$\overrightarrow{F_B} = \rho B\vec{g}(T - T_o) \tag{2.5}$$

where ρ is the density of the fluid, B is the coefficient of thermal expansion of the liquid molten metal, $\vec{g}$ is the gravitational attraction, T is the temperature of interest, and T_o is the reference temperature [50]. It is apparent from Equation 2.5 that the difference in temperature is the main cause of buoyancy driven fluid flow [50]. Since density decreases with temperature, the fluid closest to the arc will have a lower density than the fluid at the edge of the weld pool. This causes the denser fluid to flow to the bottom of the workpiece under the force of gravity, while the lighter fluid rises to the top as shown in Figure 2.4c.

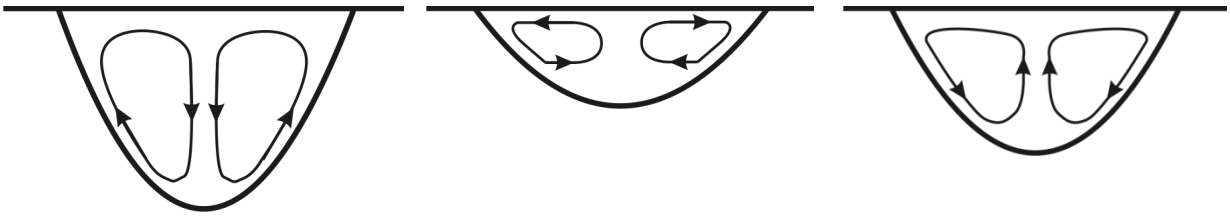

Figure 2.4: Fluid flow in a weld pool caused by: ***a)*** Lorentz forces; ***b)*** Marangoni convection; ***c)*** buoyancy (from Kou [44]).

In a study by Kou and Sun [51] on fluid flow in stationary GTA welds in AA6061, the surface tension gradient force was found to be the primary driver of fluid flow in the weld pool, followed by Lorentz forces, and lastly by buoyancy forces. Marangoni convection was found to be capable of generating fluid flow in the weld pool with a velocity between 10 – 100 cm/s, while Lorentz forces generated velocities of up to 10 cm/s, and buoyancy forces only generated velocities of up to 1 cm/s. Dong *et al.* [52] investigated fluid flow in DSA welds of 6 mm thick AA2024 plate in the flat position using a dual-GTAW torch setup and found that the role of buoyancy forces was insignificant in comparison to the Lorentz force. Increasing the welding current was found to increase the strength of the Lorentz force due to the greater current density, and also increase the strength of the buoyancy force due to the higher temperature. In a real weld pool, the three driving forces for fluid flow can compete against each other resulting in more complex fluid flow. Keyhole-mode welding can also generate fluid flow in the weld pool. During keyhole-mode welding, the moving keyhole causes molten weld metal to flow around and resolidify behind the keyhole.

Howard *et al.* [53], investigated the fluid motion in lap-fillet configuration, high-power diode laser (HPDL) welds between AA5182 and AA6111 sheet. A mixing pattern was seen when AA6111 sheet was placed on top of AA5182 sheet when producing lap-fillet joints. However, when the position of the

sheets was reversed there was no mixing between the two alloys. During conduction-mode laser welding of aluminum alloys, Lorentz forces are not generated due to the lack of an electric current, and Marangoni forces may be very small due to the formation of surface oxides. Therefore, only weak buoyancy driven fluid flow would exist in the weld pool, and the main driving force was found to be the difference in density between the two alloys, with the AA6111 sheet having a slightly higher density than the AA5182 sheet.

2.1.4 Dual VPPAW DSAW

In a variation of the DSAW process, two PAW torches are connected to one power supply operating in constant current square wave AC mode as shown in Figure 2.5. In keyhole-mode DSAW, a portion of the welding current is able to travel through the plasma-infused keyhole while the remainder travels through the workpiece [42]. The total voltage drop between electrodes associated with keyhole-mode DSAW is shown in Equation 2.6, where V_{EC} is the cathode voltage, V_{C1} is the voltage of arc column 1, V_K is the voltage across the keyhole, V_{C2} is the voltage across arc column 2, and V_{EA} is the voltage across the anode. In conduction-mode welding, the current passes through the workpiece and the associated voltage drop is given in Equation 2.7, and shown schematically in Figure 2.5, where V_{WA} is the voltage across the work anode, and V_{WC} is the voltage across the work cathode. The voltage drop across the workpiece will be close to zero when welding thin, conductive sheet such as aluminum sheet.

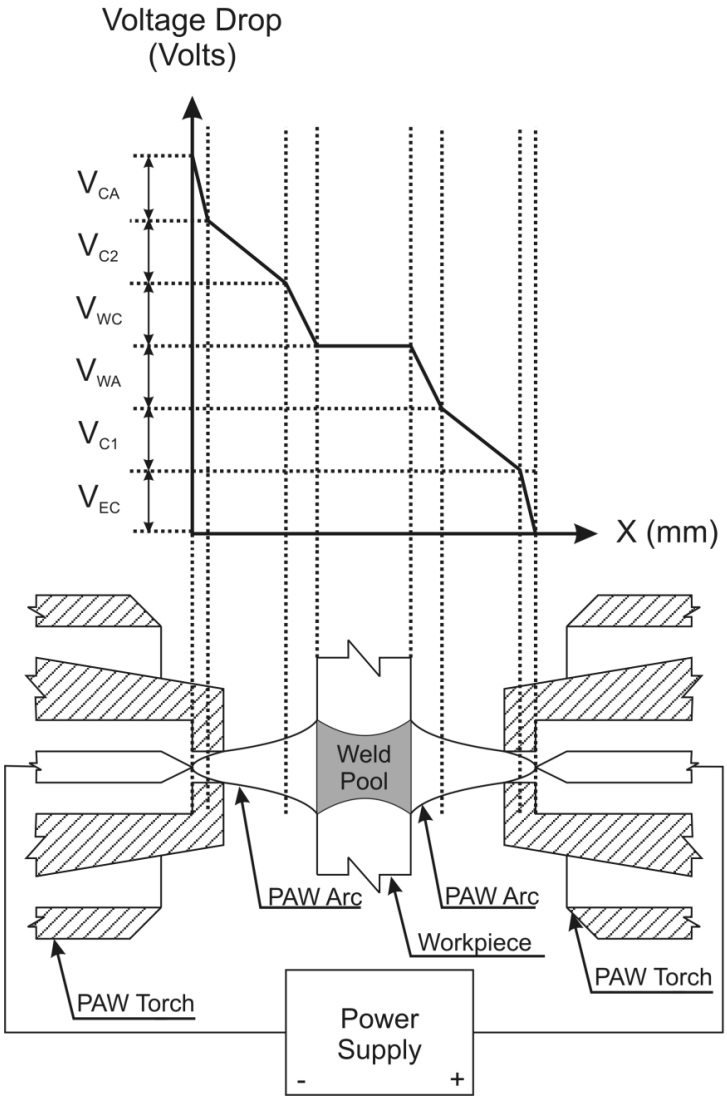

Figure 2.5: Voltage drops in conduction-mode DSAW using two PAW torches.

$$V = V_{EC} + V_{C1} + V_K + V_{C2} + V_{EA} \tag{2.6}$$

$$V = V_{EC} + V_{C1} + V_{WA} + V_{WK} + V_{C2} + V_{EA} \tag{2.7}$$

2.1.5 DSAW in Thick Plate

Y.M. Zhang and S.B. Zhang [38] - [43], investigated the applications of autogeneous, keyhole-mode, butt-joint configuration DSA welds in 6-12 mm thick carbon steel, aluminum, and stainless steel plates. The purpose of these studies was to determine the feasibility of DSAW for shipbuilding applications. Compared to VPPAW, DSAW was found to produce welds with greater penetration, a finer microstructure with a high percentage of equiaxed grains, less angular thermal distortion, less porosity, and no undercutting.

In a study by Zhang *et al.* [42] which compared DSAW and VPPAW of thick austenitic stainless steel plate, the keyhole-mode DSAW process was found to be capable of producing full penetration butt-joint welds in 9.5 mm thick plate at a welding power of 3.15 kW and a welding speed of 80 mm/s. In contrast, the keyhole-mode VPPAW process could only produce full penetration welds in 6.4 mm thick plate with a welding power of 2.1 kW and a welding speed of 40 mm/s. In other words, the DSAW process was able to fully penetrate a thicker plate using only 60% of the heat input required by the VPPAW process. Similarly, the DSAW process was found to require only 30% of the heat input required by VPPAW to weld a 9.5 mm thick plate. A comparison of the microstructure revealed that the DSA weld contained a greater percentage of equiaxed grains with only a small region of columnar grains at the fusion boundary.

In another study by Y.M. Zhang and S.B. Zhang [38], the pulsed keyhole-mode DSAW technique was used to produce very narrow welds at high speeds in 10 mm thick type 304 stainless steel. The high pressures associated with a high welding current can blow metal away from the workpiece when producing keyhole-mode welds at a constant current. To avoid this phenomenon, the authors suggested using a pulsed current waveform in which a penetrating keyhole was periodically established and then

closed to maintain a stable weld pool while producing narrow, full-penetration welds with minimal heat input. A schematic of this waveform is shown in Figure 2.6. The authors found the pulsed DSAW process was capable of producing full-penetration butt-joint configuration welds in 12.7 mm thick type 304 stainless steel plate and 10 mm thick DH36 carbon-manganese steel. The welds were found to possess a high depth-width ratio and a symmetrical geometry.

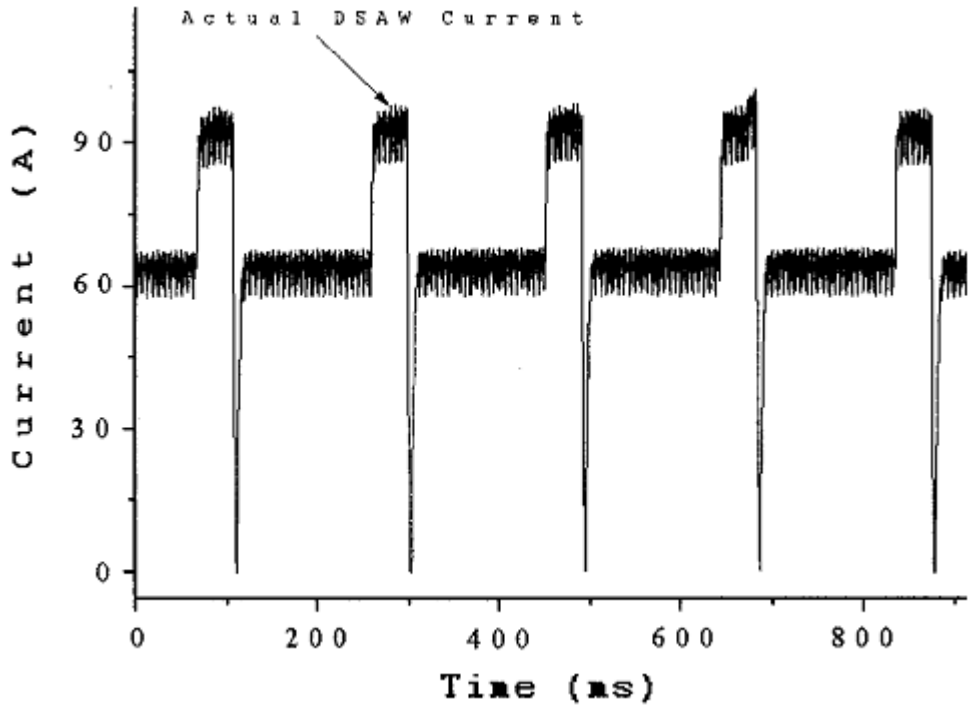

Figure 2.6: Waveform of pulsed DSAW current (taken from Zhang *et al*. [38]).

A large amount of underfilling was observed in the welds because they were produced autogeneously. However, the authors believed that this defect could be eliminated by adapting the process into a non-autogeneous process.

Y.M. Zhang and S.B. Zhang [40], also studied the application of DSAW to the welding of thick 5xxx and 6xxx series aluminum alloys. The authors found that the welds exhibited a beneficial columnar-to-equiaxed grain transition (CET) in a study of the solidification behaviour of welds produced in 6.4 mm thick AA5050. Full penetration welds were found to contain a greater amount of equiaxed grains compared to partial-penetration welds. This was explained by the larger amount of melted metal in the fully penetrated welds which increased the cooling in the weld and decreased the thermal gradient. However, the authors believed that the decreased thermal gradient could not fully account for the large percentage of equiaxed grains. Instead, the equiaxed microstructure was attributed to strong Lorentz forces which produced a stirring effect in the DSA weld pool. The specimens used in this study were not cleaned prior to welding and the resulting welds exhibited significant amounts of hydrogen gas porosity. The authors found that the amount of porosity and the size of the pores decreased with increasing joint penetration. In addition, the larger pores were found to form in the columnar grains while the smaller pores formed in the equiaxed grains.

In another study by Y.M. Zhang and S.B. Zhang [41], a series of autogeneous, butt-joint configuration welds were produced in 6.4 mm and 9.5 mm thick AA6061-T651 using a dual-GTAW DSAW process. This alloy is notorious for its high sensitivity to solidification and liquation cracking and is normally welded using filler metals to reduce the freezing range and subsequent cracking sensitivity. In this study, the authors claimed to have produced full-penetration, single-pass, crack-free welds in 6.4 mm thick plate using a total welding power of 6.8 kW and a welding speed of up to 7.5 mm/s. In comparison, a standard AC GTAW process was found to require a welding power of 4.35 kW and a welding speed of 2 mm/s and was incapable of producing crack-free, full penetration welds. The authors found that the symmetrical bead geometry and lower heat input in DSAW decreased the thermal stresses and solidification shrinkage

in the weld. In addition, the authors believed that the Lorentz forces produced by the alternating current produced a stirring effect in the weld pool which improved fluid flow and heat transfer.

2.1.6 DSAW in Thin Sheets

Kwon and Weckman [45], [47] first studied the application of conduction-mode DSAW for welding of thin aluminum sheet. In this study, a series of autogeneous, full-penetration welds were produced in 1.2 mm and 1.15 mm thick AA5182-O sheets in the butt-joint configuration using a variable polarity power supply with a balanced waveform. The DSAW process was found to be capable of producing acceptable welds at a welding power of up to 3.4 kW and welding speeds of 40 to 60 mm/s. The weld beads had a symmetrical, hour-glass profile and showed excellent cathodic cleaning, minimal porosity, no evidence of undercutting, and minimal underfill and drop-through. An analysis of the weld microstructure revealed that up to 40% of the weld metal was comprised of equiaxed grains which is similar to results observed by Zhang *et al.* [40]. Higher welding speeds were found to increase the quantity of equiaxed grains. The weld width was found to increase linearly as the total welding power was increased from 1.8 kW to 2.7 kW, given a constant welding speed. However, when the welding power was increased to 3.4 kW there was very little change in the weld width since the clamps started to act as heat sinks. Tensile tests revealed the welded sheets to have a 5% lower yield strength compared to the base metal with a joint efficiency of 91%.

Moulton and Weckman[46], [54] further studied the application of DSAW to conduction-mode welding of thin AA5182-O sheet by welding dissimilar thickness aluminum sheet for TWB applications. During this study, 1.0 mm thick sheet was joined to 1.5 mm thick sheet in the butt-joint configuration. Visually acceptable, full-penetration welds were produced at a maximum welding power of 4.6 kW using

a travel speed of 70 mm/s. Again, the weld beads displayed a symmetrical, hourglass profile with excellent cathodic cleaning, minimal porosity, no evidence of undercutting, and minimal underfill and drop-through. However, welds produced at speeds greater than 25 mm/s were to found to exhibit solidification shrinkage micro-porosity which was found to severely degrade the ductility and formability of the weld specimen. The formation of micro-porosity was found to be caused by a large length/width ratio which increased the size of the mushy zone and prevented the ability of the molten weld metal to fill voids left by solidification shrinkage. Welds produced at speeds of 25 mm/s or less did not show any signs of solidification shrinkage micro-porosity and possessed excellent mechanical properties.

2.2 Factors Affecting Weldability of Aluminum Alloys

Welding of aluminum presents a number of challenges compared to steel. The tenacious oxide layer which protects the aluminum from corrosion also prevents heat from flowing into the base metal, making it difficult to melt. The high solubility of hydrogen in molten aluminum can cause the formation of large hydrogen gas bubbles which reduce the mechanical properties of the weld. The high thermal conductivity of aluminum, which is approximately six times greater than that of steel, necessitates the use of higher heat inputs to melt the material. Lastly, the high thermal expansion coefficient of aluminum, which is approximately double that of steel, can cause weld distortion and solidification cracking [24].

2.2.1 Aluminum Oxide and Cathodic Cleaning

Bare aluminum oxidizes rapidly when exposed to oxygen and instantly forms a thin protective oxide layer. This oxide presents several challenges to the welding of aluminum due to its high melting point and low electrical conductivity. Over time, the oxide can also absorb significant quantities of moisture

from room air in the form of aluminum hydroxide which contribute to hydrogen gas porosity. Compared to other aluminum alloys, the 5xxx series is more sensitive to the formation of oxides and great care must be taken to remove the oxide prior to welding [17]. Thin oxide layers can be easily removed by cathodic cleaning in arc welding processes. Thicker layers, however, must be removed through chemical or mechanical means prior to welding [24].

A phenomenon known as cathodic cleaning occurs when direct-current electrode positive (DCEP) welding is used to join aluminum [17], [24]. During cathodic cleaning, the surface oxide layer is removed from the workpiece by the arc and this improves the weld bead appearance. According to the literature, the accepted theory suggests that electron discharge from the workpiece is responsible for cathodic cleaning [24], [55]. During DCEP, a layer of positive ions accumulates on the surface of the workpiece and creates an electric field. Electrons within the surface oxide layer are attracted to the electric field and tunnel through the oxide towards emissions sites. As the moving electrons are ejected away from the workpiece, the oxide at the emission sites is broken up [24], [55].

Fuerschbach [49] investigated the importance of process parameters on the effectiveness of cathodic cleaning during VPPAW of AA1100 sheet. Optimal cleaning occurred when beta was within the range of 0.2-0.5 and when theta was less than 0.5, where θ was the fraction of time spent in DCEN, and β was the DCEN polarity fraction. Therefore, the duration of time spent in DCEP polarity was the primary factor in determining the extent of cathodic cleaning. However, some degree of DCEN polarity was required for optimum cleaning to prevent arc instability. The amplitude of the DCEP current was not a significant factor. In their study of DSA welding of AA5182 sheet, Kwon and Weckman[45], [47] determined that a DCEP polarity balance of at least 30% was required to obtain adequate cathodic cleaning during DSAW.

When θ and β were set to less than 0.4, only the top surface of the workpiece was observed to have good cathodic cleaning. For values of θ and β greater than 0.6, only the bottom surface of the workpiece was observed to have good cathodic cleaning. When θ and β were set between 0.4 and 0.6 good cathodic cleaning was observed on both surfaces. Therefore, the optimal value for θ and β was found to be 0.5 when using the DSAW process. Moulton and Weckman [46], [54] investigated the effects of torch standoff on oxide removal and found that increasing the standoff produced a wider cathodically cleaned region. The larger cathodically etched region was attributed to the increase in arc width caused by the increase in standoff.

2.2.2 Porosity

The two main types of porosity found in aluminum alloy welds are hydrogen gas porosity and solidification shrinkage porosity. Hydrogen gas porosity is caused by the evolution of gasses during solidification of a molten weld pool and occurs when the concentration of hydrogen gas in the molten metal is higher than its solubility in the solid phase [56]. The main cause of hydrogen gas porosity is the large difference in hydrogen solubility between the molten and solid states as shown in Figure 2.7 [44], [56]. In addition, hydrogen is the only gas that has a measurable solubility in liquid aluminum alloys [56], [57]. Moisture reacts easily with molten aluminum to produce hydrogen gas as shown in Equation 2.8 [56]. This reaction can release hydrogen that can easily dissolve into molten aluminum according to Equation 2.9 [56].

$$3H_2O + 2[Al] = Al_2O_3 + 3H_2 \quad (2.8)$$

$$H_2 = 2[H] \quad (2.9)$$

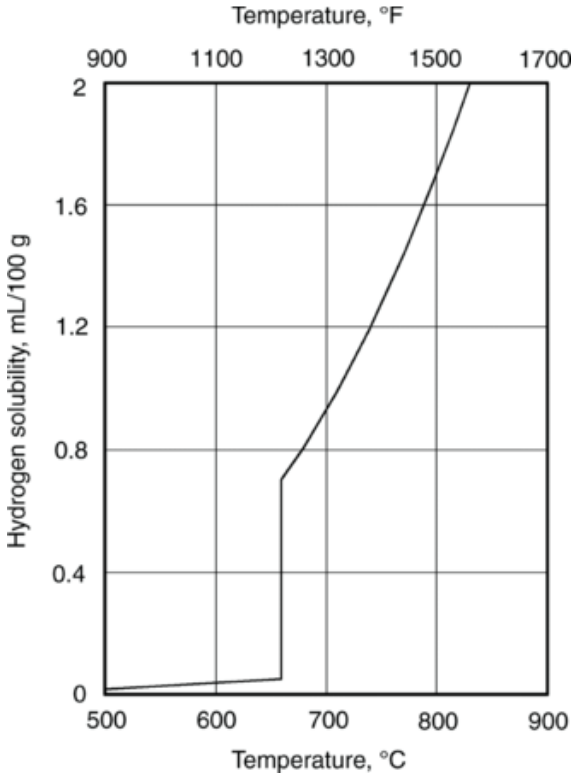

Figure 2.7: Hydrogen solubility in aluminum taken from ASM Handbook Vol. 15 [56].

As the molten weld pool solidifies, hydrogen is rejected into the liquid and eventually nucleates into spherical-shaped gas bubbles shown in Figure 2.8a. Given enough time, the gas bubbles may float out of the molten weld pool. However, at high welding speeds, the weld may solidify too quickly to allow the gas bubbles to float out. In addition, a thin oxide layer may form on top of the weld pool and prevent the ejection of gas. Common sources of hydrogen include oils, greases, paints, solvents, and moisture. These substances are easily absorbed and retained by the porous aluminum oxide [44], [58]. When stored in the presence of changing temperatures and high humidity, these alloys will grow a thick, moisture rich oxide layer known as a "water stain" [58].

Shrinkage porosity is formed when the shrinkage due to solidification cannot be filled in by liquid and generally takes an irregular shape as shown in Figure 2.8b. Volumetric solidification shrinkage of between 3.5-8.5% is commonly seen in aluminum alloys [6]. Solidification shrinkage is more problematic in aluminum alloys compared to steel since the aluminum atoms are rearranged into a dense, close-packed face-centered cubic (FCC) structure upon solidification whereas the iron atoms are rearranged into a more open body-centered cubic (BCC) structure [59].

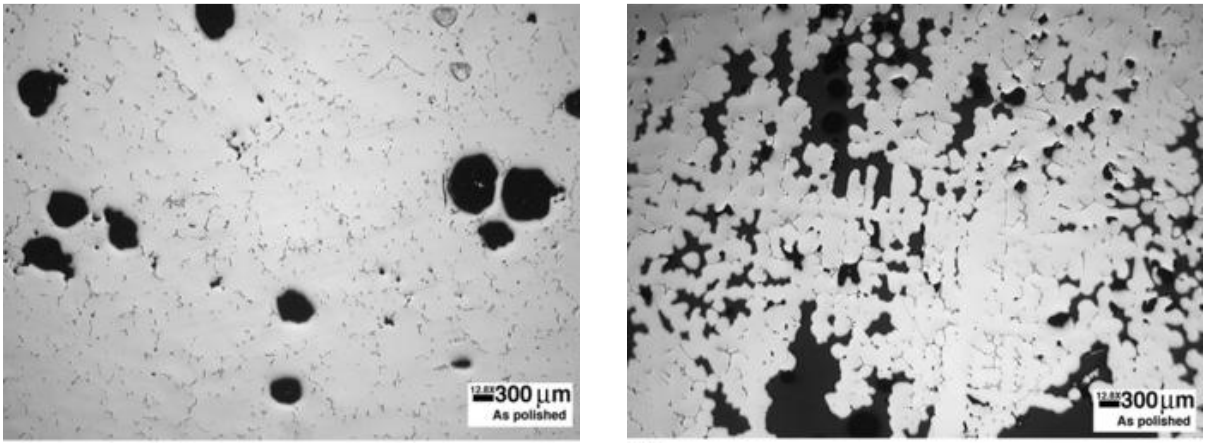

a) b)

Figure 2.8: Porosity formation in an AA5182 casting showing ***a)*** hydrogen gas porosity; ***b)*** solidification shrinkage porosity (taken from ASM Handbook Vol 15. [56]).

Porosity is undesirable in welds since it reduces mechanical properties such as tensile strength, ductility, and formability. Kwon and Weckman [45], [47] used a LaserStrobe imaging system to capture the formation of gas pores during DSAW of degreased, 2.5 mm thick AA5182 sheet. The results showed the hydrated aluminum oxide to be the main source of porosity in the aluminum welds and that cathodic cleaning was incapable of removing the thick, hydrated oxide layer. Gas porosity was reduced by producing full penetration welds in sheet which were stainless steel wire brushed prior to welding.

Moulton and Weckman [46], [54] also found that stainless steel wire brushing significantly reduced porosity content and improved weld bead consistency and appearance. However, welds produced at welding speeds greater than 25 mm/s exhibited a significant amount of solidification shrinkage micro-porosity. Additionally, as the welding speed was increased, the quantity of solidification micro-porosity was also found to increase. The authors observed that an increase in welding speed resulted in an increase in the length-to-width ratio. With a high length-to-width ratio there was a larger distance between the liquidus and non-equilibrium solidus, as well as a low thermal gradient in the mushy zone at the tail of the weld. These conditions prevented the voids caused by solidification shrinkage from being filled by the liquid in the weld pool, resulting in the nucleation and growth of solidification microporosity at the dendrite roots. Welds produced at speeds of 25 mm/s or less were free of solidification shrinkage micro-porosity.

2.2.3 Shielding Gas Flow in Welding Nozzles

Molten aluminum reacts very easily with oxygen and water in room air. Therefore, adequate shielding gas coverage must be provided in order to produce high quality, defect-free welds. The primary purpose of the shielding gas is to displace the surrounding atmosphere from the molten weld pool. The ability of the shielding gas to cover the weld pool is influenced by parameters such as: gas flow rate, nozzle diameter, and torch-to-workpiece distance [60]. The flow rate and nozzle diameter are especially important since the flow rate has to be matched to the nozzle diameter to avoid turbulent gas flow [17]. Turbulence in the shielding gas can lead to increased mixing with room air, causing inadequate protection of the weld pool and poor joint quality.

The flow through a shielding gas nozzle can be modeled as an annular impinging jet which contains three main regions, each with their own flow characteristics as shown in Figure 2.9. In the free jet region, the gas flow resembles that of an unobstructed free jet. In the impingement region, there is a high static pressure which reaches its maximum value at the stagnation point. In the wall jet region, the gas flow thickens and moves radially outwards.

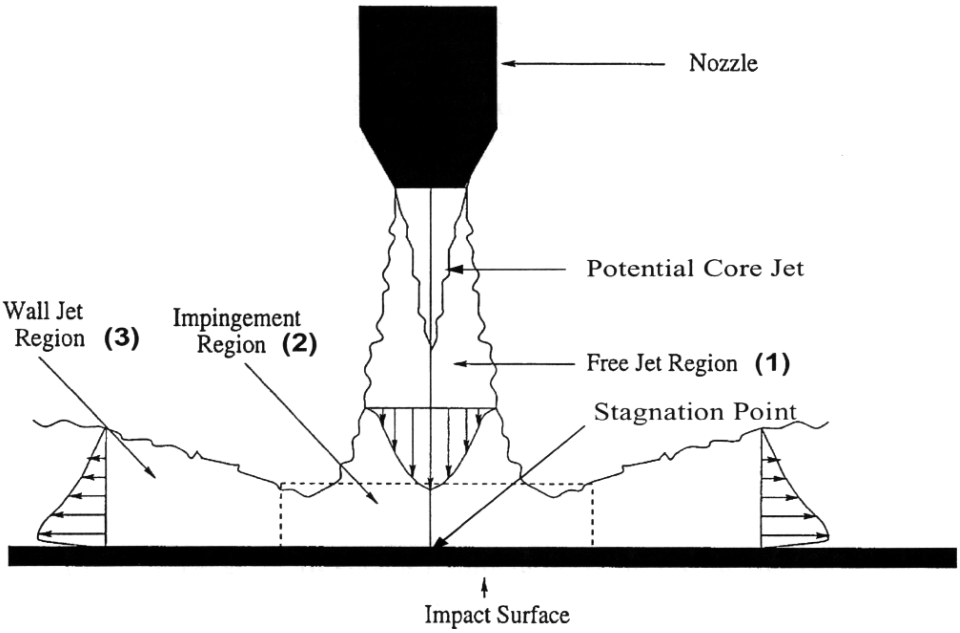

Figure 2.9 Schematic diagram of an impinging jet, (taken from Donaldson and Snedeker [61]).

The non-dimensional Reynolds number, Re, shown in Equation 2.9, is used frequently to describe the flow characteristics of a fluid through a pipe and other geometries, where ρ is the density of the fluid, V is the mean fluid velocity, d is the characteristic length, and μ is the dynamic viscosity of the fluid [62].

$$Re = \frac{\rho V d}{\mu} \tag{2.9}$$

In a constant cross-section pipe, laminar flow will occur at a Reynolds number of less than 2100 and fully developed turbulent flow will occur at values greater than 4000 [62]. Random, turbulent

fluctuations may be seen between these values. However, shielding gas flow in a PAW nozzle is more complex due to the short internal development length and non-uniform cross section of the nozzle. Therefore, fully developed turbulent flow may occur at a Reynolds number of less than 4000 [62].

Johnson *et al.* [60] studied the gas flow in a GMAW shielding gas nozzle at different flow parameters such as gas flow rate, torch travel speed, and torch-to-workpiece distance. In a series of tests conducted using a constant torch-to-workpiece distance and a stationary torch, laminar gas flow was observed at Re = 1260, as seen in Figure 2.10a. In this case, the flow at the emerging jet and the flow away from the impingement region were observed to have a smooth, stable profile. An increase in the gas flow rate increased the Reynolds number to 1680 and the jet edge was observed to show signs of instability as shown in Figure 2.10b. At an even higher gas flow rate, the Reynolds number increased to 2100 and large vortices were observed along the jet edge and impingement region as shown in Figure 2.10c. In other words, turbulent, unsteady flow was observed at Re = 2100.

Turbulent shielding gas flow can have adverse effects on the quality of the weld pool. The eddy currents seen in the turbulent flow have the potential to mix room air, which is rich in moisture and oxygen, into the shielding gas and contaminate the weld pool. In addition, excessive turbulence can reduce the area of the workpiece which is covered by the shielding gas. This can be seen by comparing Figure 2.10a, which shows excellent coverage of the workpiece and a consistent gas plume, with Figure 2.10c, which shows a smaller gas plume and inconsistent coverage.

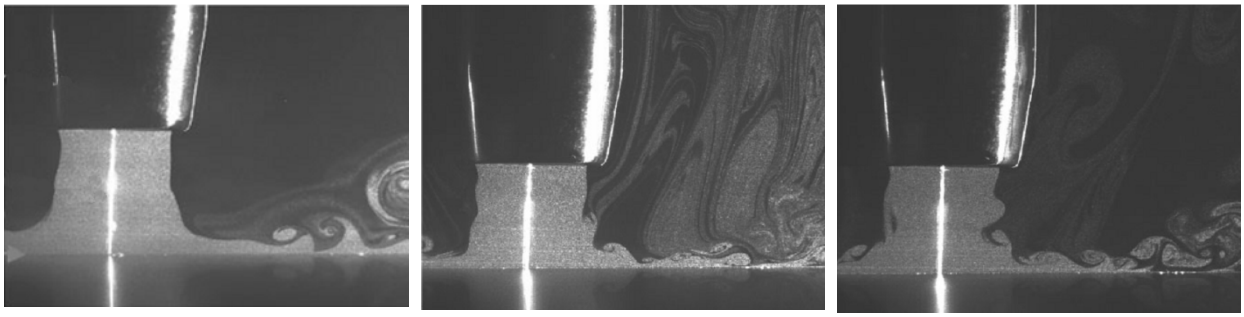

a) b) c)

Figure 2.10: Shielding gas flow through a GMAW nozzle with: ***a)*** Re=1260; ***b)*** Re=1680; ***c)*** Re=2100; (taken from Johnson *et al.* [60]).

The effect of travel speed on shielding gas width was also investigated by comparing the width of the shielding gas cloud at different travel speeds. Although the travel speed was found to have very little effect on the size of the shielding gas field, the wall jet separated closer to the nozzle centerline in the radial mean flow direction at higher travel speeds.

2.3 Summary

Previous studies by Y.M. Zhang and S.B. Zhang fabrication [38] - [43], have successfully used the keyhole-mode DSAW process to produce butt-joint configuration welds in thick plates. More recently, Kwon and Weckman [45], and Moulton and Weckman [46] have successfully used the conduction-mode DSAW process to produce butt-joint configuration welds in thin aluminum sheet. Acceptable welds were made between sheets of equal thickness at speeds of up to 60 mm/s at a welding power of 3.4 kW. Welds with good mechanical properties were made between sheets of dissimilar thickness at speeds of up to 25 mm/s at a welding power of 2.2 kW. However, the feasibility of using the DSAW process to produce lap-joint configuration seam or spot welds has not yet been explored. Lap-joint configuration welds are commonly used in the automotive industry and the aim of this study was to determine whether DSAW is

a viable alternative to RSW or LBW. The following chapter explains the experimental procedures and apparatus used to investigate the feasibility of lap-joint configuration seam welds in 1.0 mm thick AA5182 sheet.

Chapter 3: Experimental Apparatus and Procedures

3.1 Double Sided Arc Welding System

The double-sided arc welding (DSAW) apparatus uses a single power supply to produce an arc across two liquid cooled plasma torches. The various components of the apparatus of the system are shown in the schematic in Figure 3.1 and in the photos in Figure 3.2. Each plasma torch was connected to the power supply through a plasma console. These plasma consoles provide control over the pilot arc and gas flow rate for each PAW torch. The weld specimens were clamped into place on the welding table, which also provided a fixed mounting point for the plasma torches. A microcontroller based data acquisition system was used to measure welding current and voltage and also to provide control over the welding speed. This system is unique compared to other DSAW systems since two VPPAW torches and two plasma consoles are used to facilitate arc initiation via the integral pilot arc in each torch at any location along a lap joint.

3.1.1 The Arc Welding Table

A custom-designed DSA welding table was used in this study that consisted of a moving carriage that held and moved the specimens between the two torches and a stationary frame that allowed access to the workpiece from both sides. The stationary part of the frame was fastened to the floor and provided a fixed mounting point for components of the DSAW system. Figure 3.3 shows a schematic of the cold-rolled steel clamping fixture used to secure the welding specimens to the carriage. The specimen was clamped in place by tightening the bolts on the upper clamping bar, moving it towards the lower clamping bar.

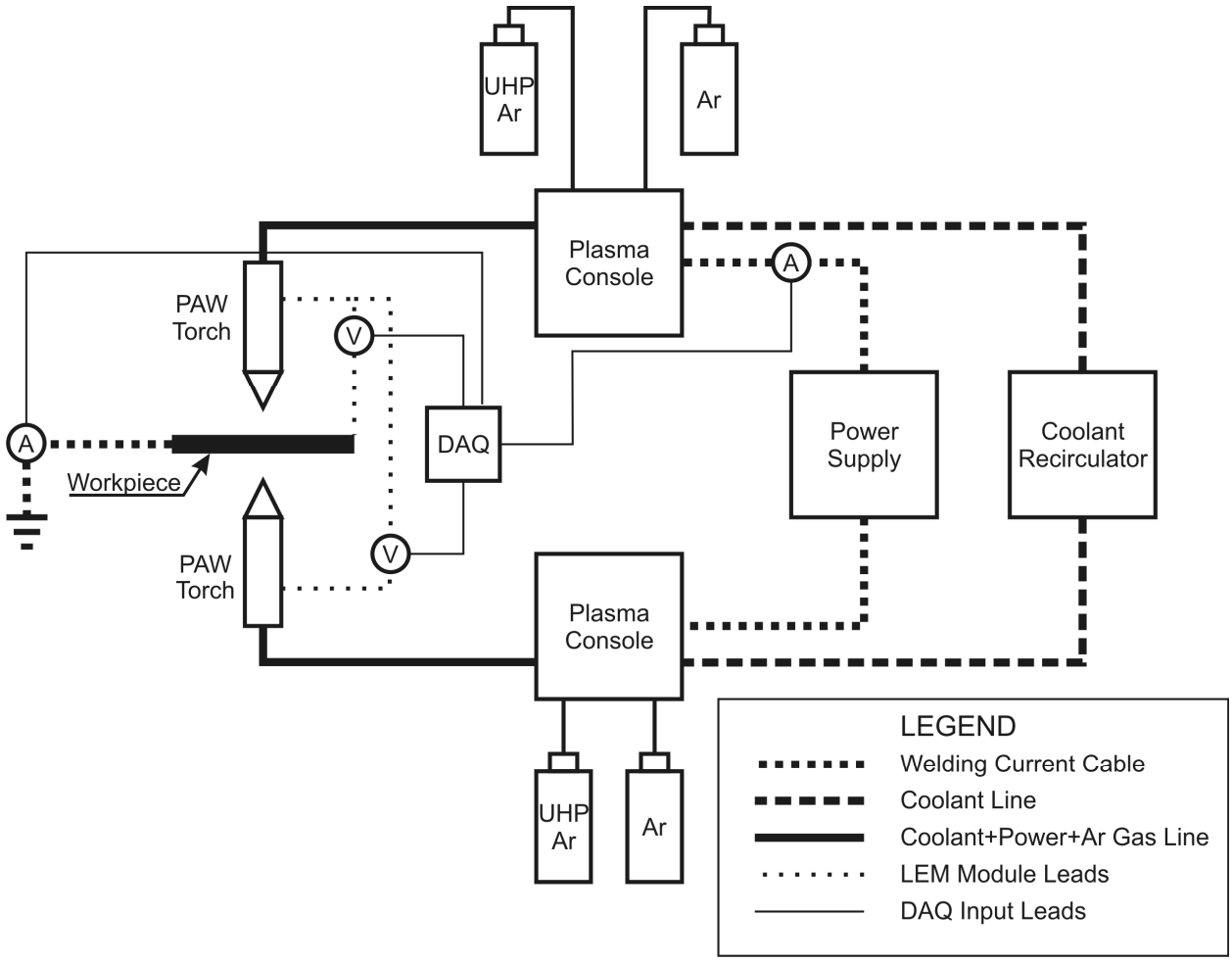

Figure 3.1: Schematic diagram of the main components of the DSAW system.

The moving carriage was mounted to the stationary frame and traversed the length of the table on a set of linear bearings and rails. The carriage was capable of speeds between 0 to 90 mm/s and was connected to a DC motor using a lead screw with a 10:1 gear reduction. The DC motor was controlled by a servo-motor controller which received a ±10 V input signal from a National Instruments PCI 6024E data card, which itself received inputs from a Labview program. Limit switches mounted at opposite ends of the table allowed a total travel distance of 0.9 m.

(a) (b)

Figure 3.2: Photographs of the DSAW system showing the: ***a)*** the Miller Aerowave power supply, both Thermal Arc plasma consoles, and coolant recirculator; ***b)*** welding table, two PAW torches, and voltage and current sensors.

The welding carriage and welding table were electrically grounded to a copper grounding rod using a flexible braided Cu strap in accordance with CSA Standard W117.2-M87 [63] to prevent electrical shocks to the operator while welding. In addition, PVC plates were placed in between the linear bearings and the carriage to electrically insulate the bearings and prevent current from flowing through the table and into the bearings.

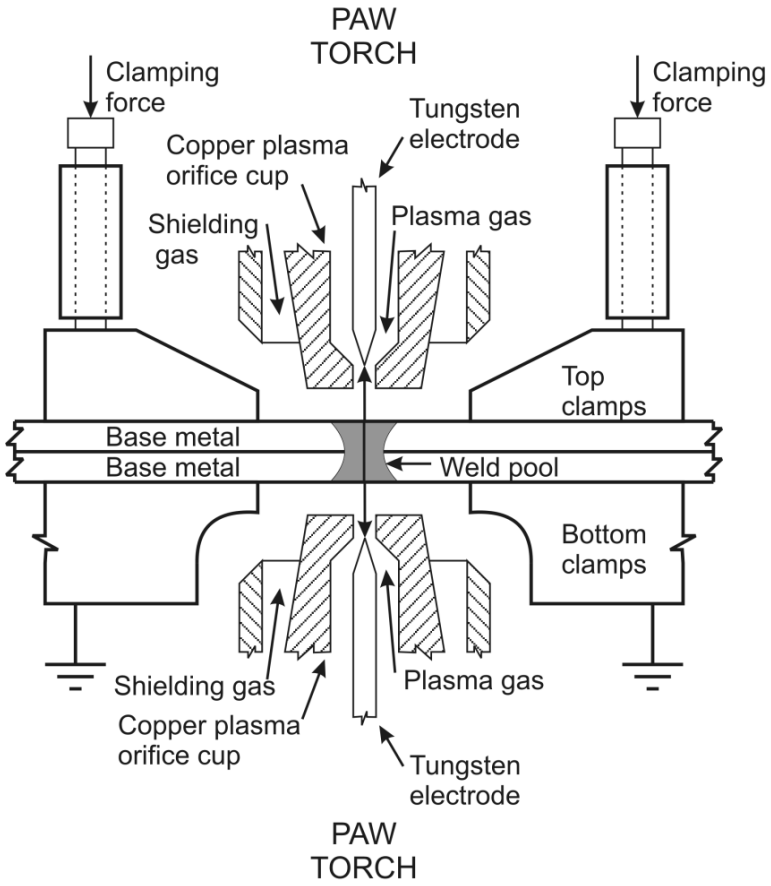

Figure 3.3: Schematic diagram of the DSAW clamping fixture and PAW torches.

3.1.2 The Arc Welding Torches

A Thermal Arc WC100B Model 300 PAW Torch and a B&B Precision Machining PAW Torch were used in this study. The Thermal Arc torch was mounted above the weld specimen while the B&B torch was mounted below as shown in Figure 3.4. Each torch was mounted to the welding table using a rack and pinion mechanism that allowed adjustment of the torch-to-workpiece distance.

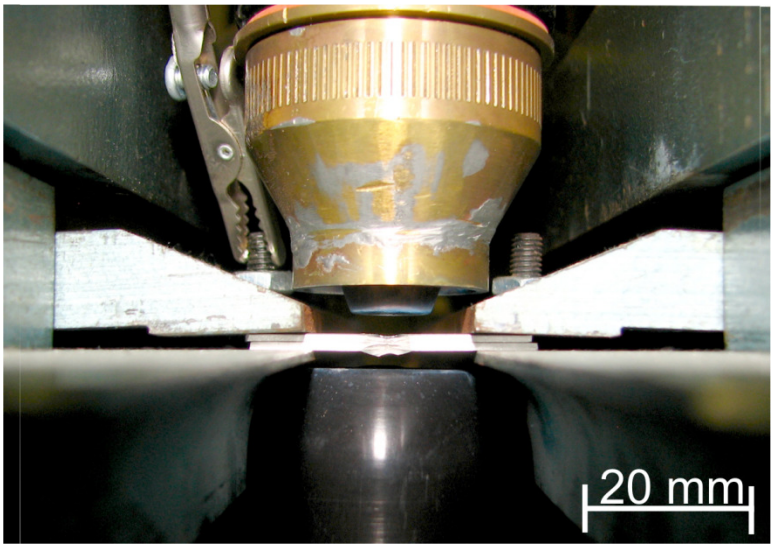

Figure 3.4: Clamping bar securing a specimen between the two PAW torches.

3.1.3 The Plasma Consoles

The Thermal Dynamics Thermal Arc WC100B plasma consoles used in this study served three purposes. Firstly, the plasma console initiated and controlled the pilot arc between the electrode and the orifice cup which was used to start the main arc in each plasma torch. Secondly, the plasma console connected each torch to the power supply and coolant recirculator. Lastly, the plasma consoles were used to control the plasma gas and shielding gas flow rate. The plasma console offered two settings for the pilot arc: normal and continuous mode. In normal mode, the pilot arc was shutdown once the main arc was started. In continuous mode, the pilot arc was left running continuously alongside the main arc. All experiments in this study were conducted in continuous mode, since previous literature had shown that this provided improved arc consistency when welding with an alternating current [54]. Coolant was circulated through both PAW torches and the plasma consoles by a Thermal Dynamics Corporation

HE100A Coolant Recirculator. The coolant solution contained 75% deonized water and 25% ethylene glycol.

3.1.4 The Power Supply

All experiments in this study were performed using a Miller Aerowave hybrid AC/DC constant current power supply which outputted a variable polarity square wave alternating current. A sample waveform is shown in Figure 3.5. The Thermal Arc torch was connected to the negative terminal of the power supply while the B&B torch was connected to the positive terminal. All experiments in this study were conducted using a symmetrical waveform, since it had been demonstrated by Kwon and Weckman [45] to provide a good balance between cathodic cleaning and penetration during DSA welding.

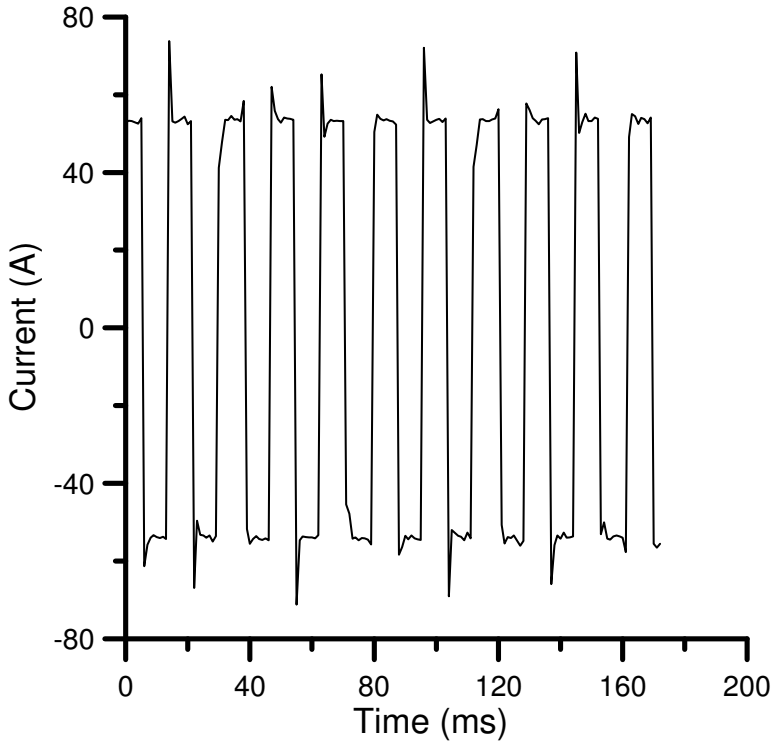

Figure 3.5: Example of a variable polarity square wave alternating current with a balanced waveform.

3.1.5 Data Acquisition System

The welding current and voltage for each weld produced in this study was measured and recorded by a set of Labview programs using a Pentium III-based Windows-PC microcomputer. The welding current between the top torch and the power supply was measured using a LEM LT505-S Hall-effect current transducer. This transducer was capable of measuring currents over a range of 100 mA to 500A with frequencies up to 150 kHz and was factory calibrated to within ± 0.1A. A schematic of this circuit is shown in Figure 3.6. Another LEM LT505-S current transducer was used to measure any stray welding current that may have flowed from the welding table to ground. The torch voltage was measured using voltage leads connected to the body of the bottom torch and to the coolant supply line of the top torch. A third lead was connected to the clamping bars to measure the torch-to-workpiece voltage. The voltage across the leads was measured using two LEM LV100 Hall-effect voltage transducers capable of measuring voltages over a range of 200mV to 50V. Both transducers were factory calibrated to within ±0.01 V. A schematic of this circuit is shown in Figure 3.7. One transducer was installed to measure the voltage across the top torch and the workpiece, while the second voltage transducer was installed to measure the voltage across the two torches.

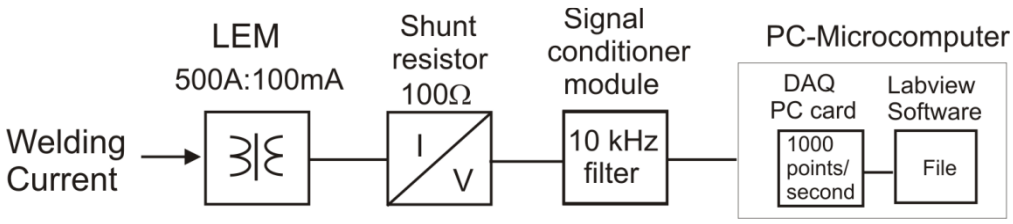

Figure 3.6: Schematic of the circuit used to measure welding current (taken from Deutsch [11])

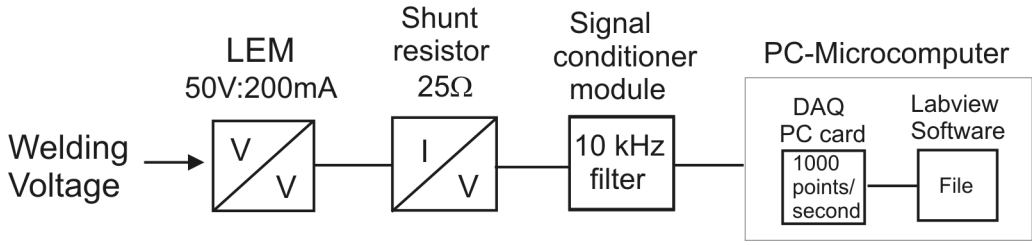

Figure 3.7: Schematic of the circuit used to measure welding voltage (taken from Deutsch [11]).

The outputs from the current and voltage transducers were measured using a National Instruments SCXI 1120 signal conditioning module. As shown in Figure 3.6 and Figure 3.7, these signals were sent through a low pass filter with a 10 kHz cutoff frequency to prevent damage to the data acquisition system from high frequency signals such as those generated by the pilot arc starter and the power supply inverter. Finally, the data was processed by a Labview program to calculate the RMS current, voltage, power, and resistance.

The Labview panel interface shown in Figure 3.8 allows the operator to manually adjust the position of the welding carriage with respect to the two welding torches. A set-point voltage signal with an output range of -10 V to +10 V was produced in the National Instruments 6024E card based on the desired welding speed. The "On/Off" button was used to start the DC motor and the "Forward" and "Backward" buttons were used to specify the direction of movement. The output signal was relayed to a National Instruments SCXI 1138 output module which in turn transmitted the voltage signal to the DC servo-motor controller. The linear relationship between speed and voltage is shown in Equation 3.1, and was verified for accuracy prior to welding.

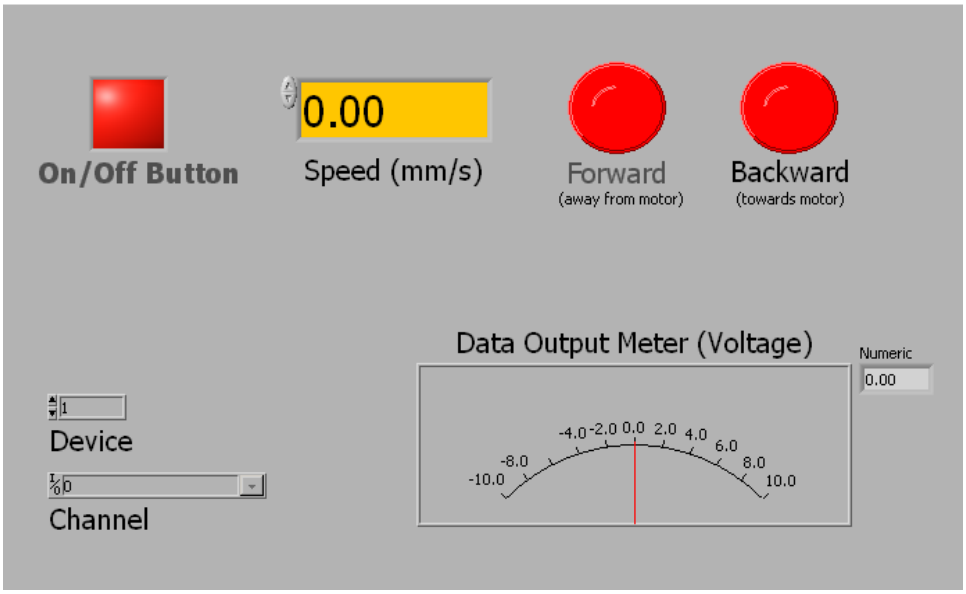

Figure 3.8: Front panel of Labview program used to move the welding carriage.

$$output\ voltage(v) = (welding\ speed\ (\frac{mm}{s})) * 0.0163 + 0.0235 \quad (3.1)$$

The Labview panel interfaces shown in Figure 3.9 and Figure 3.10 were used to move the welding specimen through the arc and to acquire voltage and current measurements from the transducers. The panel shown in Figure 3.9 was used to specify welding speed and to specify the number of data samples to be acquired. The scan rate was set to 1000 Hz based on previous research which determined that this value provided accurate characterization of the current and voltage waveforms without oversampling the data [11]. A delay feature was used to delay the start of data acquisition until the weld pool reached steady state conditions. The panel shown in Figure 3.10 was used to enter the preset welding variables.

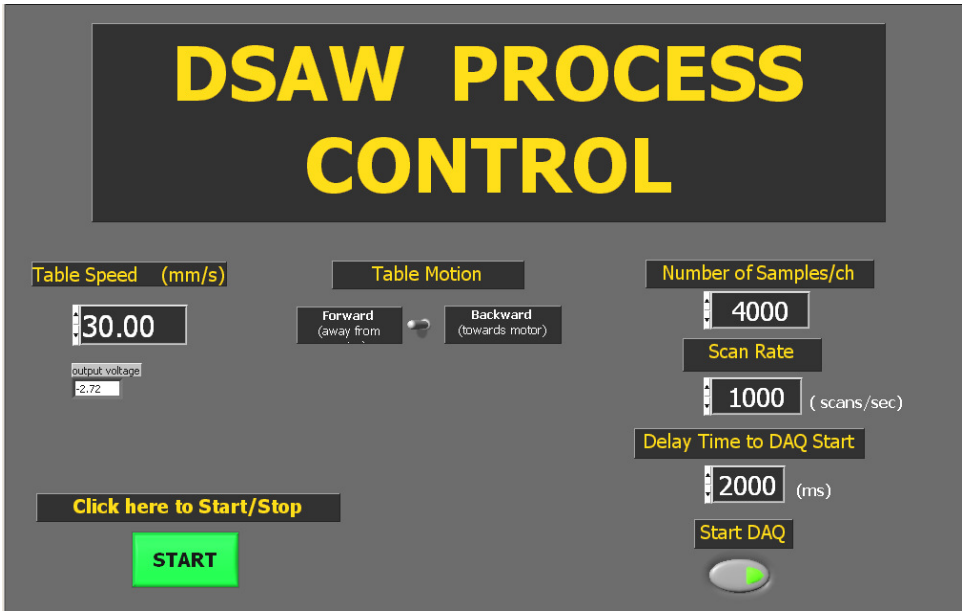

Figure 3.9: Front panel for data acquisition and carriage movement.

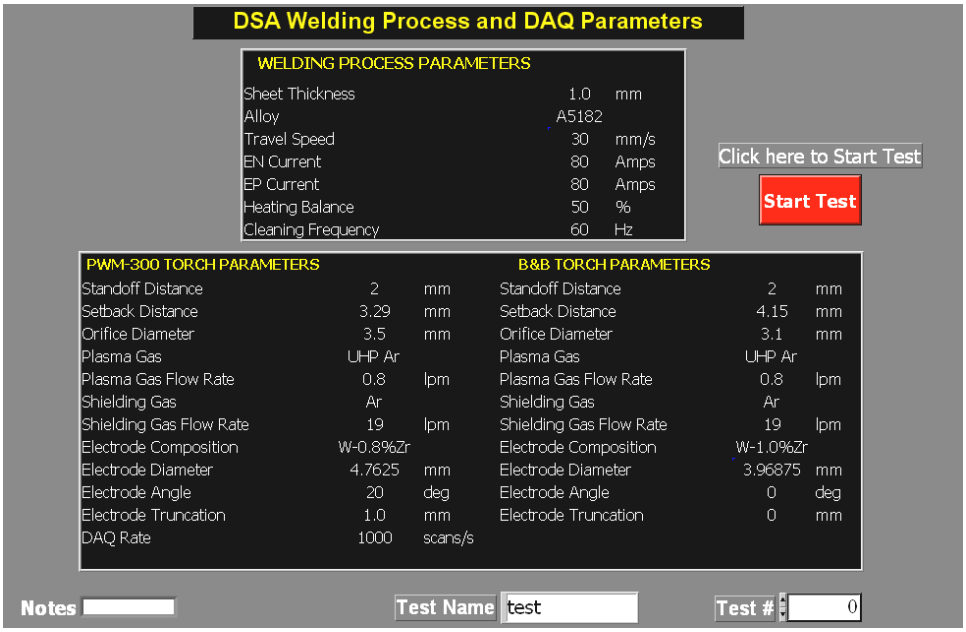

Figure 3.10: Panel of Labview program used to specify the pre-set welding parameters.

After the data acquisition was completed, the Labview program would calculate the RMS voltage and current from the measured voltage and current using the following equations:

$$I_{EN\_RMS} = \sqrt{\frac{\sum_{i=1}^{n}(I_{EN}(i))^2}{n}} \tag{3.2}$$

$$I_{EP\_RMS} = \sqrt{\frac{\sum_{i=1}^{n}(I_{EP}(i))^2}{n}} \tag{3.3}$$

$$V_{EN\_RMS} = \sqrt{\frac{\sum_{i=1}^{n}(V_{EN}(i))^2}{n}} \tag{3.4}$$

$$V_{EP\_RMS} = \sqrt{\frac{\sum_{i=1}^{n}(V_{EP}(i))^2}{n}} \tag{3.5}$$

$$I_{RMS} = \sqrt{(I_{EN\_RMS})^2(I_{EP\_RMS})^2(1-\theta)} \tag{3.6}$$

$$V_{RMS} = \sqrt{(V_{EN\_RMS})^2(V_{EP\_RMS})^2(1-\theta)} \tag{3.7}$$

$$P_{RMS} = V_{RMS} * I_{RMS} \tag{3.8}$$

$$R_{RMS} = V_{RMS} \div I_{RMS} \tag{3.9}$$

where

I_{EN}	is the magnitude of the electrode negative current
I_{EP}	is the magnitude of the electrode positive current
I_{EN_RMS}	is the RMS value of the EN current
I_{EP_RMS}	is the RMS value of the EP current
V_{EN}	is the magnitude of the voltage during EN polarity
V_{EP}	is the magnitude of the voltage during EP polarity
V_{EN_RMS}	is the RMS value of the EN voltage
V_{EP_RMS}	is the RMS value of the EP voltage
P_{RMS}	is the RMS power
R_{RMS}	is the RMS resistance
n	is the number of data samples
θ	is the fraction of time spent in EN mode

These variables are shown schematically in Figure 3.11. This data, along with the preset welding variables, were exported to a Microsoft Excel file.

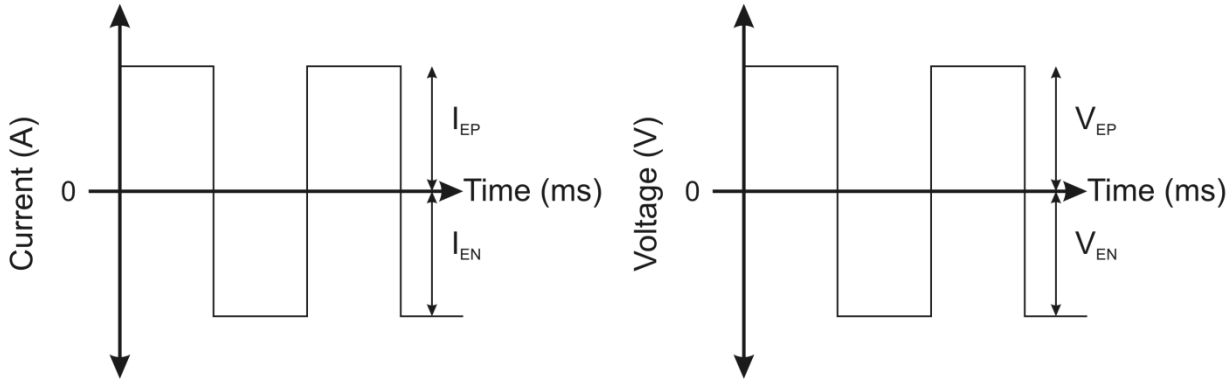

a) b)

Figure 3.11: Schematic diagrams of welding variables showing: ***a)*** welding current versus time; ***b)*** welding voltage versus time.

3.2 Materials

Welds were produced in 1 mm and 1.5 mm thick sheets of non-heat treatable AA5182-O alloy (cold rolled, annealed and recrystallized). This alloy contains 4.5%-wt Mg for solid-solution strengthening while retaining good formability characteristics. The 5xxx series of aluminum alloys is known for its good welding characteristics and its ability to be welded autogeneously with minimal risk of solidification cracking [58]. The nominal composition of this alloy is shown in the table below. During this study, 1 mm thick sheets of heat treatable AA6111 alloy were also used to study the fluid flow in the molten weld pool. The 6xxx series of aluminum alloy is known to provide moderate strength in relation to other heat-treatable alloys with good formability. However, the 6xxx series is also known to be susceptible to solidification cracking, liquation cracking, and HAZ degradation [24].

Table 3.1: Nominal composition (wt%) of AA5182-O and AA6111 [6], [64]

Alloy	Mg	Mn	Fe	Si	Cu	Cr	Zn	Ti	Zr	Al
5182-O	4.50	0.35	0.35	0.2	0.15	0.15	0.25	0.1	<0.01	Bal
6111	0.8	0.3	0.4	0.9	0.7	0.1 max	0.15 max	0.10 max		Bal

Table 3.2: Nominal thermal and mechanical properties of AA5182-O [6]

T_s (K)	T_l(K)	ρ (Mg/m^3)	C_p (J/kgK)	ΔH_f (KJ/kg)	Surface Tension (N/m)	σ_y (MPa)	UTS (MPa)	Elongation (%)
850	911	2.65	904	396	0.605	138	275	25

3.3 Weld Specimens

Welds made using a combination of 5182 and 6111 alloys were welded on specimens measuring 35 mm × 125 mm. All other welds were produced using weld specimens measuring 35 mm × 110 mm. All specimens were sheared to size perpendicular to the rolling direction as previous research indicated that this provided the best cathodic cleaning [11], [12]. Prior to welding, specimens were degreased using acetone and methanol, immersed in a 5% NaOH solution heated to 70° C for 2 minutes, rinsed in cold water, immersed in an as received HNO_3 solution for 1 minute, rinsed with hot water, dried, and then manually stainless steel wire brushed.

3.4 Experimental Procedures

The following list explains the procedure that was followed prior to welding.

Table 3.3 lists the preset welding constant welding torch parameters used for all experiments.

1. A sharpened electrode was placed in the top torch such that the electrode tip protruded from the orifice tip
2. The condition of the blunt tip electrode for the bottom torch was examined. If necessary the electrode was ground flat
3. The alignment of the top and bottom torches was verified by raising the bottom torch up to its maximum height and lowering the top torch so that the protruding electrode from the top torch was centered in the orifice of the bottom torch
4. Once the two torches were aligned, the protruding electrode in the top torch was pushed back into the torch body at a specific setback distance shown in Figure 3.12
5. The fume hood, power supply, plasma consoles, and coolant recirculator were turned on
6. The plasma gas was purged for 5 min, and the shielding gas was purged for 2 min
7. The two torches were set 6 mm apart from each other and a free standing arc at 50 A was left running for 5 min to melt the electrode tip into a ball-shape
8. Weld specimens were placed onto the weld carriage. The specimens were clamped into place by tightening a series of 5/16" diameter, 18 threads/inch socket head cap screws using a pneumatic ratchet
9. Prior to each weld, the plasma gas and the shielding gas were purged for 1 min
10. The torch-to-workpiece distance was set using spacer-blocks
11. The desired welding parameters were entered at the power supply and the flow rates for the plasma gas and shielding gas were adjusted on the plasma consoles to the required values
12. The welding arc was started and allowed to run as a free-standing arc for one minute

13. The Labview based control and data acquisition system was started
14. After the specimen passed through the welding arc and a weld was produced the main welding arc and the pilot arc were shut off and the torches were allowed to cool down
15. The welding specimen was removed from the clamps
16. The welding table was moved back to the starting position

Table 3.3: Constant present welding parameters used for producing DSA welds.

Torch Parameter	**Top Torch**	**Bottom Torch**
Standoff Distance	2 mm	2 mm
Setback Distance	4 mm	4.15 mm
Orifice Diameter	3.1 mm	3.1 mm
Plasma Gas	UHP Argon	UHP Argon
Plasma Gas Flow Rate	0.45 l/min	0.45 l/min
Shielding Gas	Argon	Argon
Shielding Gas Flow Rate	10 l/min	10 l/min
Electrode Composition	W-0.8%Zr	W-1.0%Zr
Electrode Diameter	4.76 mm	3.97 mm
Electrode Angle	20°	0°
Electrode Truncation	1 mm	0 mm

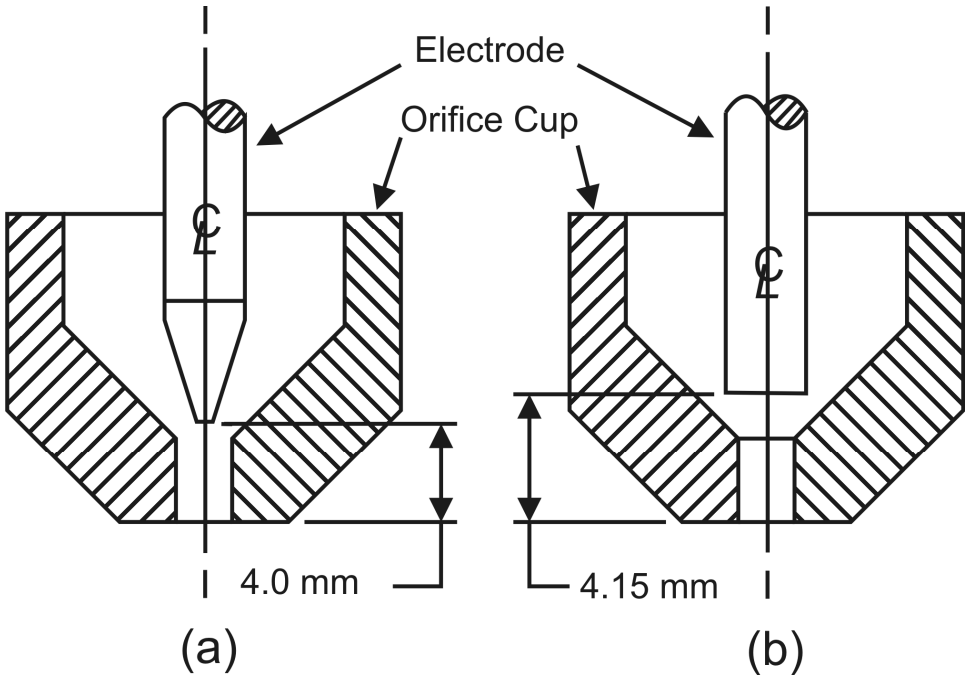

Figure 3.12: Schematic showing the electrode setback required for the: ***a)*** top Thermal Arc PAW torch; ***b)*** bottom B&B PAW torch.

Experimental Series A: was carried out to determine the welding conditions which would minimize porosity. A series of welds were produced to determine the best specimen cleaning procedure. Another series of welds were produced using different torch-to-workpiece distances and shielding cup designs to determine the effects of turbulent shielding gas flow on porosity formation. All experiments were performed on 1.5 mm thick AA5182 using a welding current of 80A and a welding speed of 30 mm/s. The effectiveness of the various cleaning procedures and the effect of turbulent shielding gas flow on porosity formation were determined by measuring the area fraction of porosity in six cross-sectional images from each weld specimen.

Experimental Series B: was carried out to determine whether the DSAW process could produce visually acceptable, defect free spot welds between two 1 mm thick AA5182 sheets. A series of welds were produced over a range of welding currents and dwell times to determine a range of acceptable values. All experiments were performed using a 2 mm standoff. Another series of welds were produced to investigate the effects of gradually decreasing the welding current on hydrogen porosity in the spot welds.

Experimental Series C: was carried out to investigate the optimal welding parameters that would produce visually acceptable and defect-free seam welds in the lap-joint configuration between two sheets of 1 mm thick AA5182. Welds were made using welding powers of 2 kW, 3 kW, 4 kW, and 5.1 kW at welding speeds of 5 to 75 mm/s, in increments of 5 mm/s. If blowholes were produced at a given power due to excessive heat input, further welds were not made at even slower speeds. If insufficient penetration was seen at a given power due to insufficient heat input, further welds at even higher welding speeds were not conducted.

Experimental Series D: was carried out to visualize the fluid flow in the DSA weld pool. Lap-joint configuration seam welds were produced between 1 mm thick sheets of AA6111 alloy and 1 mm thick sheets of AA5182 alloy. Welds were produced using a total welding power of 2kW at speeds of 10 mm/s and 15 mm/s. Samples were etched in Kellers reagent to visualize any fluid flow that may have taken place as delineated by the distinct differences in etched microstructures.

3.5 Post Weld Analysis of Double-Sided Arc Welds

3.5.1 Metallographic Examination

Transverse cross-sections of the welds were prepared by using a chop-saw to cut three sections from each welding specimen at least 50 mm from the end of the weld. The cut samples were mounted in a Struers Epofix cold mounting resin. Specimens were allowed to cure at room temperature for at least 12 hours. Once cured, the samples were ground flat on a belt grinder and then ground using a Struers Pedemax-2 automatic grinder/polisher with 320, 600, 800, 1200C, and 1200F grit silicon carbide paper using water as a lubricant. After grinding, the samples were polished on a Microstar 2000 Forcipol 2V grinder/polisher using a LECO Lecloth polishing cloth, a LECO 1μm diamond spray, and a LECO microid diamond extender as a lubricant. Specimens which required a finer finish were polished on a LECO Black CAMEO pad using LECO colloidal silica. Polished samples were etched with Keller's reagent, shown in Table 3.4, for 20 seconds.

Table 3.4: Composition of Keller's reagent [65]

Chemical	HNO_3	HCL	HF	H_2O
Quantity	2.5 mL	1.0 mL	1.5 mL	95 mL

Imaging of the finished samples was performed using the IMAGE-PRO 4.5 image analysis system together with an OLYMPUS optical microscope and OLYMPUS C-35AD-4 digital camera. Macro level images were taken using a Nikon Coolpix 8800, 8 megapixel digital camera.

3.5.2 Mechanical Property Evaluation

Porosity was measured using IMAGE-PRO 4.5 to count the number of pixels occupied by the gas pores. The total weld area was also measured using the IMAGE-PRO software. An average of six cross-sections was taken to improve the statistical relevance of the measurements.

Vickers micro-hardness testing was carried out in accordance with ASTM E92 Standard Test Method for Vickers Hardness of Metallic Materials [66]. Tests were performed using a Shimadzu Corporation HMV hardness tester using a 200 gram-force load and a constant spacing of 500 microns. Indentations were measured using the IMAGE-PRO 4.5 image analysis system and OLYMPUS optical microscope.

Transverse tensile testing was performed in accordance with ASTM E8M-04 Standard Test Method for Tensions Testing of Metallic Materials (Metric) [67]. A base metal sample and two specimens welded at a constant welding power of 2 kW and a welding speed of 15 mm/s and 20 mm/s were produced using the dimensions shown in Figure 3.13. Tests were conducted using an Instron tensile machine using a crosshead speed of 15 mm/min.

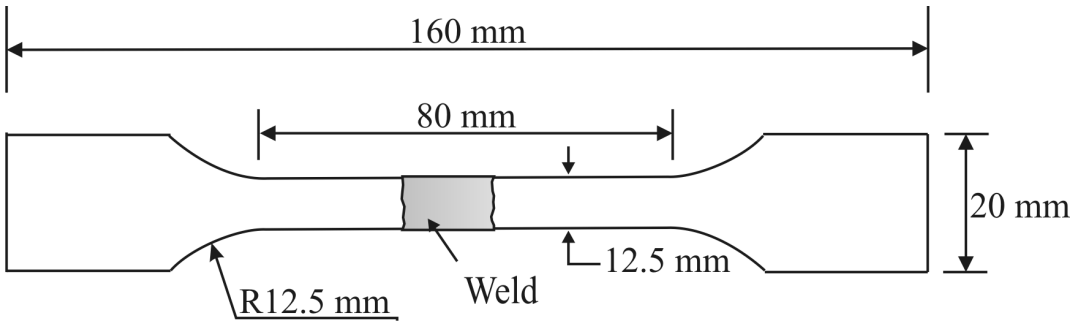

Figure 3.13: Tensile test specimen as per ASTM E 8M-04 [67].

Tension-shear tests were performed on DSA spot welds in accordance with the "Standard Methods for Testing Resistance Welds" specified in AWS C1.1-66 [68]. Two sets of tension-shear specimens were produced using the dimensions shown in Figure 3.14. One set of tension-shear specimens were made using nuggets produced using a 1.9 kW welding power and a 3 second weld time, and another set of specimens were made with nuggets that were produced with a 2.8 kW welding power and a 1 second weld time.

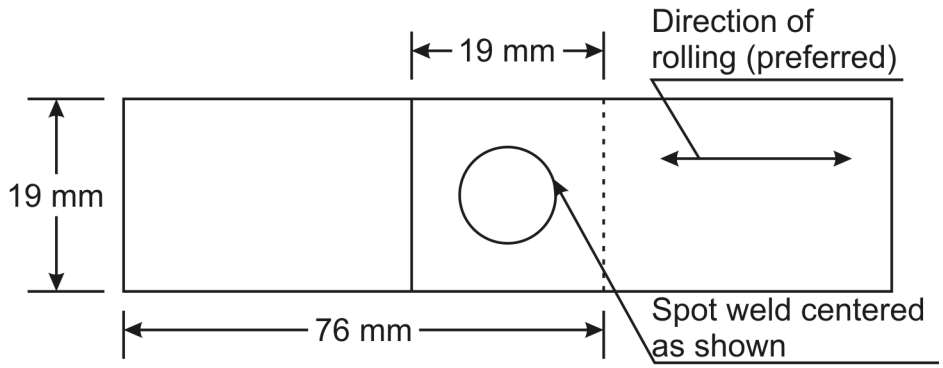

Figure 3.14: Tension-shear test specimen as per AWS C1.1-66 standard [68].

Chapter 4: Experimental Results and Discussion

The purpose of this chapter is to discuss and analyze the results of the four main experiments that were outlined in the previous chapter. The observations from Experimental Series A are shown in Section 4.1 and the effectiveness of various specimen pre-cleaning procedures on the area fraction of hydrogen gas porosity in the welds is discussed. The results from Experimental Series B, which was designed to examine the feasibility of using the DSAW process for producing spot welds, are described in Section 4.2. The feasibility of using the DSAW process for producing lap-joint configuration seam welds was examined in Experimental Series C and the results are shown in Section 4.3. Lastly, the observations from Experimental Series D, in which the different forces that might drive fluid flow inside the weld pool and disrupt the oxide films at the sheet interface in lap-joint configuration DSA welds, are presented and discussed in Section 4.4.

4.1 Porosity Reduction

Hydrogen gas porosity is formed easily during aluminum welding due to the presence of rolling lubricants, the tenacious hydrated aluminum oxide layer on the surface of the sheet, and from inadequate shielding of the molten aluminum from humid room air. Porosity is undesirable in welds, since it has been shown to reduce the mechanical properties of the weld metal, such as ductility, and act as a crack initiation point [44], [50], [69]. As a result, various welding standards specify the maximum amount of porosity that can be tolerated in a weld. For example, the AWS D8.14M/D8.14:2000 [70] specification for arc welded automotive components allows a maximum of 15% of porosity by area, while the Canadian Standards Association (CSA) W59.2 [71] standard for welded aluminum construction allows a

maximum of only 0.12% area fraction of porosity for sheet metal applications with a thickness of less than 3 mm.

In previous studies on DSAW of aluminum sheet by Kwon and Weckman [45], and Moulton and Weckman [46], welding specimens were degreased using acetone and methanol, and the oxide layer was removed using an electrically operated stainless steel power wire brush prior to welding. In their studies, this cleaning procedure was found to significantly reduce the amount of gas porosity and improve the consistency of the weld bead. Moulton and Weckman [46] found that welds produced using a 3 kW welding power and a shielding gas flow rate of 19 lpm contained an average porosity area fraction ranging between 0.05% and 0.09%, depending on welding speed. However, when bead-on-plate welds were produced during the present study using similar welding parameters, the average porosity area fraction was found to be 0.91%. Since these cleaning techniques and welding parameters had been used successfully in the past, it was thought that the new dual-VPPAW DSAW system was producing more porosity than the welds produced by the GTAW/VPPAW DSAW system used by Kwon and Weckman [45], and Moulton and Weckman [46].

4.1.1 Comparison between Dual-VPPAW DSAW System and VPPAW-GTAW DSAW System

A series of bead-on-plate welds were produced in 1.5 mm thick AA5182 sheet using the GTAW/VPPAW DSAW system and the dual-VPPAW DSAW system in order to determine whether the new dual-VPPAW DSAW system was responsible for the increase in porosity. The torch-to-workpiece distance was set at 2 mm and the shielding gas flow rate was set at 19 lpm. Welds were produced using a total welding power of 3.1 kW and a welding speed of 30 mm/s. All specimens were degreased using

acetone and methanol and the oxide was mechanically removed using a stainless steel wire brush. Two stainless steel wire brushing methods were studied in this experiment. A review of literature had suggested that a power wire brush may cause the aluminum oxide and other surface contaminants to become embedded in the specimen, and increase porosity [58]. To compare the effects of power brushing against manual wire brushing, one set of welds was produced with specimens that were manually wire brushed prior to welding, and another set was produced using specimens that were power brushed prior to welding.

Figure 4.1 compares the area fraction of porosity in the welds produced using the different welding systems. Welds produced using the GTAW/VPPAW system were found to contain 0.68 ± 0.50% porosity by area for manually wire brushed specimens, and 1.39 ± 0.85% porosity by area for power brushed specimens. Welds produced using the dual-VPPAW system contained an average of 0.48 ± 0.24% porosity by area for manually wire brushed specimens, while specimens that were power wire brushed contained 0.70 ± 0.45% porosity by area. The difference in porosity between welds produced by the GTAW/VPPAW process and the dual-VPPAW process was compared using a t-test with a level of significance of 0.05, assuming that the standard deviation of the two populations was unequal. Six replicates were used and the null hypothesis assumed that the average area fraction of porosity in the welds produced by the dual-VPPAW and GTAW/VPPAW DSAW systems was equal for welds produced in specimens that were manually wire brushed prior to welding. This hypothesis test was repeated for the welds that were power wire brushed prior to welding. The hypothesis test revealed that the dual-VPPAW system produced welds with a similar level of porosity as the GTAW/VPPAW system.

Another hypothesis test was conducted to compare the mean porosity fraction in welds produced in specimens that were manually wire brushed against welds which were power wire brushed prior to welding. Again, a t-test was used with a level of significance of 0.05 and assuming that the standard deviation of the two populations was unequal to test the null hypothesis that the average area fraction of porosity for manually wire brushed specimens and power wire brushed specimens was equal. The hypothesis test did not produce strong evidence to reject the null hypothesis, and specimens that were manually wire brushed were found to have a similar level of porosity as specimens that were power wire brushed.

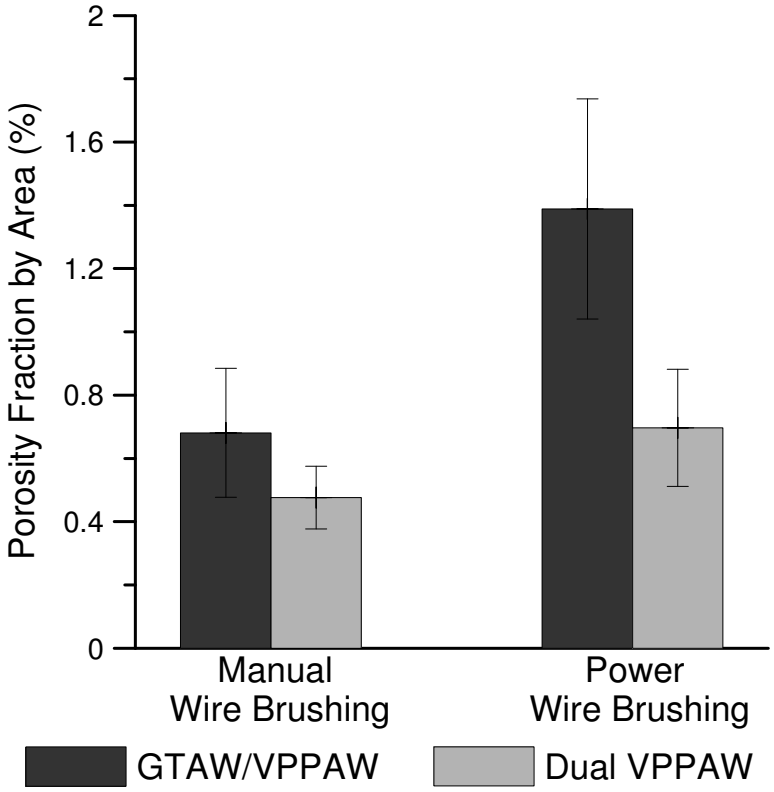

Figure 4.1: Porosity fraction by area (%) in dual-VPPAW DSA welds versus GTAW/VPPAW DSA welds when using manual and power stainless steel wire brushing of the oxide prior to welding.

4.1.2 Cleaning Techniques

Previous research by Kwon and Weckman [45], and Moulton and Weckman [46], had already demonstrated the importance of degreasing and stainless steel wire brushing prior to welding aluminum sheet if hydrogen porosity in the welds was to be minimized. Light degreasing and wire brushing may be adequate if the specimens have been kept clean and stored in a dry environment. However, the surfaces of the specimens used in this study were saturated with rolling lubricants and were covered in a thick, hydrated aluminum oxide layer. Therefore, a more aggressive cleaning technique was required to adequately clean the specimens.

Deoxidizers are often recommended for removing heavily oxidized and contaminated aluminum surfaces [58], [72]. For example, The Aluminum Association [58], recommended the following procedure:

1. Immerse the aluminum specimens in a 5% sodium hydroxide (NaOH) solution at a temperature of 70° C for up to 60 seconds to remove the hydrated oxide and any other surface contaminants.
2. Rinse with cold water.
3. Desmut the surface by immersing the specimens in concentrated nitric acid (HNO_3) at room temperature for up to 30 seconds.
4. Rinse in hot water and dry.

A similar procedure was also recommended by Bill Christy [73], a welding technologist at the Novelis Global Technologies Centre, Kingston ON, who suggested a 2 minute immersion in a sodium hydroxide solution, and a one minute immersion in a nitric acid solution.

A factorial design experiment was used to evaluate the effectiveness of the three different cleaning techniques by producing a series of bead-on-plate DSA welds in 1.5 mm thick AA5182-O sheet at a total welding power of 3.1 kW and a welding speed of 30 mm/s. The three factors considered in this experiment were: Factor A, degreasing using acetone and methanol; Factor B, deoxidizing in a 5% NaOH solution for 2 minutes at 70° C and desmutting in an as-received HNO_3 solution for one minute; and Factor C, stainless steel wire brushing the specimen prior to welding using either an electrically operated power wire brush or a manually operated wire brush. The average area fraction of porosity was calculated using measurements obtained from six transverse cross sections.

The factors and the resulting average area fraction of porosity are summarized in Table 4.1. Specimens welded in the as-received condition, as seen in Figure 4.2a, contained the highest average area fraction of porosity of 3.82 ± 1.42%. Welds produced in specimens that were degreased and manually wire brushed, as seen in Figure 4.2b, contained a lower average area fraction of porosity of 0.49 ± 0.24%. Lastly, welds produced in specimens that were cleaned using a combination of degreasing, deoxidizing, and manual stainless steel wire brushing, as seen in Figure 4.2c, contained the lowest average area fraction of porosity of only 0.12 ± 0.13%. All of the pores observed in the transverse cross-sections appeared to float towards the top of the weld, but failed to break through the top surface, perhaps due to the presence of an oxide film.

Table 4.1: Summary of factorial experiment used for evaluating various cleaning procedures.

Factorial Experiment Conditions			**Observed Porosity Area Fraction**	
Factor A: Degreasing with acetone and methanol	Factor B: Immersion in NaOH and HNO_3 solutions	Factor C: Stainless Steel Wire Brushing	Average Area Fraction of Porosity (%)	Standard Deviation (%)
no	no	no	3.82	1.43
no	no	manual	1.03	0.67
no	no	power	1.18	0.43
no	yes	no	0.73	0.58
no	yes	manual	0.29	0.19
no	yes	power	0.69	0.42
yes	no	no	1.39	0.76
yes	no	manual	0.49	0.24
yes	no	power	0.68	0.38
yes	yes	no	0.44	0.18
yes	yes	manual	0.12	0.13
yes	yes	power	0.15	0.18

An analysis of variance (ANOVA) was performed in Minitab [74] to determine the importance of the various factors and the interactions between them. A complete summary of the ANOVA is given in Appendix A. An analysis of the main effects revealed that all three cleaning procedures significantly reduced the amount of weld porosity, as shown in Figure 4.3. The plot also shows that manual wire brushing had a more significant effect on reducing porosity than power wire brushing. Second level interaction effects were also found to significantly reduce the area fraction of porosity, as shown in Figure 4.4. The plots show that combining two cleaning procedures yields better results than using only one procedure by itself. This was expected since both the rolling lubricants and the oxide layer need to be removed prior to welding. Lastly, the analysis also revealed that third level interaction effects were also significant. This suggests that the rolling lubricants were only sufficiently removed when the specimen has been degreased and deoxidized, and that the oxide layer is only sufficiently removed when the specimen has been deoxidized and wire brushed.

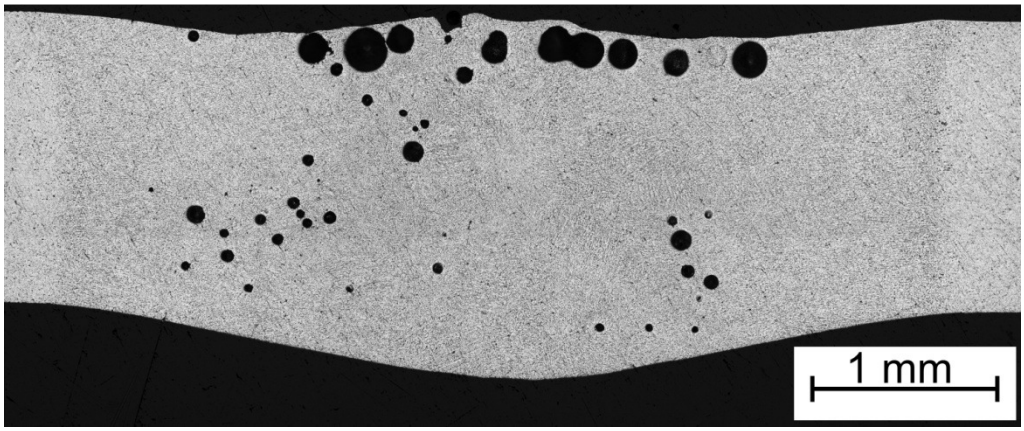

a)

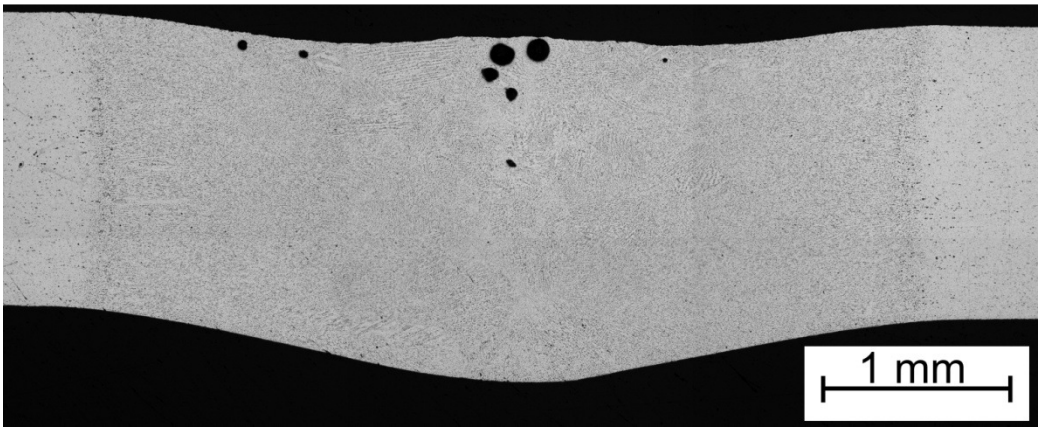

b)

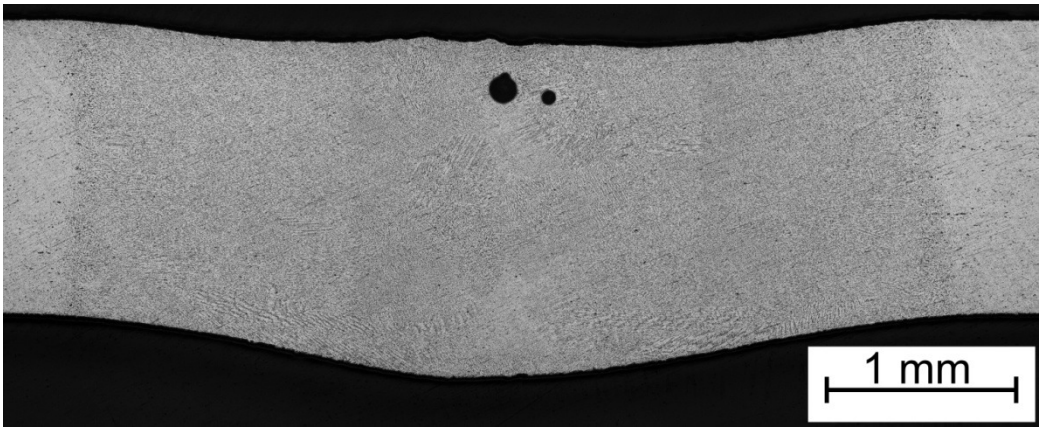

c)

Figure 4.2: Transverse cross-sections of welds produced using a welding power of 3.1 kW and a welding speed of 30 mm/s showing specimens cleaned using: ***a)*** as received; ***b)*** degreased and manually wire brushed; ***c)*** degreased, deoxidized, and manually wire brushed.

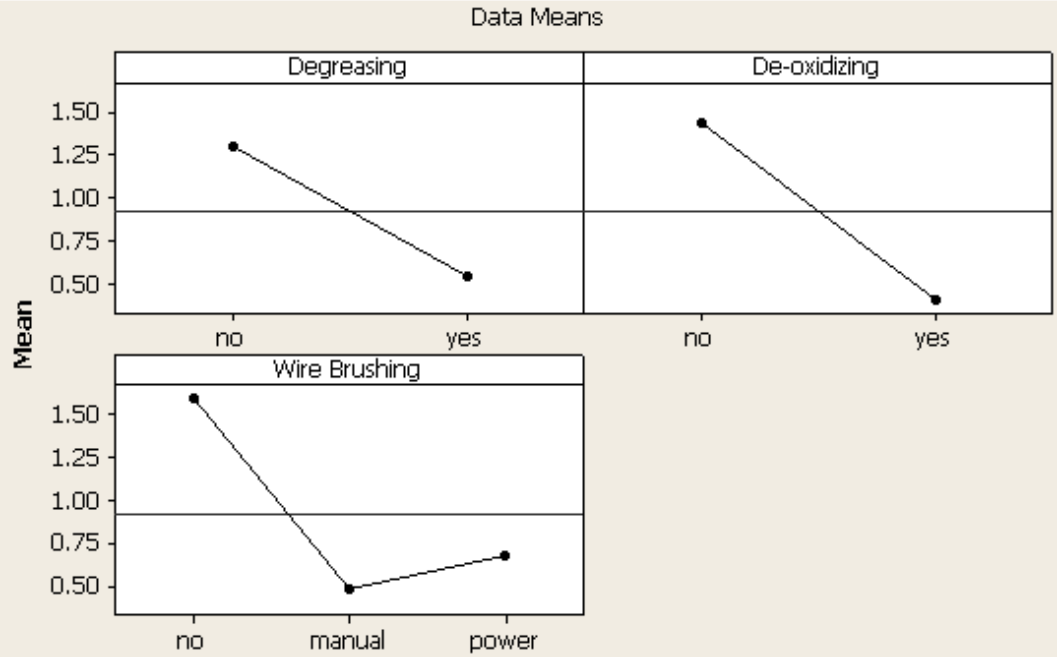

Figure 4.3: Main effects of degreasing, deoxidizing, and wire brushing on area fraction of porosity.

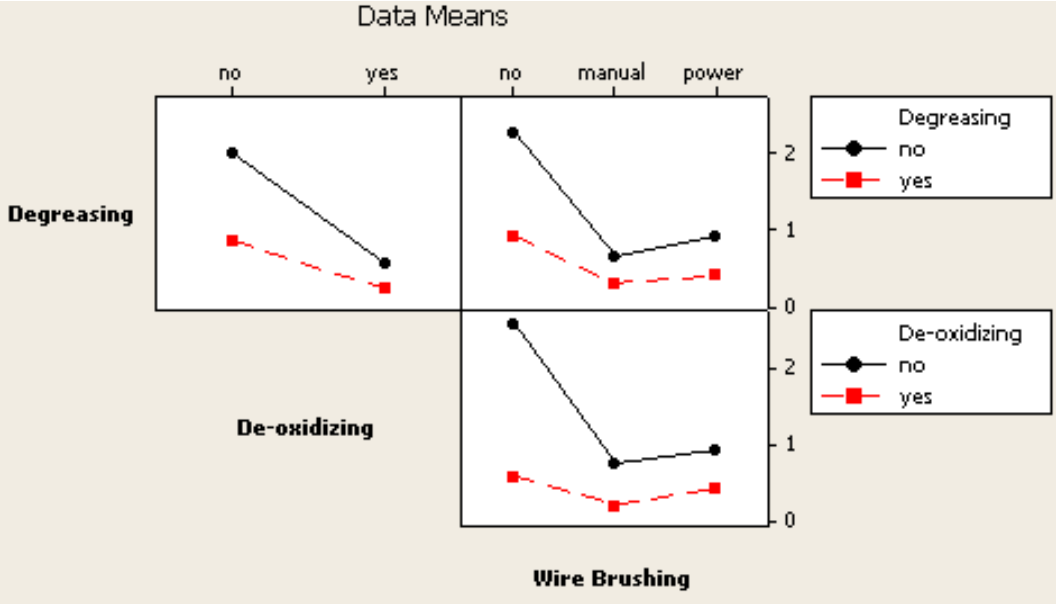

Figure 4.4: Interaction effects of degreasing, deoxidizing, and wire brushing on area fraction of porosity.

4.1.3 Comparison between VPPAW of Top Torch and VPPAW of Bottom Torch

Since the dual VPPAW DSAW system used in the present study was not found to produce a greater amount of porosity than the original GTAW/VPPAW DSAW system used by Kwon [45] and Moulton [46], it was believed that the B&B VPPAW torch may be responsible for the increase in hydrogen gas porosity observed using the dual VPPA torch system, since this was the only major component which changed over the previous DSAW system. To determine if this was true, a series of one-sided VPPA welds were produced in 1.5 mm thick AA5182 using a total welding power of 1.2 kW, a welding speed of 10 mm/s, a shielding gas flow rate of 19 lpm, and a torch-to-workpiece distance of 2 mm. All specimens were cleaned prior to welding using a combination of degreasing, deoxidizing, and manual stainless steel wire brushing. One set of welds was produced using the top Thermal Arc torch in the flat position while another set of welds was produced using the bottom B&B torch in the overhead position. Since hydrogen gas porosity tends to float upwards against the force of gravity, it was expected that the welds produced in the overhead position would have a slightly higher average porosity since the gas pores would not be able to float out from the weld pool surface. For each welding condition, the area fraction of porosity was measured in six transverse cross sections.

Welds produced using the Thermal Arc torch were found to contain an area fraction porosity of 0.48 ± 0.23%. Welds produced using the B&B Machining torch were found to contain an area fraction porosity of 0.43 ± 0.32%. A hypothesis test using 6 replicates was used to test the null hypothesis that the average area fraction of porosity in single-sided VPPA welds produced by the Thermal Arc torch and the B&B torch was equal. Using a t-test with a significance level of 0.05, and assuming that the standard deviation of the two populations was unequal, there was not enough evidence to reject the null hypothesis.

Therefore, the area fraction of porosity in VPPA welds produced using the Thermal Arc torch was found to be equal to the porosity in VPPA welds produced using the B&B torch.

4.1.4 Effects of Torch-to-Workpiece Distance

A series of welds were produced over a range of torch-to-workpiece distances of 2 mm, 3 mm, and 4 mm, to determine the effects of torch-to-workpiece distance on the formation of hydrogen gas porosity. At each torch-to-workpiece distance, three welds were produced at a shielding gas flow rate of 10 lpm, 15 lpm, and 19 lpm. The results from this series of welds are illustrated in Figure 4.5. Weld porosity was minimized when a high gas flow rate was used with a long torch-to-workpiece distance. Conversely, weld porosity increased when the shielding gas flow rate was reduced in welds produced with a long torch-to-workpiece distance. Weld porosity increased when a high gas flow was used with a short torch-to-workpiece distance. However, welds produced using a low shielding gas flow rate and a short torch-to-workpiece distance also had minimal porosity.

A series of hypothesis tests were performed using 6 replicates for each welding condition to compare the average area fraction of porosity in welds. A t-test was used to test the null hypothesis that the area fraction of porosity would be equal in welds produced at different torch-to-workpiece distances for a given flow rate. Welds produced using a torch-to-workpiece distance of 2 mm were found to have more porosity than specimens produced using a 3 mm or a 4 mm torch-to-workpiece distance at a flow rate of 19 lpm and 15 lpm. On the other hand, when welds were produced at a flow rate of 10 lpm, the average area fraction of porosity was found to be consistent at all three torch-to-workpiece distances. Overall, welds produced using high gas flow rates and low torch-to-workpiece distances were found to contain more porosity than welds produced with high gas flow rates and a high torch-to-workpiece distance.

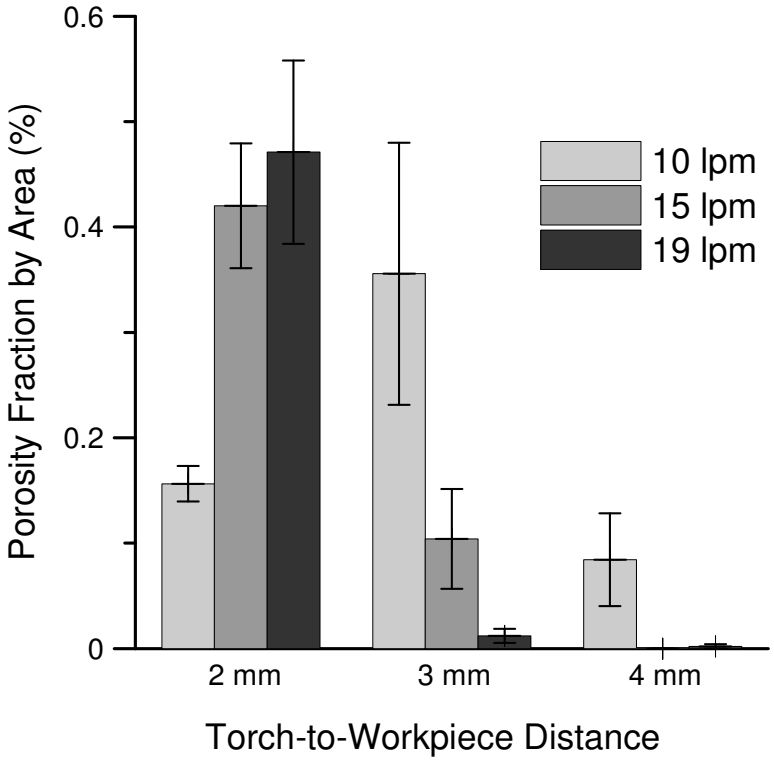

Figure 4.5: Porosity fraction by area (%) for welds produced using a 2.1 kW welding power, 30 mm/s welding speed, and 10, 15, and 19 lpm shielding gas flow rates.

Johnson *et al.*[60], observed increasingly turbulent structures at higher shielding gas flow rates in their flow visualization study of welding nozzle shielding gas jet flow during GMA welding. At a lower shielding gas flow rate, there was less turbulence due to the lower gas velocity and a more consistent shielding gas plume. In addition, the width of the jet was observed to increase continuously with distance from the nozzle exit and the kinetic energy and momentum of the shielding gas were found to decrease with distance. In other words, porosity may be reduced by decreasing the shielding gas flow rate to produce a more laminar flow, and therefore, a more consistent coverage of the weld pool or by increasing the torch-to-workpiece distance to produce a larger area of coverage by the shielding gas plume.

During the present study, the area fraction of porosity was very low when a high shielding gas flow rate was used with a long torch-to-workpiece distance, as shown in Figure 4.5. This may have been caused by a wider gas plume and a less energetic flow near the surface of the weld pool which would be less likely to entrain room air into the shielding gas plume. Conversely, the area fraction of porosity increased when a high shielding gas flow rate was used with a short torch-to-workpiece distance. This may be due in part to a narrower shielding gas plume and a more energetic, turbulent gas flow near the surface of the weld pool which could have enhanced mixing with room air and porosity-causing contaminants into the shielding gas plume. Overall, using a long torch-to-workpiece with a high shielding gas flow rate was found to produce the most significant reduction in gas porosity in the bead-on-plate welds. A short torch-to-workpiece distance with a low shielding gas flow rate was also found to reduce porosity, but this was found to be less effective compared to using a long torch-to-workpiece distance and a high shielding gas flow rate.

4.1.5 Effects of Shielding Gas Flow

Turbulence in the shielding gas plume is undesirable since the enhanced turbulent mixing in the flow can stir room air into the shielding gas and contaminate the surface of the molten weld pool with humid room air [17]. From the Reynolds number equation discussed in Section 2.2.3, higher velocities will increase the Reynolds number. Conversely, the Reynolds number will decrease as the cross-sectional area of the nozzle increases for a constant flow rate. Laminar flow and good shielding will exist at low Reynolds numbers; however, above a characteristic Reynolds number for each flow geometry, there will be a transition from laminar to turbulent flow with increasing mixing with room air and reduction in the quality of gas shielding of the weld pool surface. Although increasing the torch-to-workpiece distance was shown in the previous experiment to reduce porosity at certain shielding gas flow rates, increasing

the torch-to-workpiece distance also increases the torch voltage and decreases the process efficiency. Therefore, it would better to minimize the torch-to-workpiece distance and promote more laminar gas flow in the shielding gas nozzle.

One of the most commonly used methods for promoting laminar gas flow in GTA welding is a device known as a gas lens [17], [75]. A gas lens is a layered series of fine stainless steel wire mesh discs which are stacked together, as shown in Figure 4.6. The gas lens forces the shielding gas to flow through small gaps in the mesh and laminarizes the shielding gas flow. This and the flow restriction help to distribute the shielding gas more evenly around the shielding cup, increases the length of the laminar flow region, and reduces turbulence in the shielding gas plume.

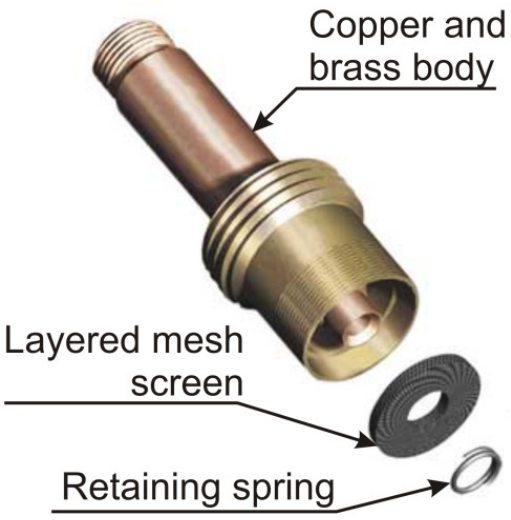

Figure 4.6: Exploded diagram showing a typical GTAW gas lens (taken from Miller Electric [75]).

A commercially available gas lens could not be found for either of the two VPPAW torches used in this study. Therefore, the existing shielding gas cup for the top Thermal Arc torch was modified to include three layers of 304 stainless steel mesh of 0.114 mm wire diameter spaced 0.140 mm apart, as

shown in Figure 4.7. In addition, the cross sectional area of the shielding gas tip was increased from 174 mm^2 to 380 mm^2 to reduce the gas velocity and the corresponding Reynolds number.

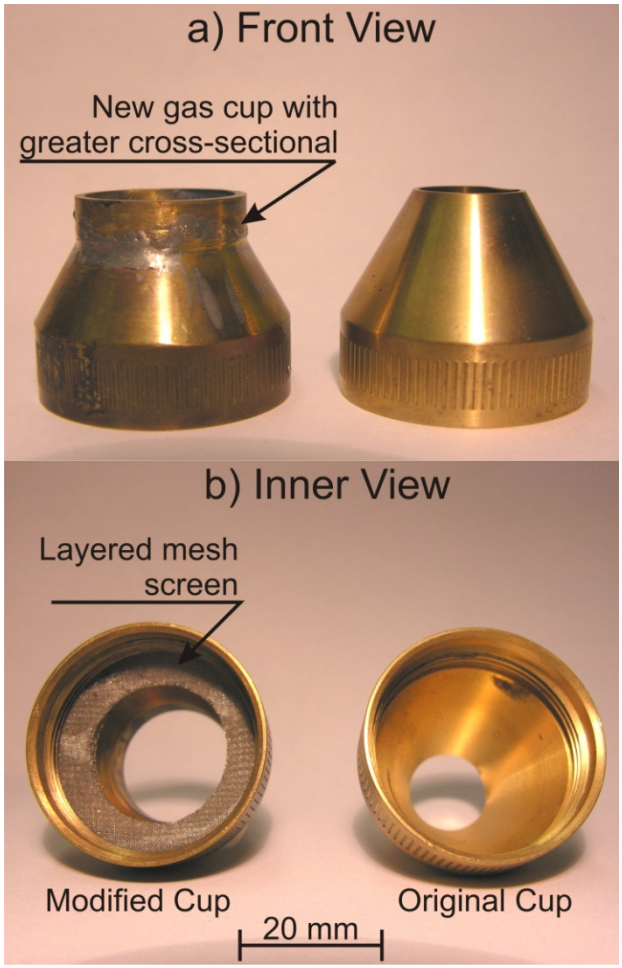

Figure 4.7: Photograph comparing modified shielding cup (L) original shielding cup (R) for the top Thermal Arc VPPAW torch showing: ***a)*** front view; ***b)*** inner view.

The shielding cup for the bottom B&B torch was modified by cutting the upper 12 mm of the shielding cup and replacing it with a constant-cross sectional area extension, as shown in Figure 4.8, thereby increasing the cross sectional area from 280 mm^2 to 615 mm^2. A gas lens could not be added into this shielding cup since there were not any convenient mounting points for the stainless steel mesh. The

Reynolds numbers for the original shielding cups and the new shielding cup designs are summarized in Table 4.2. These are approximate values and will vary in reality since the flow is not expected to be fully developed due to the relatively short entrance length, and because the shielding nozzles do not have smooth, constant diameter internal profiles [60], [62]. Based on these calculations, the Reynolds number was expected to decrease by 18% and 21% for the Thermal Arc torch and the B&B torch, respectively. However, since the shielding cup does not have a constant cross-sectional area, the actual Reynolds number may have been different from the calculated value. In addition, while the Reynolds number is frequently used to estimate the transition conditions from laminar to turbulent flow, the influence of using a gas lens on laminarizing the flow is not captured in the Reynolds number.

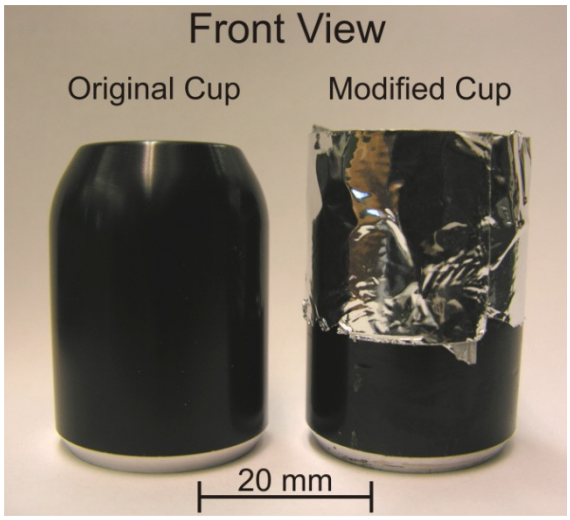

Figure 4.8: Photograph comparing original shielding cup (L) modified shielding cup (R) for the bottom B&B Machining VPPAW torch.

Table 4.2: Reynolds numbers for the original and redesigned shielding cups.

		Flow Rate:		
		19 lpm	15 lpm	10 lpm
Top Torch	Re (original design)	1106	873	582
	Re (new design)	907	716	477
Bottom Torch	Re (original design)	860	679	452
	Re (new design)	678	535	357

A series of welds were produced using a total welding power of 2.1 kW, a welding speed of 30 mm/s, and a torch-to-workpiece distance of 2 mm, to determine whether the new shielding cup design would have any effect on the formation of hydrogen gas porosity. All specimens were cleaned using the technique described in Section 4.1.2. Three sets of welds were produced for this section of the study. The first set was produced using the original shielding cup design on both torches. The second set of welds was produced using the modified shielding cup on the top Thermal Arc torch and the original shielding cup on the bottom B&B torch. The final set of welds was produced using the original shielding cup on the top Thermal Arc torch and the modified shielding cup on the bottom B&B torch. Each set of welds was produced using a shielding gas flow rate of 19 lpm, 15 lpm, and 10 lpm.

The area fraction of porosity from each of these welds is shown in Figure 4.9. Overall, the area fraction of porosity was highest when the modified bottom shielding cup was used, whereas the area fraction of porosity was lowest when the modified top shielding cup was used. When a high shielding gas flow rate was used, the welds tended to contain more porosity in comparison to welds produced using a low shielding gas flow rate.

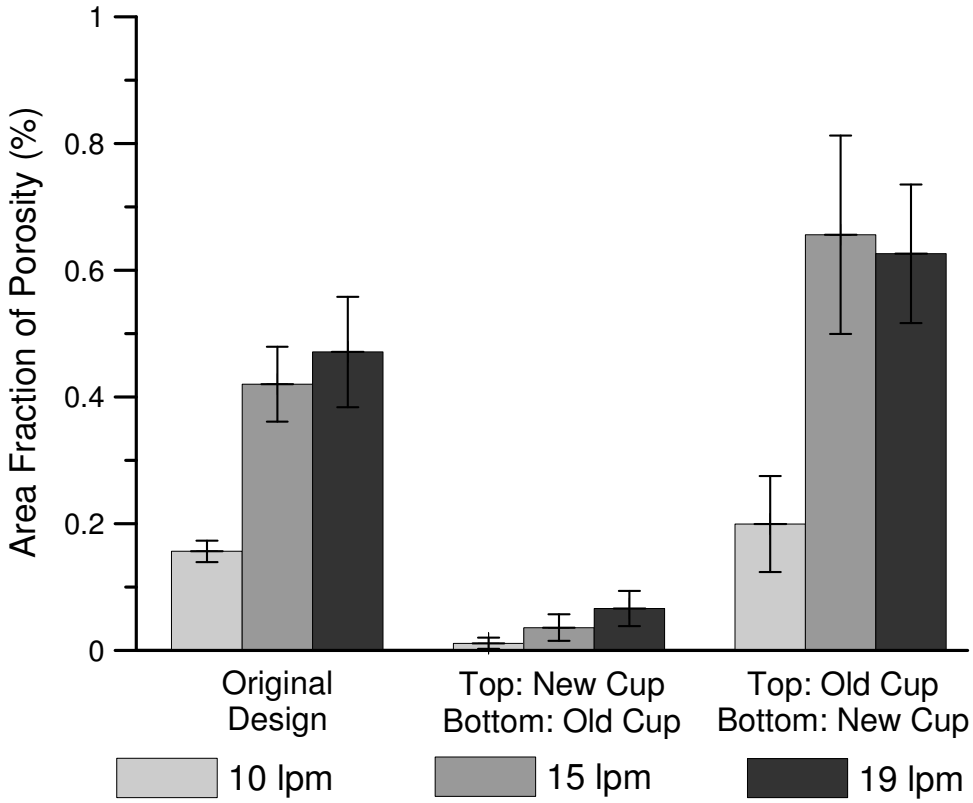

Figure 4.9: Area fraction of porosity (%) in welds produced using a 2 mm torch-to-workpiece distance versus shielding cup design and three different shielding gas flow rates.

A hypothesis test was performed to determine if there was any statistically significant difference in the mean area fraction of porosity in welds produced using the different shielding cups using 6 replicates for each welding condition. A t-test was used with a level of significance of 0.05, and assuming that the standard deviation of the two populations were unequal, to test the null hypothesis that the average area fraction of porosity in the welds produced using the original shielding cup and using the modified shielding cups was equal for each given shielding gas flow rate. The null hypothesis was rejected when comparing the mean area fraction of porosity in welds produced by the system with the modified shielding cup for the top Thermal Arc torch and the original system. In other words, the modified

shielding cup for the top Thermal Arc torch was found to significantly reduce the mean area fraction of porosity compared to the original system at each shielding gas flow rate. On the other hand, the null hypothesis was accepted when comparing the mean area fraction of porosity produced by the system with the modified shielding cup for the bottom B&B torch and the original system. In other words, when the shielding cup for the B&B torch was modified, there was no significant change in the mean area fraction of porosity at any shielding gas flow rate.

Based on this evidence, it is believed that the addition of a gas lens and the increased cross-sectional area of the shielding cup tip for the Thermal Arc torch increased the length of the laminar flow region and improved gas distribution. However, when the shielding cup for the B&B torch was modified, the shielding gas was less evenly distributed. Upon closer examination, the tapered section of the B&B torch's original shielding cup was observed to evenly distribute the shielding gas around the torch body. When this tapered section was removed, the shielding gas was no longer evenly distributed around the weld pool and some regions of the weld pool may have been exposed to contaminants in the room air.

Another series of hypothesis tests was also performed to determine whether the mean area porosity fraction was significantly different at different shielding gas flow rates. A t-test was used with a level of significance of 0.05 and assuming that the standard deviation of the two populations were unequal, to test the null hypothesis that the average area fraction of porosity in the welds produced at different shielding gas flow rates was equal. The null hypothesis was accepted when comparing the mean area fraction of porosity in welds produced by the system using the modified shielding cup with the top Thermal Arc torch, at a flow rate of 15 lpm vs. 19 lpm, 15 lpm vs. 10 lpm, and 10 lpm vs. 19 lpm. In other words, the mean area fraction of porosity was the same regardless of flow rate when the modified shielding cup was

used with the top Thermal Arc torch. The shielding gas flow rate was set at 10 lpm for future experiments since it was more economical to use less shielding gas.

4.2 Spot Welding with DSAW

Double-sided arc welding is a relatively new process which has only been applied towards the production of butt-joint configuration welds in thick plate of various alloys [38] - [43], and thin sheet [45], [46]. To date, the DSAW process has not been applied towards the production of lap-joint configuration welds. The feasibility of producing lap-joint configuration spot welds in thin aluminum sheet in the lap joint configuration using the DSAW process is examined in the following subsections.

4.2.1 Process Parameters and Suitable Welding Conditions

The main parameters involved in RSW are the electrode force, electrode shape, welding current, and welding time [50]. However, in the DSAW process, since neither torch comes into contact with the workpiece, the electrode force and shape are not relevant parameters, and the only important variables are the welding power and the weld time. In order to determine the range of welding conditions that would produce sufficiently large nuggets, a series of spot welds were produced in overlapping 1 mm thick AA5182 sheets using welding currents of 30 A, 50 A, and 70 A, and a weld time ranging from 1 second to 7 seconds. According to the AWS Welding handbook, RSW nuggets produced between 1 mm thick sheet must have a diameter of at least 4.06 mm [17]. Therefore, any DSA welds produced in this experiment which met this criterion and which fully penetrated through the thickness of the two sheets were considered to be “good” welds.

An example of a “good” weld that was produced using a 2.0 kW welding power and a 2 second weld time is shown in Figure 4.10. As seen in Figure 4.10a and Figure 4.10b, the nugget measures 7 mm in diameter, and both sides of the DSA weld nugget have been cathodically etched and exhibit a smooth bead profile. Evidence of the grain structure can be seen on the bottom weld bead surface in Figure 4.10b which shows a region of columnar grains starting from the fusion boundary and equiaxed grains in the centre of the welds. The transverse cross-sectional view of the weld, shown in Figure 4.10c, shows a crater crack at the centre of the nugget which is surrounded by solidification cracks and a through-thickness hole in the centre of the weld caused by solidification shrinkage. In addition, hydrogen gas porosity and oxide tails at the fusion boundaries with hydrogen pores attached are evident in the spot weld.

Figure 4.11 shows the measured DSAW weld nugget diameter versus weld time. In all cases, the weld nugget diameter increased with both welding power and welding time. At the lowest welding power of 1.2 kW, a weld time of three seconds was required to produce a nugget of an acceptable size between the two sheets. At a welding power of 1.9 kW, a weld time of one second was sufficient to produce a 6 mm diameter nugget in the workpiece. When the weld time was increased to seven seconds, a 16 mm diameter nugget was produced. Lastly, at a welding power of 2.8 kW, a one second weld time was capable of producing a 10 mm diameter nugget, and a weld time of three seconds was capable of producing a 14 mm diameter nugget. Additional welds were not made at this welding power since the nugget would have been too large for the DSAW table which had clamps spaced 20 mm apart.

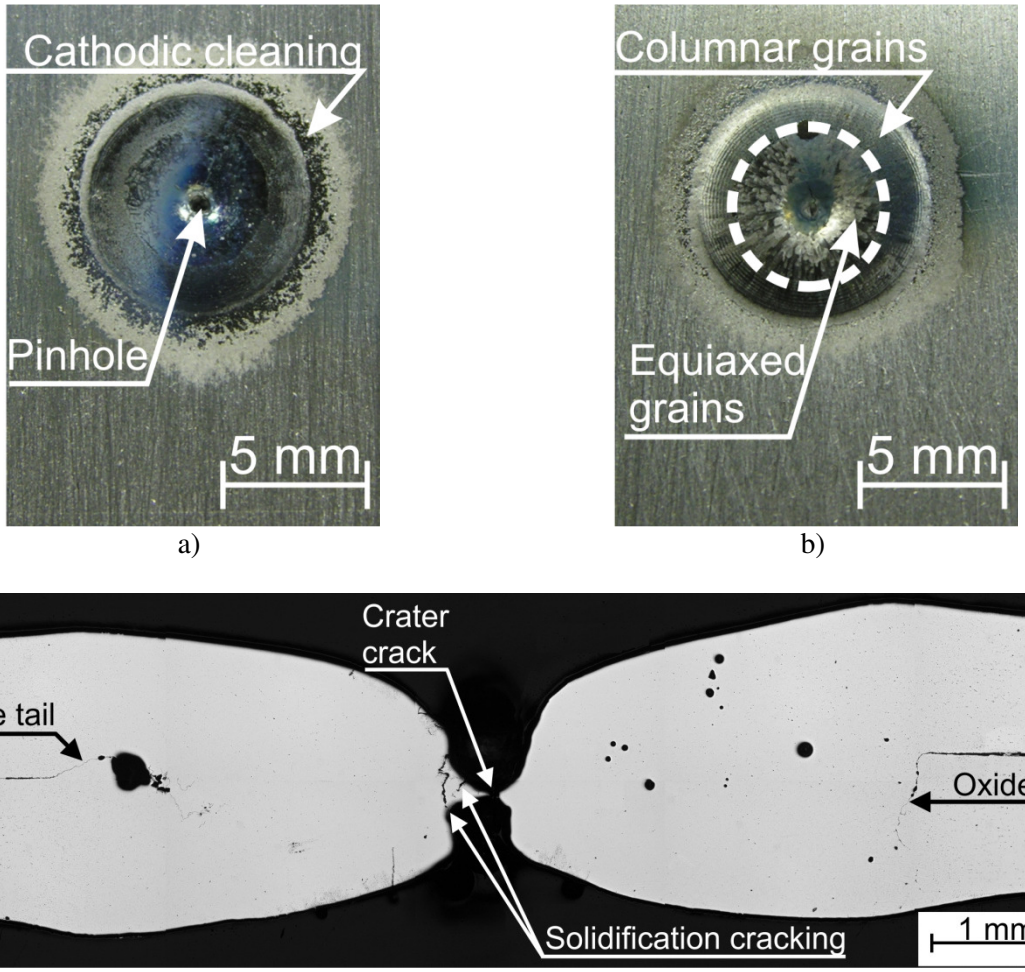

Figure 4.10: Photographs of a "good" weld produced using a 2.0 kW welding power and a weld time of 2 seconds showing: ***a)*** top view; ***b)*** bottom view; ***c)*** cross-sectional view.

The process map shown in Figure 4.12 shows the effect of welding power and welding time on nugget quality. The welding time required to make acceptable welds decreased with increasing welding power. Low weld times and powers produced undersized welds or welds with a lack of fusion whereas welds with acceptable diameters for the sheet thickness were produced using higher welding times or welding powers.

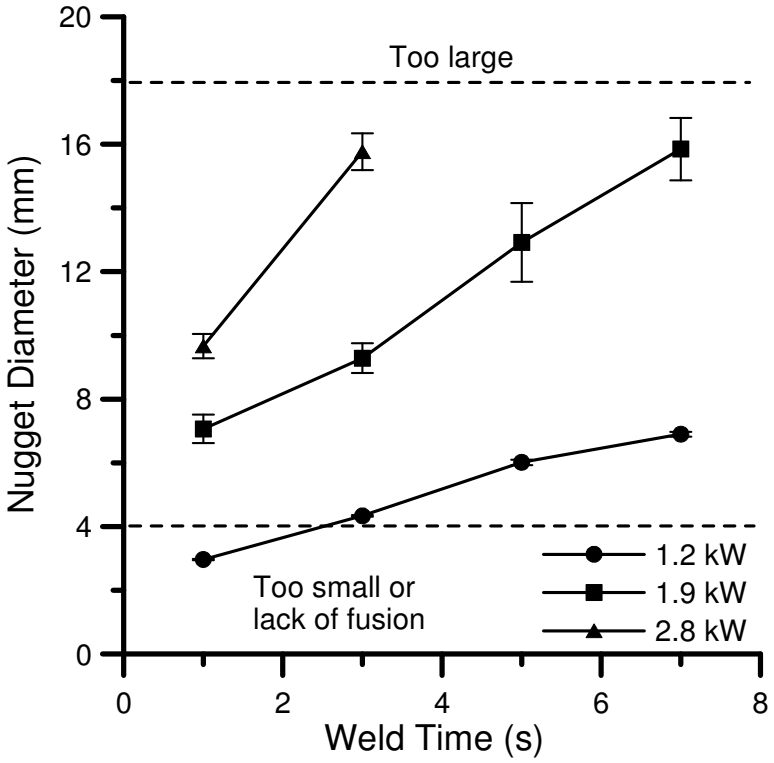

Figure 4.11: DSA spot weld nugget diameters (mm) versus weld time (s) for various welding powers (kW).

In a previous study of RSW in 1.5 thick AA5182 sheet, acceptable welds were produced with a welding current of 29 kA over a period of 42 cycles, or 0.67 seconds [25]. In comparison, the DSAW process was capable of producing spot welds in overlapping 1.0 mm thick AA5182 sheets using a welding current of at least 50A over a period of 60 cycles, or one second. Overall, it appears that the DSAW process is capable of producing full penetration spot welds of acceptable diameter in an amount of time which is comparable to the amount of time required by conventional RSW equipment, but at a small fraction of the welding current.

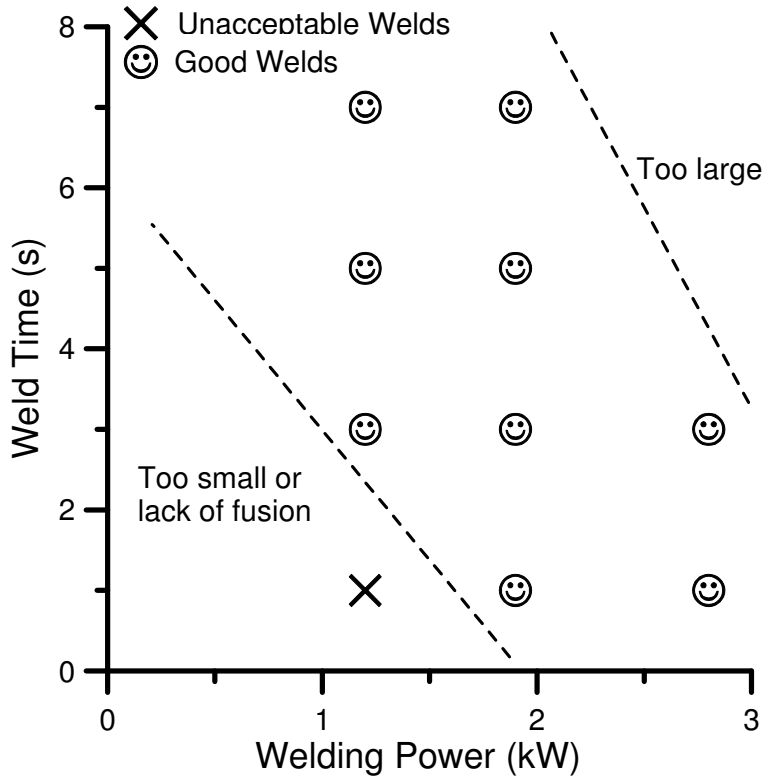

Figure 4.12: DSA spot weld process map.

4.2.2 Effects of Current Ramp Down

Crater cracks are commonly encountered during arc welding and a few techniques exist to prevent their formation. Adding extra filler metal to the end of the weld bead to provide the necessary fluid to fill in any shrinkage cavities and building up a convex bead profile which can better tolerate the transverse stresses caused by weld shrinkage is a commonly used technique for non-autogeneous welding processes [24]. For autogeneous processes, one method for eliminating crater cracks in arc welds is to gradually reduce, or ramp down, the welding current while the workpiece remains stationary. This reduces the cooling rate and the resulting strain rate acting on the solidified weld metal [24]. It was believed that ramping down the current could also lead to a decrease in gas porosity since the weld pool

would remain in the molten state for a longer period of time and allow more time for any dissolved gasses to bubble out of the weld pool. In order to determine the effectiveness of using the temporal pulse shaping technique, a series of spot welds was produced using a base welding current of 50 A, a hold time of 2 seconds, and a ramp down time of 0, 2, 4, and 10 seconds. Five welds were made at each welding condition.

As the ramp down time increased from 0 to 10 seconds, the weld nugget diameter also increased from 8 mm to 12 mm. Upon inspection of the DSA spot welds using a stereomicroscope, it was found that all of the spot welds made using the ramp down timer contained a pinhole at the centre of the nugget, regardless of the ramp down time. Spot welds produced with a ramp down time of 0 seconds, shown in Figure 4.13a, were found to exhibit the same type of pinhole and crater cracking defect as spot welds produced with a ramp down time of 10 seconds, shown in Figure 4.13b. Therefore, gradually ramping down the current did not appear to have any effect on the formation of crater cracks.

All DSA spot welds exhibited hydrogen gas porosity as shown for example in Figure 4.10. The area fraction of porosity was also observed to be largely unaffected by an increase in ramp down time. As seen in Figure 4.14, the specimens produced with a zero second ramp down time contained the lowest area fraction of porosity. Although the general trend appears to suggest that increasing the ramp down time generally increased the area fraction of porosity, a comparison of the means using a t-test with five replicates, a level of significance of 0.05, and assuming that the standard deviation of the two populations were unequal, revealed that the area fraction of porosity remained constant as the ramp down time increased from 2 to 10 seconds. A summary of the results from the hypothesis tests is given in Appendix B.

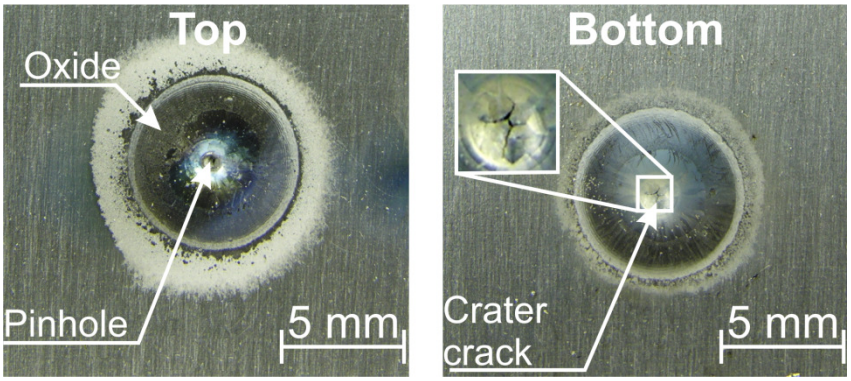

a)

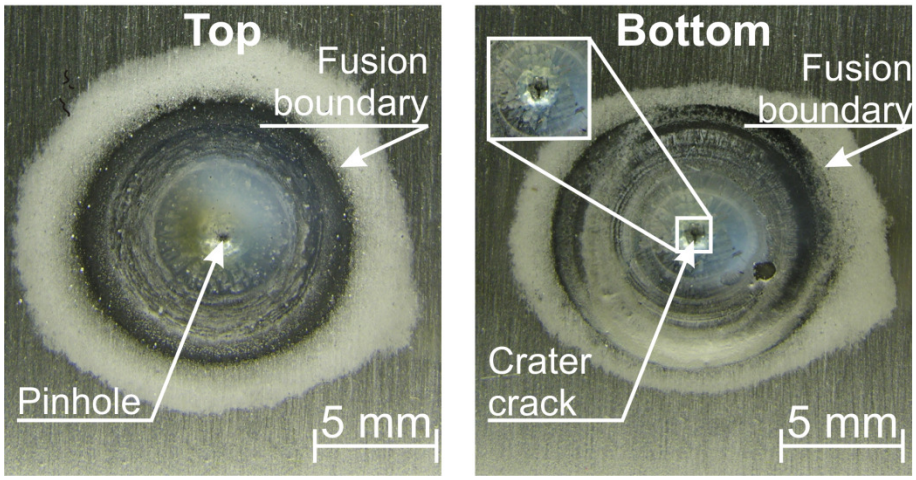

b)

Figure 4.13 Comparison of pinhole defects produced in welds with a welding power of 1.9 kW and a ramp down time of: ***a)*** zero seconds; ***b)*** ten seconds.

In a series of images captured using a Laser Strobe imaging system, shown in Figure 4.15, the outer edges of the weld pool appeared to be covered by an immobile oxide layer that would have prevented any hydrogen gas from escaping the weld pool. This increased oxide was evident on the outer regions of the weld pool shown in Figure 4.13. Since the molten, oxide-free weld pool reflects incident light, the dark, reflective surface corresponds to the exposed weld pool. On the other hand, the oxide film does not reflect light other than a diffuse reflection of the N_2 laser strobe light. The region surrounding the exposed weld pool corresponds to the region of the weld pool which is covered by the oxide layer. Although

increasing the ramp down time increased the amount of time that the weld pool remained in the molten state, the oxide layer covered a large area of the weld pool surface preventing any hydrogen gas bubbles that formed in the outer sections of the DSA weld nugget from escaping the weld pool.

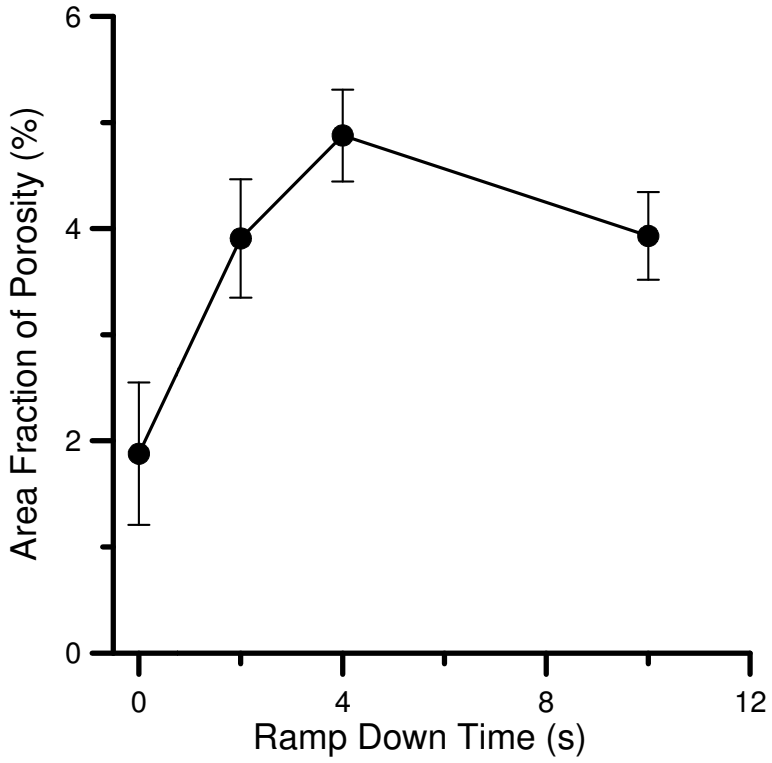

Figure 4.14: Area fraction of porosity versus ramp down time.

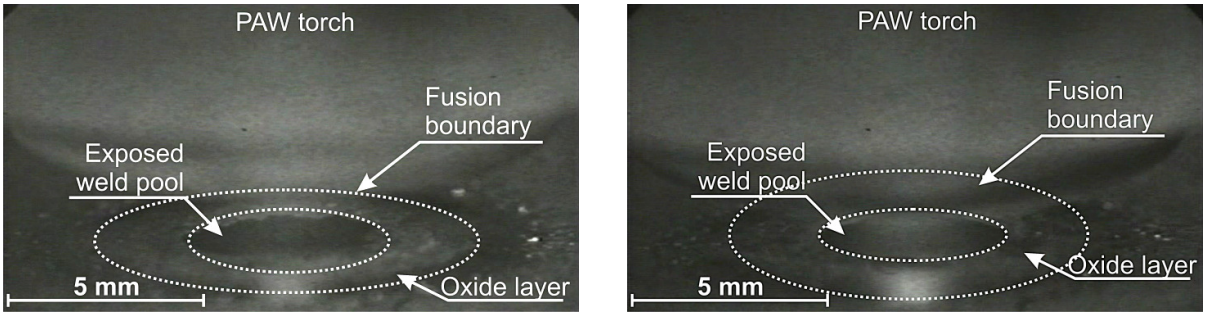

a) b)

Figure 4.15: Photographs of DSA spot welds taken using a Laser Strobe imaging system produced using a 2 kW welding power, 2 second weld time, and a ramp down time of: ***a)*** 2 seconds; ***b)*** 3 seconds

Although the incomplete cathodic etching of the oxide film on the top surface of the spot weld may explain why the amount of gas porosity did not decrease, it does not explain how the increase in ramp down time caused an increase in porosity. As shown in Figure 4.9, bead-on-plate welds produced in specimens that were degreased, deoxidized, and stainless steel wire brushed prior to welding were found to contain little to no porosity. Therefore, the formation of porosity in the DSA spot welds must be inherent to this particular application of the DSAW process.

4.2.3 Tensile-Shear Testing

Weld nuggets produced using a welding power of 1.9 kW and 2.8 kW, and with a weld time of 3 seconds and 1 second, respectively, were used to examine the strength and failure modes of the DSA spot welds. DSA spot welds produced using a 1.9 kW welding power had a nugget diameter of 6 mm, while nuggets produced using a 2.8 kW welding power had a nugget diameter of 10 mm. Load-displacement curves for these specimens are given in Figure 4.16. All of the welds failed in button pullout failure modes, which is the preferred mode of failure [76]. Figure 4.17 and Figure 4.18 illustrate the failure modes of welds produced using a 1.9 kW and 2.8 kW welding current, respectively. The larger nuggets produced using a 2.8 kW welding power failed at a higher load than the smaller nuggets produced using a 1.9 kW welding power. On average, welds produced with a 1.9 kW welding power sustained a maximum force of 1.96 ± 0.105 kN before fracturing, while nuggets produced using a welding power of 2.8 kW sustained an average maximum load of 2.36 ± 0.226 kN. All of the welds produced during this study exhibited a ductile fracture surface, and none of the fractures were observed to initiate at the pinhole which exists at the centre of each nugget. The AWS D8-7 “Recommended Practices for Automotive Weld Quality – Resistance Spot Welding” standard stipulates that the average pulled button diameter for welds produced in 1 mm thick sheet must be no less than 4.3 mm [77]. The average pulled button

diameter for nuggets produced with a welding power of 1.9 kW was found to be 6.36 ± 0.83 mm, and 7.03 ± 0.75 mm for nuggets produced using a welding power of 2.8 kW. Therefore, these nuggets would be classified as acceptable spot welds based on this measurement.

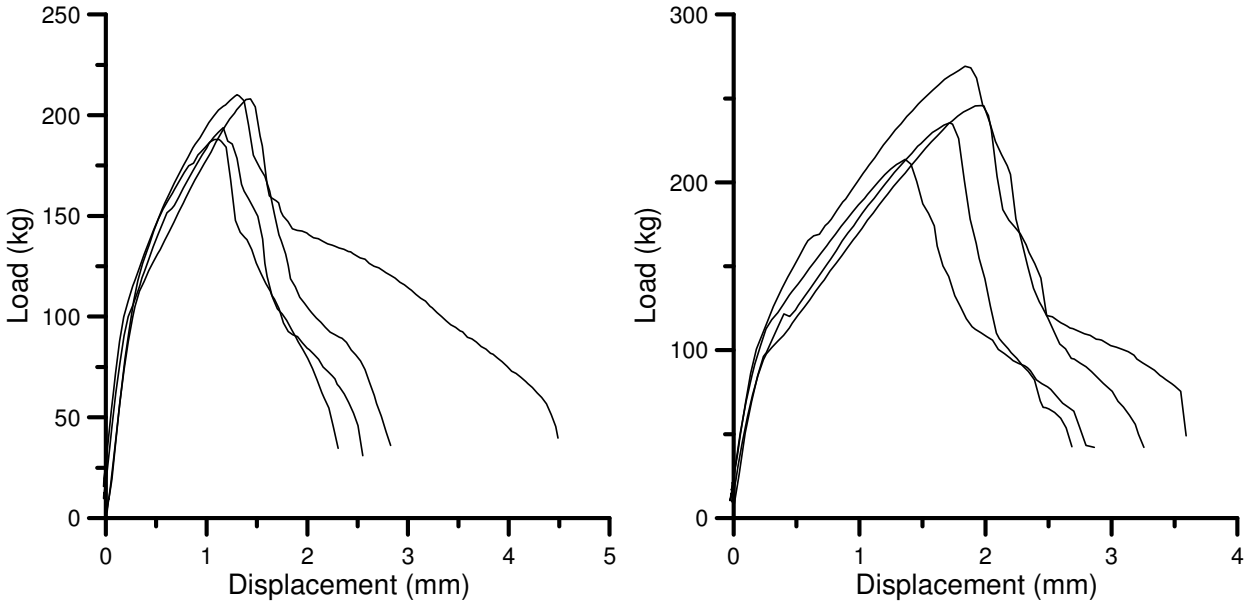

Figure 4.16: Load versus displacement curves for DSA spot weld nuggets produced using: ***a)*** 1.9 kW welding power and 3 second weld time; ***b)*** 2.8 kW welding power and 1 second weld time.

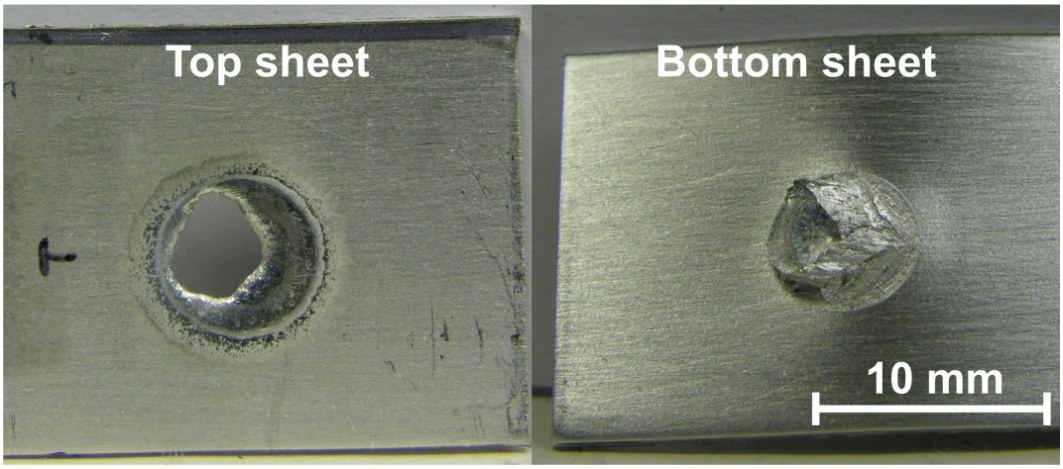

Figure 4.17: Button pullout mode fracture in a DSA spot weld nugget produced with a 1.9 kW welding power and 3 second weld time.

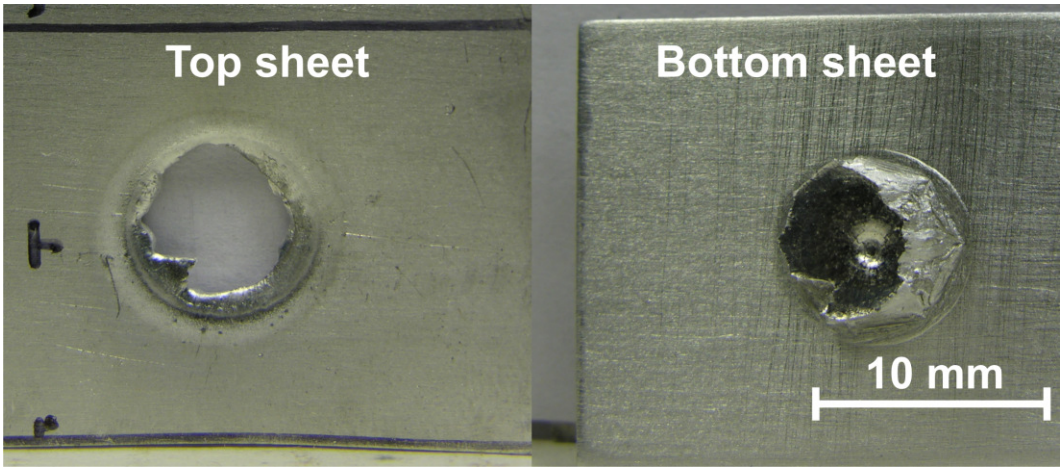

Figure 4.18: Button pullout mode fracture in a DSA spot weld nugget produced with a 2.8 kW welding power and 1 second weld time.

4.2.4 Weld Nugget Solidification

Since the previous experiments showed that crater cracking and the through-thickness hole at the centre of the DSA spot welds could not be prevented by altering the process parameters, it was believed that the defect was inherent to the solidification behaviour of the spot welds. In order to better understand this solidification behaviour, a Laser Strobe video imaging system was used to record the formation and solidification of a DSA spot weld. A series of spot welds were produced using a welding current of 50 A with a hold time of 2 seconds, and a ramp down time ranging from 1 to 4 seconds to identify any trends associated with the solidification behaviour of the weld.

The sequence of images in Figure 4.19 shows the solidification sequence of a spot weld. Figure 4.19a shows the initiation of the arc, which is the area indicated by the bright region of light. Once a stable arc is established, a weld pool starts to form, as shown in Figure 4.19b. Evidence of cathodic etching of the surrounding oxide may also be seen. The weld pool has a dark, glassy appearance because the clean molten metal surface readily reflects the incident light away from the camera. The nugget continues to grow in size as more energy is inputted into the workpiece until it reaches its maximum diameter, as shown in Figure 4.19c. After a period of 2 seconds, the arc current is gradually ramped down and the brightness of the arc is reduced, as seen in Figure 4.19d. Figure 4.19e shows the state of the weld pool at the instant that the arc is shut off. After the weld cycle is completed, the arc is turned off and the outer regions of the weld pool start to solidify. Figure 4.19f shows the solidified weld pool with its characteristic concave appearance. The dark region at the centre of the weld nugget is the concave region around the pinhole which was not illuminated by the laser due to its shape.

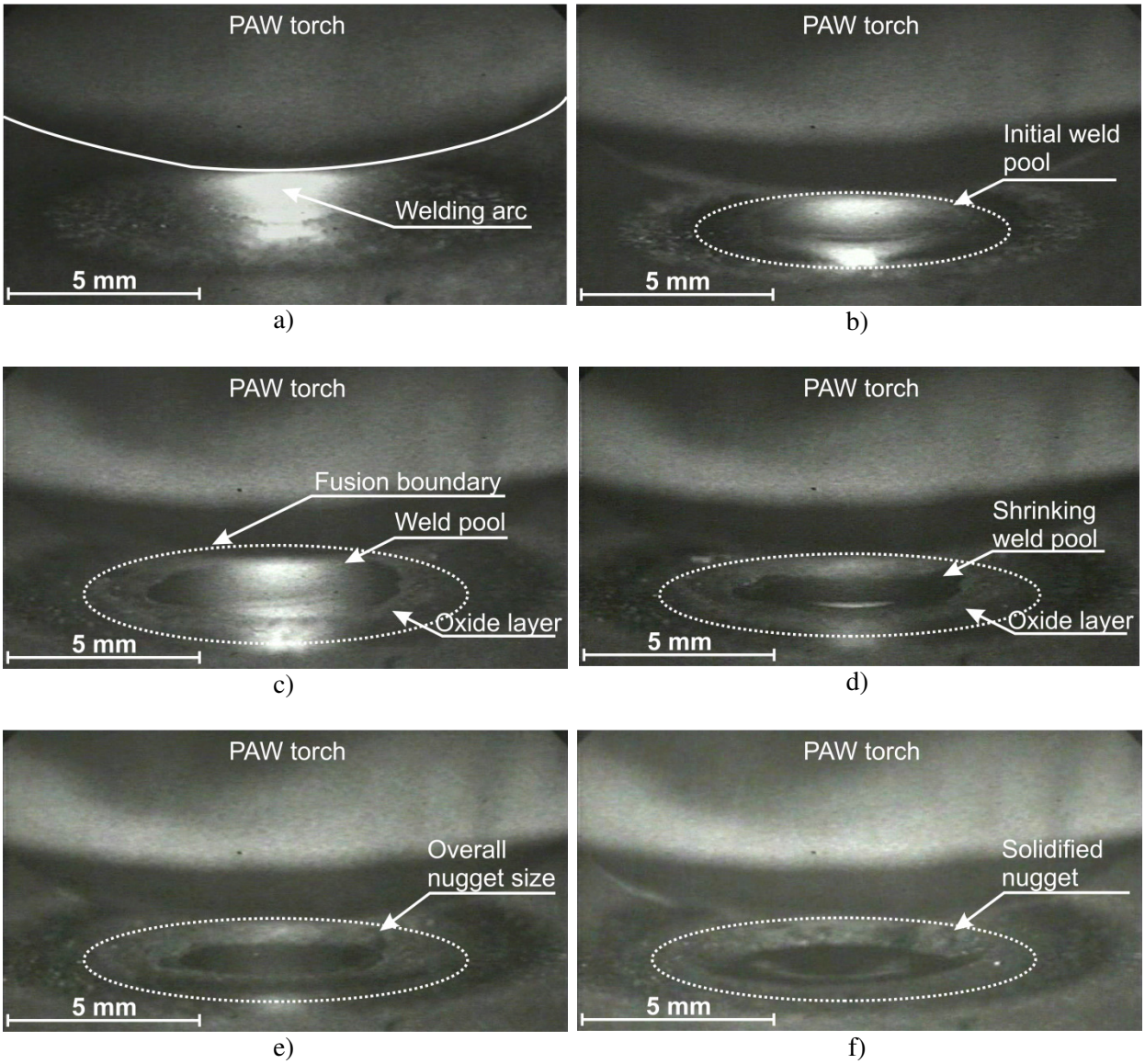

Figure 4.19: Solidification sequence of a DSA spot weld taken using a Laser Strobe imaging system showing: ***a)*** arc initiation; ***b)*** weld pool formation and growth; ***c)*** maximum weld pool size; ***d)*** decrease in welding current and weld pool size; ***e)*** weld pool after arc shutoff; ***f)*** solidified weld pool.

Schematic diagrams are shown in Figure 4.20 that show a transverse cross sectional view and a top view of the solidification sequence of a DSA spot weld. As shown in Figure 4.20a, the total volume of the molten metal in the weld pool is greater than that of the original solid due to the thermal expansion of

the solid, the increase in specific volume as the solid transforms to liquid, and the thermal expansion of the superheated liquid. While the weld pool is still completely in the molten state, the Gaussian-distributed arc pressure creates a dimple at the centre of the weld pool, and the displaced molten metal is pushed outwards to the edge of the weld pool as shown in Figure 4.20a. Once the arc is extinguished, the weld nugget begins to solidify starting from the outside. This initial solidification stage leaves evidence of the initial raised contour, and causes a transfer of material from the inside of the nugget to the outside, as shown in Figure 4.20b. As the molten weld metal cools and solidifies, there is a drop in the specific volume of the metal as the atoms rearrange themselves from a relatively open, amorphous liquid structure, into a more tightly packed crystal structure. As the weld pool shrinks in size, cavities are formed in the newly solidified metal which must be filled in with fresh molten metal to prevent the formation of shrinkage porosity. In moving welds, the advancing weld pool provides a continuous supply of fresh molten metal to the solidifying weld pool. However, this is not possible in stationary spot welds. As the weld nugget solidifies, it begins to take on a concave shape which is susceptible to crater cracking because the reduced cross section cannot tolerate the tensile thermal stresses produced by weld metal contraction on cooling [24]. As the weld nugget further solidifies, a disproportionate amount of liquid has solidified in the expanded outer ring, thereby leaving an insufficient amount of liquid to fill in the centre, as shown in Figure 4.20c. As a result, a pinhole and a crater crack form at the centre of the nugget once the remaining liquid is exhausted, as shown in Figure 4.20d, and Figure 4.10d.

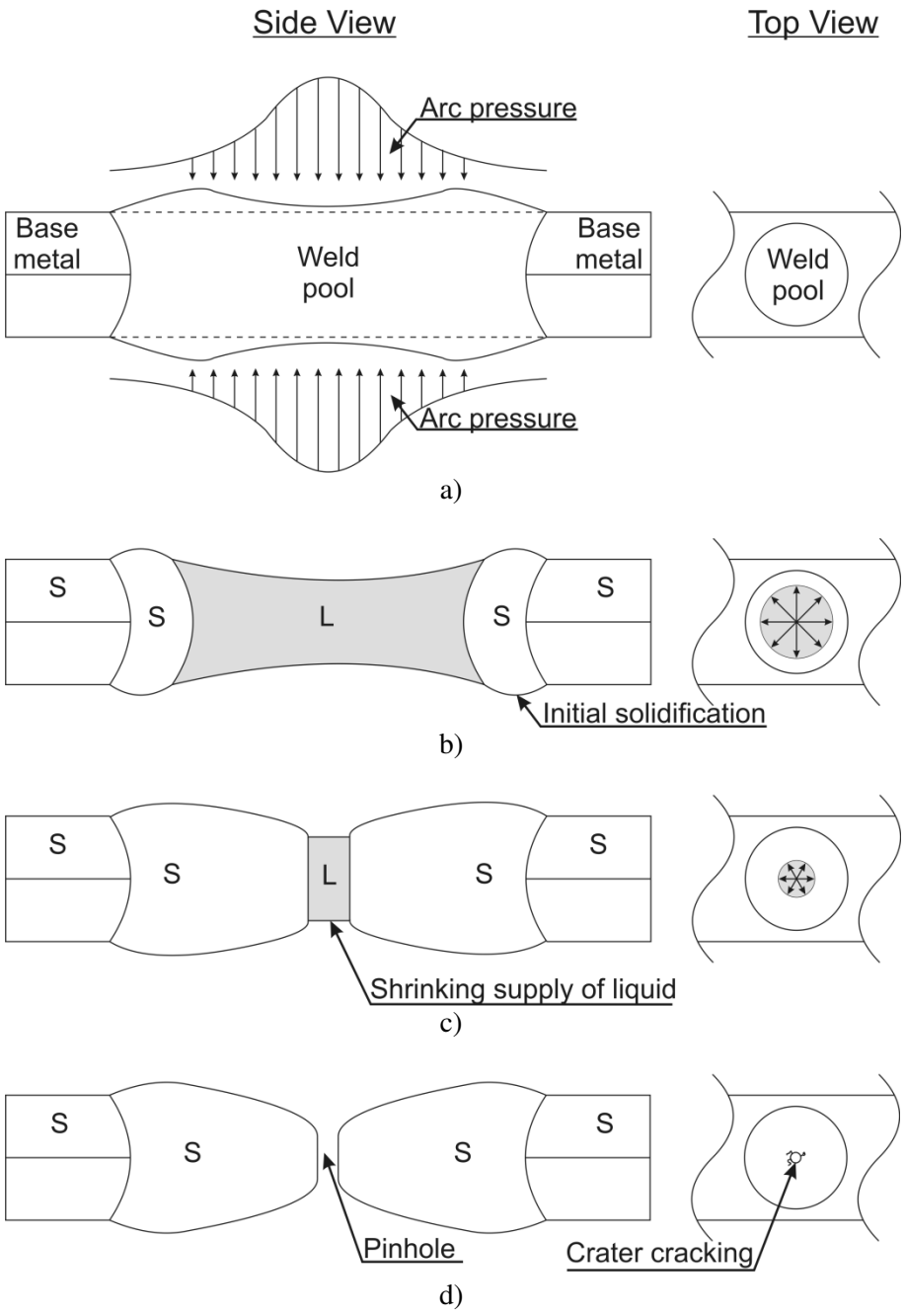

Figure 4.20: Schematic diagram of the solidification sequence of DSA spot welds showing: ***a)*** molten weld pool; ***b)*** initial solidification with raised contour near the fusion zone boundary; ***c)*** nearly complete solidification and a shrinking supply of molten metal at the centre of the nugget; ***d)*** completely solidified weld pool with a pinhole and crater cracking.

Overall, while the non-contact DSA spot welding process can be used to produce spot welds at a small fraction of the welding current required to produce resistance spot welds in the same material, the welds exhibit a number of defects which reduce their strength and quality. The presence of oxide tails at the fusion zone boundary and hydrogen gas porosity is detrimental to the mechanical properties of the DSA spot welds. In addition, the formation of crater cracks and solidification shrinkage at the centre of each weld is inevitable since the volume of metal that shrinks upon solidification cannot be filled in by a fresh supply of molten metal.

4.3 Lap-Joint Configuration Seam Welds

Since there is no current literature on conduction-mode DSAW seam welding of aluminum sheet in the lap-joint configuration, a series of experiments was performed on overlapping 1 mm thick AA5182 sheet to determine the optimal range of welding conditions. The mechanical properties of the welds were analyzed using micro-hardness and tensile tests. The microstructure of the weld was examined using metallographic analysis.

4.3.1 Range of Suitable Welding Conditions

Photographs of the top weld bead and bottom weld bead produced using a total welding power of 3 kW and at welding speeds between 15 mm/s and 40 mm/s are shown in Figure 4.21 and Figure 4.22, respectively. At low welding speeds, excessive heat input produced centreline cracking in the weld bead, as shown in Figure 4.21a and Figure 4.22a. Higher welding speeds resulted in smooth weld beads with excellent cathodic cleaning, and the weld width was observed to decrease with increasing welding speed.

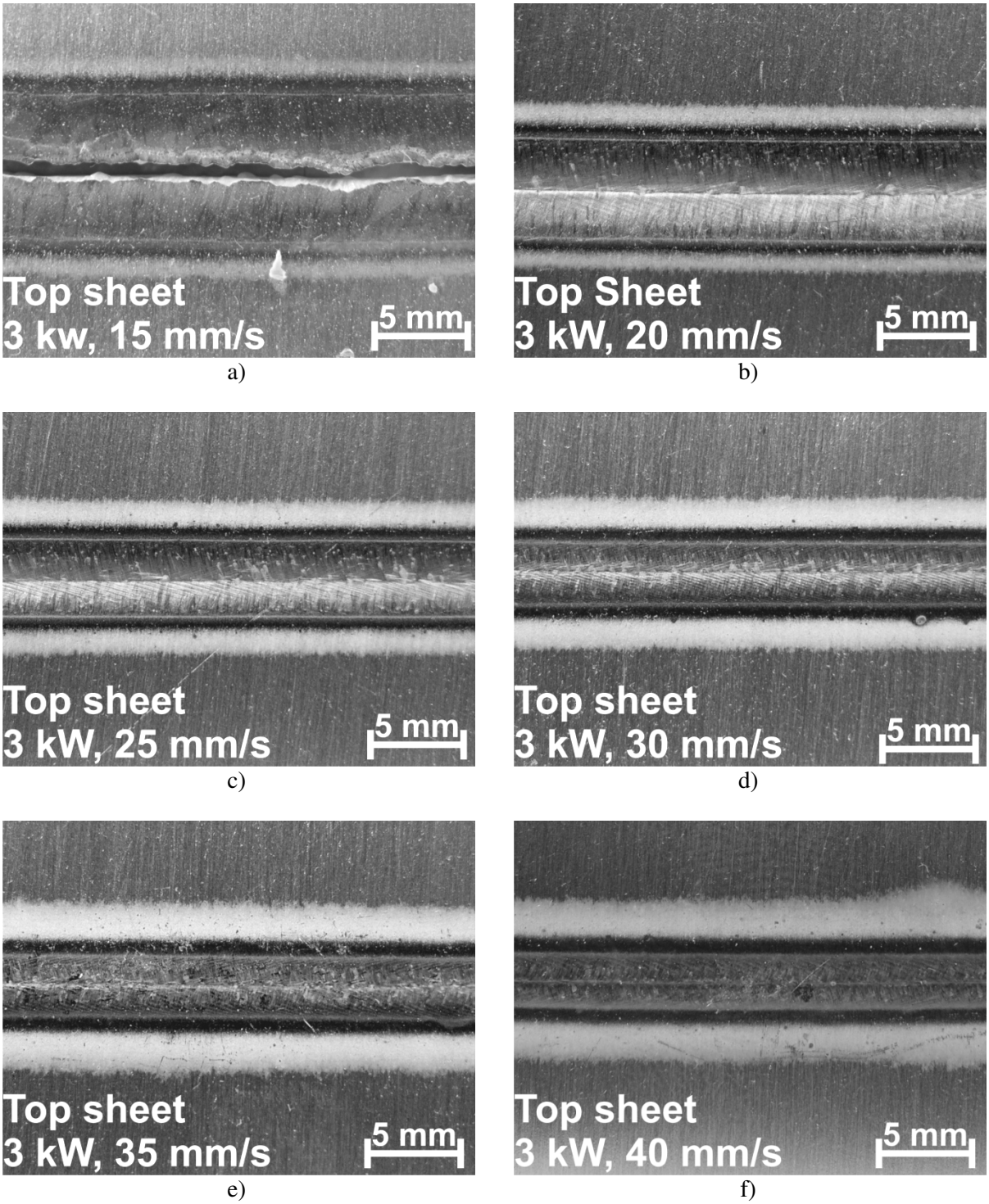

Figure 4.21: Photographs showing top weld bead appearance of lap-joint configuration DSA welds.

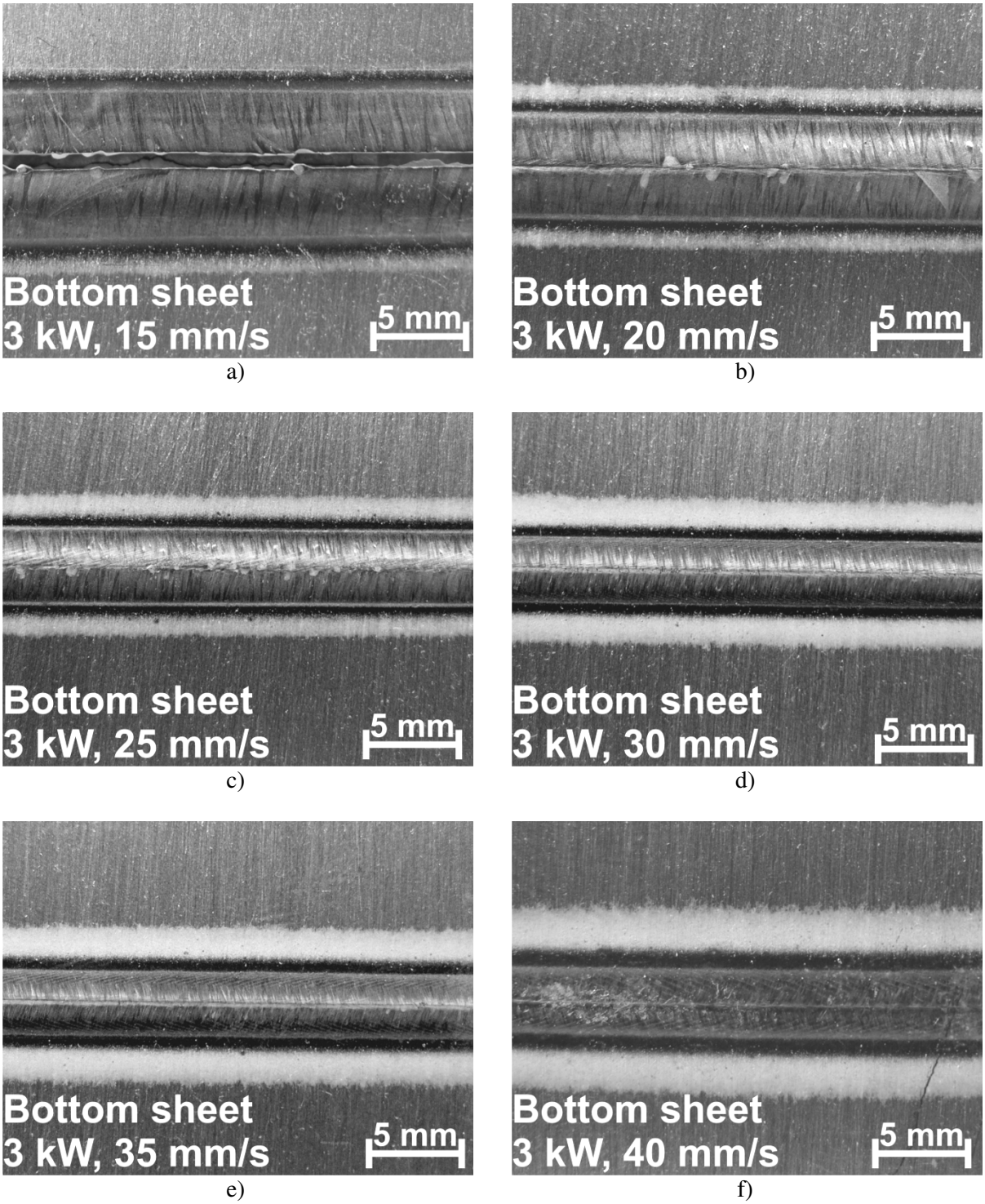

Figure 4.22: Photographs showing bottom weld bead appearance of lap-joint configuration DSA welds.

The weld bead exhibited a beneficial columnar-equiaxed grain transition, as shown in Figure 4.23, which is known to reduce the risk of solidification cracking and improve mechanical properties [44], [50]. This grain structure was also observed by Kwon and Weckman [45] and Moulton and Weckman [46] in their studies of DSAW of aluminum sheet.

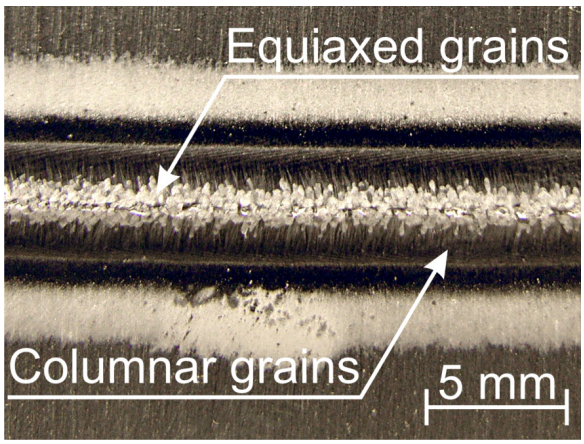

Figure 4.23: Photograph of a bottom weld bead produced at a total welding power of 4 kW and a welding speed of 40 mm/s.

Figure 4.24 shows a series of transverse cross sections of welds produced at a welding power of 2 kW and welding speeds of 10, 15, and 20 mm/s. The weld pool in each case exhibits a symmetrical, hourglass profile. Comparing Figure 4.24a and b, higher welding speeds produced a more pronounced hourglass profile and a narrower weld bead. As the welding speed was increased further, there was insufficient heat to melt through the entire thickness of the sheet and a partial penetration weld was produced as shown in Figure 4.24c. This weld would be classified as an unacceptable weld because there was no fusion between the two sheets. All of the welds show minimal angular thermal distortion as a result of the symmetry of the DSA welding process. In addition, there was minimal sag or drop-through since the surface tension forces in the molten weld pool were strong enough to counteract the force of

gravity. In many cases, there was evidence of hydrogen gas porosity in the welds and an entrained oxide film extending from the interface between the two sheets at the edge of the weld pool.

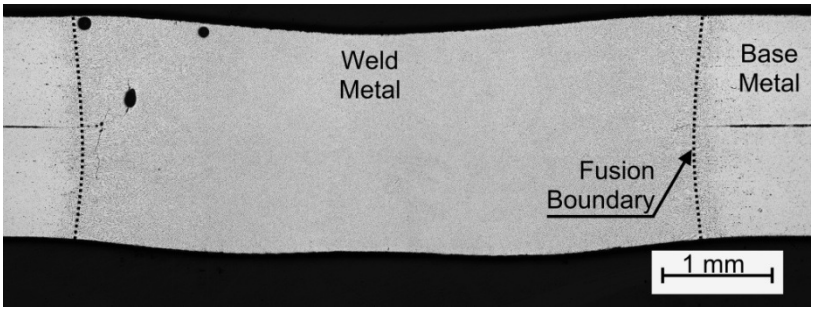

a)

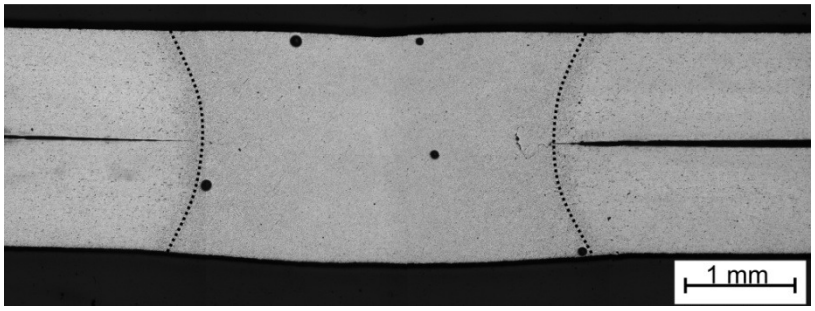

b)

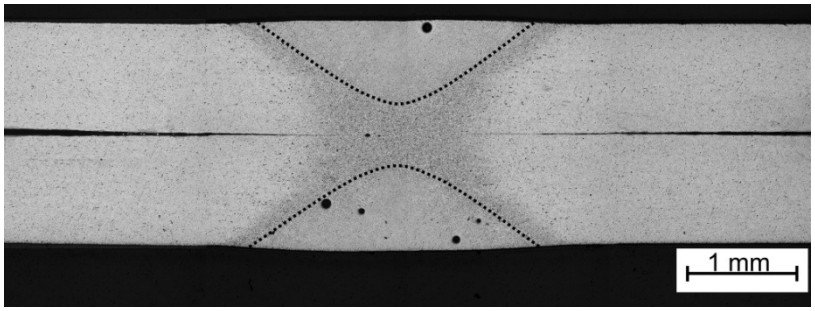

c)

Figure 4.24: Transverse cross sections of welds produced at a total welding power of 2 kW and welding speeds of: ***a)*** 10 mm/s; ***b)*** 15 mm/s; ***c)*** 20 mm/s.

A series of welds were produced using welding powers of 2 kW, 3 kW, 4 kW, and 5.1 kW, and a range of welding speeds from 5 mm/s to 75 mm/s, in increments of 5 mm/s, to generate a process map. Additional welds were not produced at welding powers greater than 5.1 kW since the welding voltage

was observed to exceed the ±44 V capability of the power supply which would cause the power supply to shut down. The range of welding conditions which produced visually acceptable, full penetration welds is shown in Figure 4.25. Blowholes and centerline cracking were seen in welds produced with excessive heat input. Insufficient heat inputs produced superficial welds without any fusion between the sheets. In general, the welding speed that could be used to make visually acceptable welds increased with welding power. Also, as the speed was increased for a fixed welding power, the width of the weld bead decreased due to the decreasing heat input per unit distance. The maximum welding speed which produced visually acceptable, full penetration welds was found to be 70 mm/s at a total welding power of 5.1 kW. All welds were found to exhibit excellent cathodic cleaning on both sides of the weld bead.

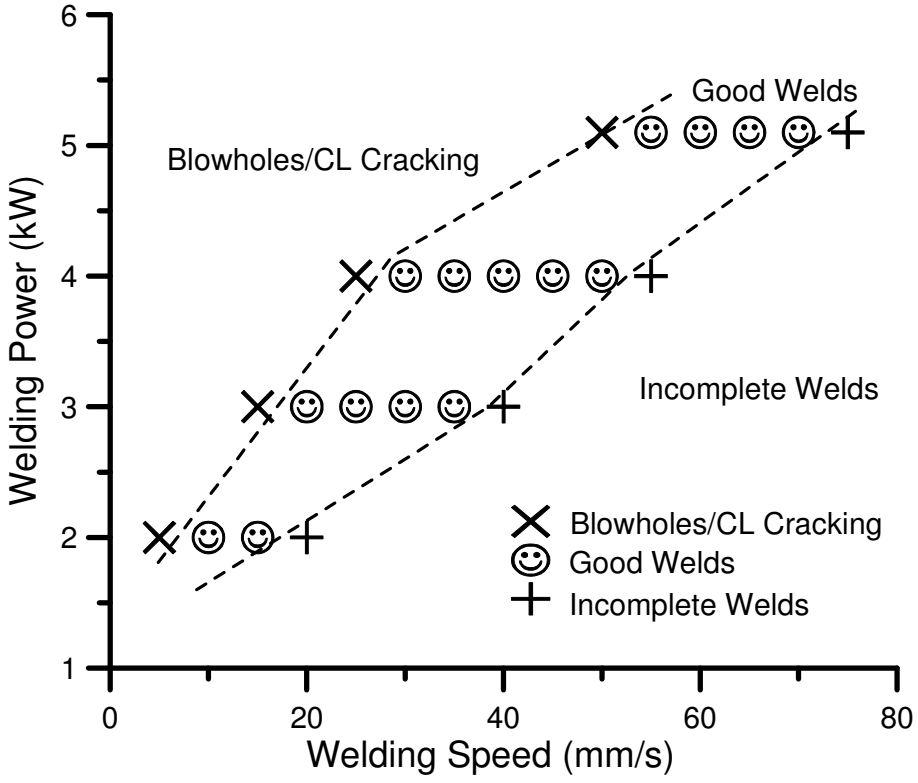

Figure 4.25: Range of visually acceptable welding conditions for producing lap-joint configuration seam welds.

4.3.2 Oxide Tail Defects

Oxide tails were previously encountered by Howard *et al*. [53] when producing lap-fillet welds made in AA5182 using a diode laser. In their study, these oxide tails were attributed to undisturbed coherent oxides on the surface of the aluminum sheet that were left in place because the fluid flow in the conduction-mode diode laser weld pool was too quiescent to disrupt the films during welding. These entrained oxides were found to reduce the weld throat and the resulting joint strength. Oxide tails are also frequently encountered in castings, and are known as bifilm defects [59]. The bifilm defect is produced in aluminum and other metal castings when an oxide film folds back onto itself due to surface turbulence, contraction of a liquid surface, or the separation and rejoining of a metal stream. The resulting ceramic-ceramic interface is unbonded and can appear as a small crack as shown in the Figure 4.26a. In the presence of a hydrogen rich environment, the bifilm acts as an excellent nucleation site for hydrogen gas porosity as shown in Figure 4.26b. The schematic diagram can be compared against Figure 4.27, which shows a typical example of an oxide tail which extend into the weld metal and provide a nucleation point for hydrogen gas pores in the region near the fusion zone boundary in a DSA seam weld produced using a 2 kW welding power and a 10 mm/s welding speed.

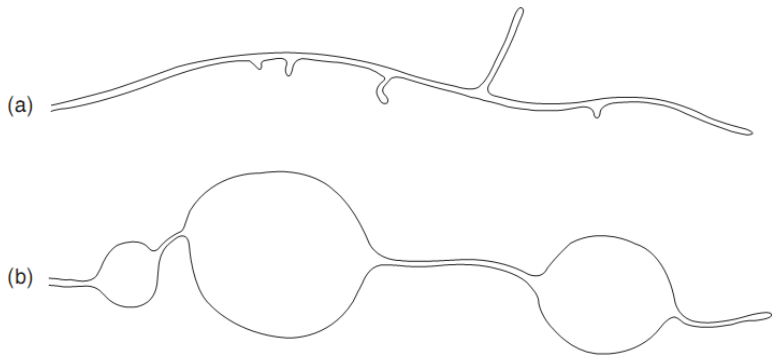

Figure 4.26: Schematic diagram of common bifilm defects showing: ***a)*** a newly formed bifilm; ***b)*** gas porosity trapped in a bifilm (taken from Castings 2nd ed by J. Campbell [59]).

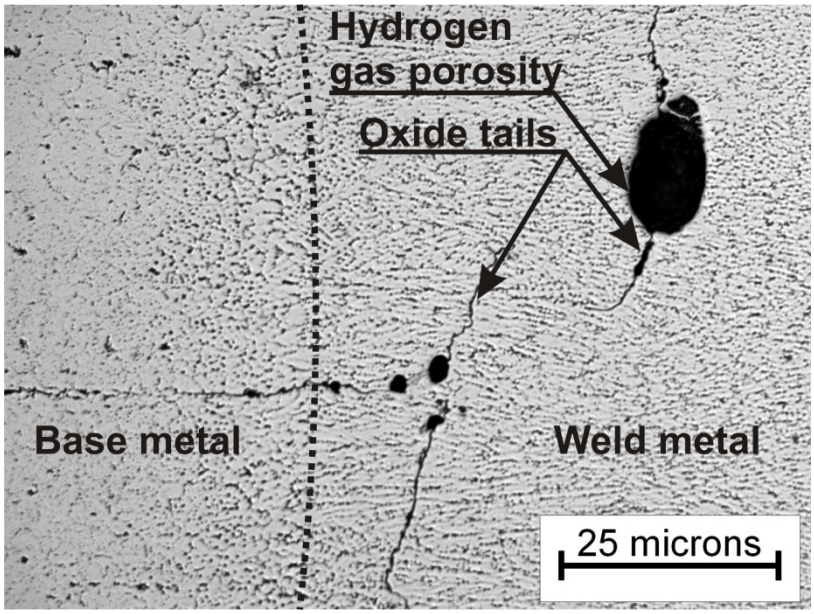

Figure 4.27: Photograph of oxide tails at the fusion boundary in a DSA seam weld produced using a 2 kW welding power and 10 mm/s welding speed.

In the case of lap-joint configuration aluminum welding, an oxide-oxide interface is formed when the two sheets to be welded are clamped together. Since the oxide has a melting temperature of 2072°C [78], it is very difficult to eliminate the oxide tails once they have formed. Howard *et al.* [53] found that removing the thick oxide layer prior to welding reduced the length of the oxide tails in diode laser lap-fillet welds of AA5182 sheet.

To determine whether the thickness of the pre-existing oxide layer played a role in the formation of oxide tails during DSAW of aluminum sheet, a series of lap-joint configuration welds were produced using five different cleaning techniques, which are summarized in Table 4.3. Welds were produced using a total welding power of 2 kW and a welding speed of 10 mm/s, since these welding conditions had been shown to produce good quality welds with minimal porosity in a previous experiment.

Table 4.3: Summary of cleaning techniques used to determine effect of specimen cleaning on oxide tail length.

Test #	1	2	3	4	5
Cleaning Procedure	• as received	• degreased with acetone • degreased with methanol	• stainless steel wire brushed	• degreased with acetone • degreased with methanol • stainless steel wire brushed	• degreased with acetone • degreased with methanol • immersed in NaOH for 2 min. @ 70° C • immersed in HNO_3 for 1 min. • stainless steel wire brushed

The effectiveness of the different cleaning techniques was determined by measuring the total length of the oxide tails in six cross-sections from each specimen. The results of the experiment are shown in Figure 4.28. The specimens that were welded in the degreased and as-received condition had a very thick oxide layer which was not completely melted. As a result, these two specimens had very long oxide tails and very little fusion between the two sheets. Stainless steel wire brushing resulted in a significant decrease in the oxide tail length. Degreasing and wire brushing the specimens prior to welding further reduced the oxide tail length. Finally, using the full cleaning procedure consistently produced short oxide tails. Based on these results, it is believed that eliminating the thick oxide layer prior to welding is necessary in order to produce welds with fewer oxide tails. In addition, degreasing the specimens is also important since hydrogen gas porosity often nucleates on the oxide tails and can also expand any entrained oxides. As shown in Figure 4.29, the average area fraction of porosity was also found to decrease with increasing specimen cleanliness.

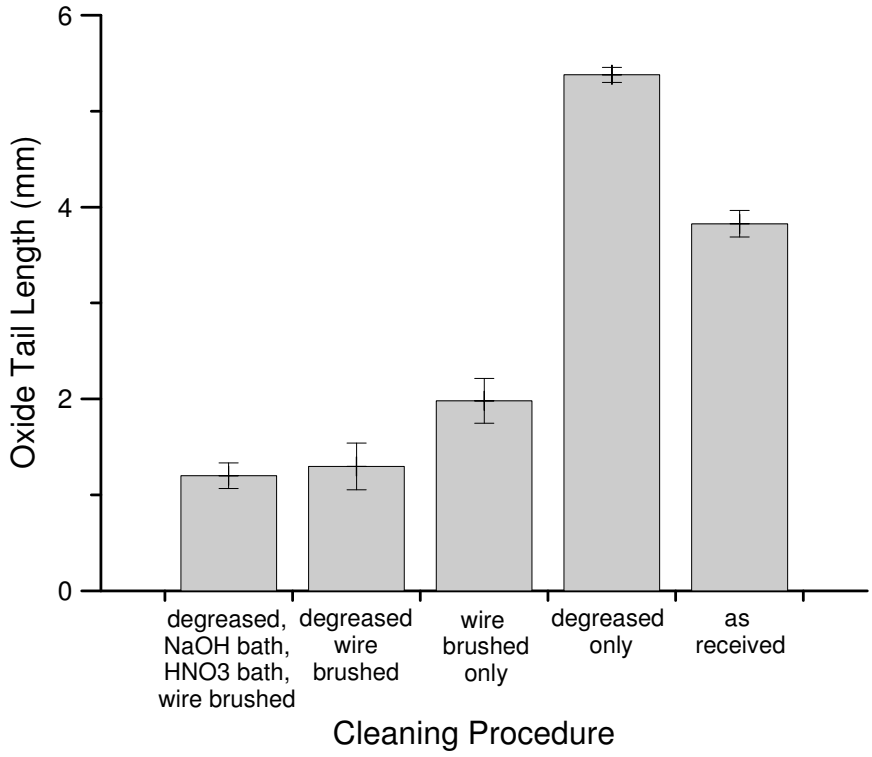

Figure 4.28: Relationship between specimen precleaning and oxide tail length.

The AWS D8.14M/D8.14:2000 Specification for Automotive and Light Truck Components Weld Quality – Arc Welding states that "the total length of imperfections in any cross section should not exceed 0.2 times the metal thickness" [70]. For 1 mm thick sheet, the oxide tails in the welds should be no more than 0.2 mm in length for the welds to meet the quality requirements specified by the AWS. Many of the seam welds contained oxide tails that exceeded 0.2 mm in length, regardless of welding power or welding speed.

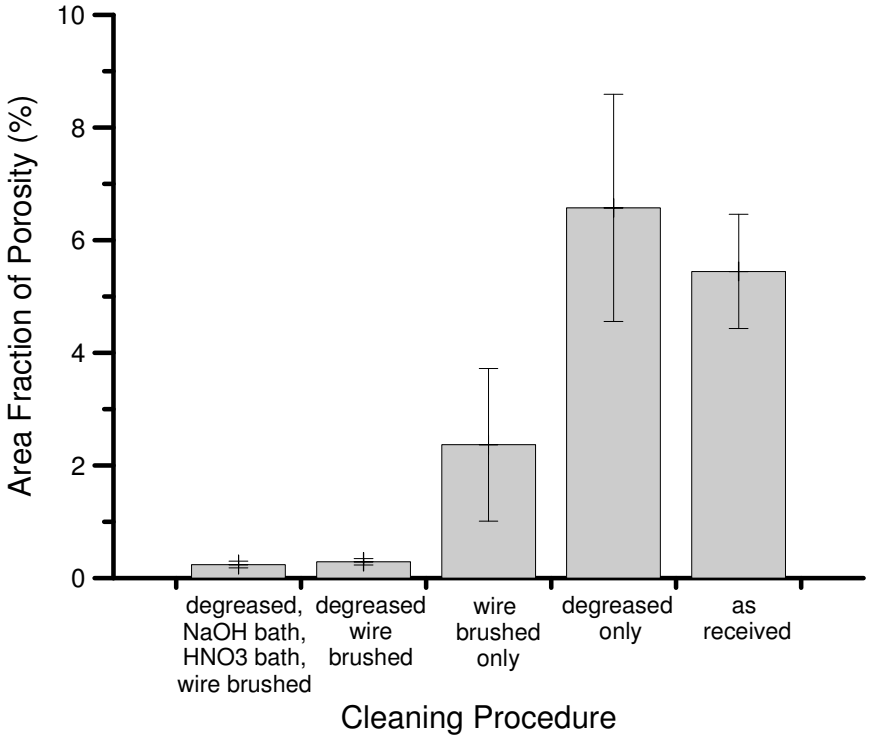

Figure 4.29: Area fraction of porosity in DSA seam welds produced using difference specimen precleaning techniques.

4.3.3 MathCAD Simulation Results

Kwon and Weckman [45], [79] demonstrated that an analytical thermal model of the DSAW process could be used to predict the size and shape of conduction mode bead-on-plate DSA welds in thin AA5182 sheet. This model was solved using MathCAD 14 software to determine whether the analytical thermal model could be used to predict the size and shape of conduction-mode lap-joint configuration DSA seam welds. All calculations were based on a sheet thickness of 2 mm and with infinite length in the x and y directions. A summary of the constant thermophysical material properties is given in Table 4.4 An arc width ranging from 0.00145 m to 0.00165 m and an arc efficiency ranging from 0.325 to 0.38 was used, depending on welding power and welding speed.

Table 4.4: Summary of constant thermophysical material properties for the AA5182-O alloy.

T_s (K)	T_{mp} (K)	T_{room} (K)	K_t (W/mK)	C_P J/KgK	ρ (Mg/m^3)
850	906	295	123	904	2.65

Figure 4.30 compares the weld width for the top and bottom weld beads predicted by the analytical thermal model with the measured values. As the welding speed was increased, the arc efficiency was also increased in the analytical thermal model to account for the reduction in heat loss to the welding table. Kwon and Weckman [80] also noticed a similar trend in their study of analytical thermal modelling of conduction-mode DSAW. Increasing the welding speed was also found to reduce the weld width, and partial penetration welds were produced at sufficiently high speeds.

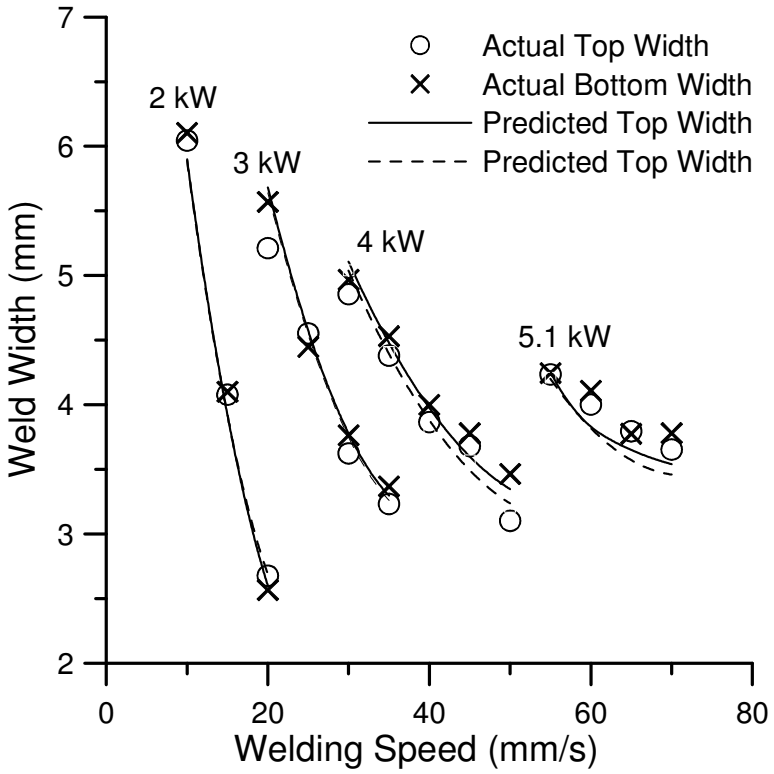

Figure 4.30: Measured and predicted weld width for lap-joint configuration DSA seam welds produced in 1 mm thick AA5182-O sheets using a 2 kW welding power.

Overall, there was excellent correlation between the predicted and measured values. The arc efficiencies and arc distribution coefficients used for each welding condition are given in Appendix C.

4.3.4 Mechanical Properties

Since the AA5182-O aluminum alloy had been annealed and recrystallized prior to welding, it was expected that the hardness would be consistent across the base metal and weld metal. Indeed, previous studies by Kwon and Weckman [45] and Moulton and Weckman [46] found that the hardness across the weld metal was approximately equal to the hardness across the base metal and heat-affected zone (HAZ). Figure 4.31 shows a microhardness profile of a weld that was produced using a total welding power of 2 kW and a welding speed of 15 mm/s. As expected, the microhardness across the base metal was very similar to the microhardness across the weld. In addition, there did not appear to be any softening in the HAZ.

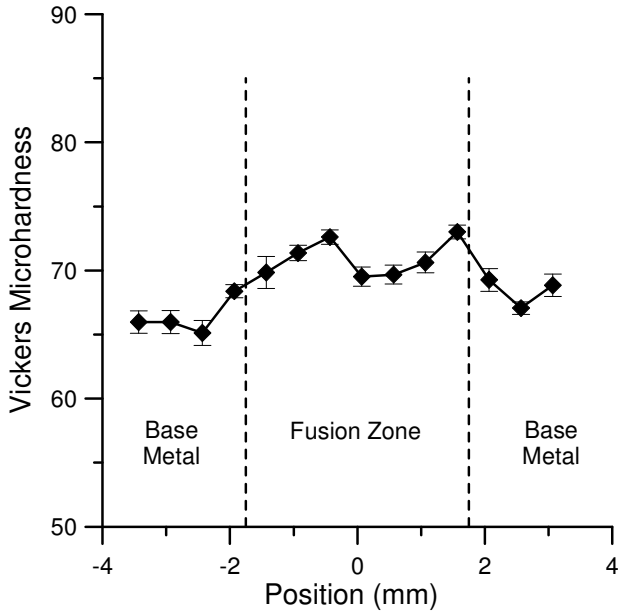

Figure 4.31: Vickers microhardness profile of lap-joint configuration DSAW weld produced using a 2 kW welding power and 15 mm/s welding speed.

Tensile-shear tests were performed using welds produced using a total welding power of 2 kW and a welding speed of 10 mm/s and 15 mm/s. Stress/strain curves obtained from the welds produced using a 10 mm/s and 15 mm/s welding speeds are shown in Figure 4.32a and Figure 4.32b, respectively. The shear strength of O temper AA5182 has been measured at 152 MPa, while the % elongation has been measured at 25% [6]. In comparison, the average shear strength for seam welds was found to be 41 ± 7.5 MPa and 32 ± 1.9 MPa while the % elongation was found to be 8.0 ± 0.03% and 8.1 ± 0.14%, at a welding speed of 10 mm/s and 15 mm/s, respectively.

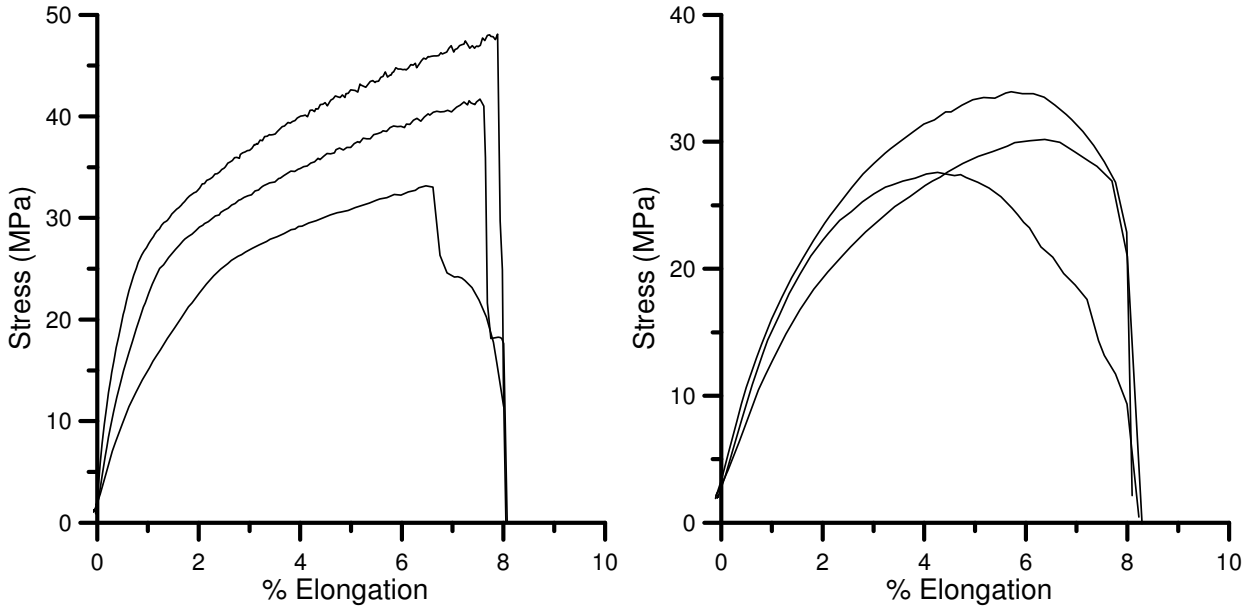

a) b)

Figure 4.32: Stress (MPa) versus % elongation plot for seam welded AA5182 sheets produced using a 2 kW welding power and ***a)*** 10 mm/s welding speed; ***b)*** 15 mm/s welding speed.

All of the welds were observed to fail in the weld metal, approximately 1 mm from the fusion zone boundary as shown in Figure 4.33. This region corresponds to the location where oxide tails were observed to form in transverse cross-sections. Since the oxide-oxide interface is unbonded, the oxide tails

would act as incipient cracks and would act as an excellent fracture initiation points. In addition, the brittle oxide layer would reduce the ductility of the weld metal and the corresponding % elongation.

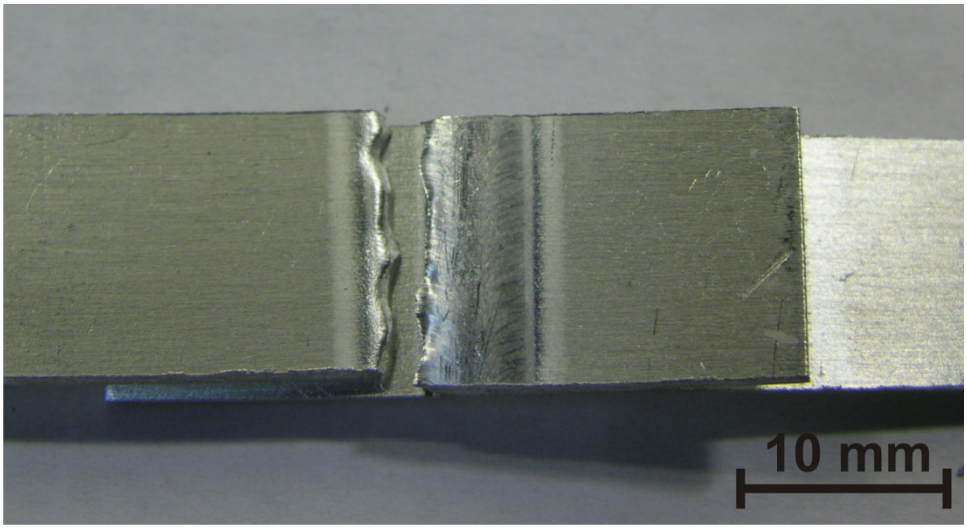

Figure 4.33: Fractured tensile specimen produced with a 2 kW welding power and a welding speed of 10 mm/s.

4.4 Fluid Flow in the DSA Weld Pools

The flow of molten metal in a conventional single arc weld pool is the result of the complex interplay between Marangoni forces, Lorentz forces, and buoyancy forces acting on the molten metal in the weld pool [44], [50]. The strength of these different forces and the resulting fluid flow can affect the properties of the weld such as the shape of the weld pool, the distribution of alloying elements, and the distribution of gas porosity and other defects [50]. The fluid flow in the weld pool can also disrupt the oxide-oxide layer, or bifilm, at the joint interface of DSAW seam welds provided it is sufficiently strong. Since the joint interface is not in contact with the arc, the bifilm cannot be removed by cathodic cleaning, and therefore, fluid flow in the molten weld pool is the only way to limit or even prevent the formation of oxide tails.

In order to better understand the fluid motion in lap-joint configuration DSA weld pools, a series of welds were produced between 1 mm thick AA5182 and 1 mm thick AA6111 at a welding power of 2 kW and at welding speeds of 10 mm/s and 15 mm/s. These conditions were used since they had previously been found to produce good quality, full penetration welds in the lap-joint configuration between overlapping 1 mm thick AA5182 sheets. Each alloy would produce a different response to chemical etching due to the difference in magnesium content, allowing the effects of fluid motion to be visualized. Within this series, one set of welds was produced by placing the AA5182 sheet above the AA6111 sheet, and another set of welds was produced with the AA6111 sheet above the AA5182 sheet. This was done to determine whether the small difference in density between the two alloys could be used to increase the buoyancy driven fluid flow in the weld pool and reduce the formation of oxide tails.

Figure 4.34 shows photographs of a set of the weld beads produced with the AA6111 sheet placed above the AA5182 sheet. Figure 4.35 shows photographs of a set of welds produced with the AA5182 sheet placed above the AA6111 sheet. All welds exhibited excellent cathodic cleaning on both sides of the workpiece. Although all welds were produced autogeneously, the weld bead produced in the AA6111 alloy was free of cracking. The weld shown in Figure 4.34c and Figure 4.34d was a partial penetration weld. All other welds were full penetration welds.

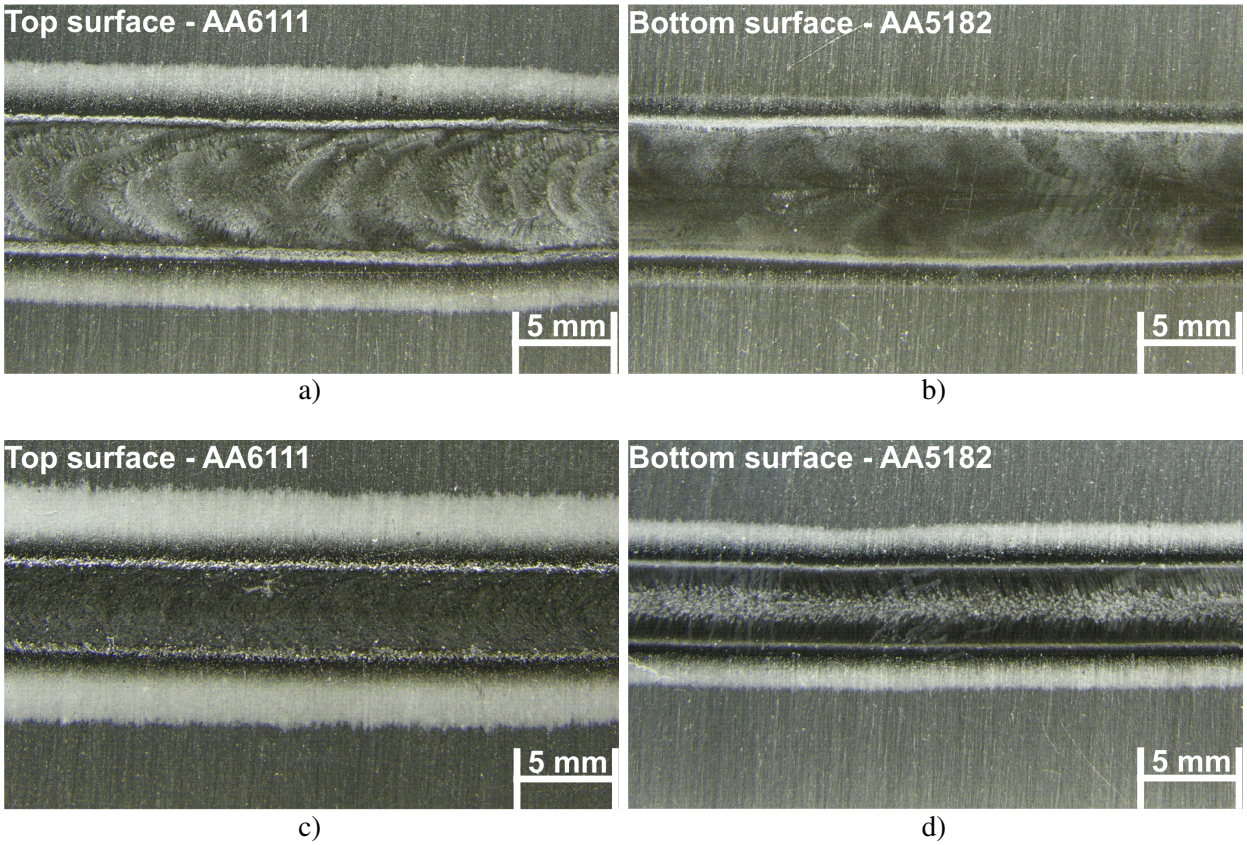

Figure 4.34: Photographs of welds produced between 1 mm thick AA6111 and AA5182 using 2 kW welding power and welding speeds of: ***a),b)*** 10 mm/s welding speed; **c*****),d)*** 15 mm/s welding speed.

Figure 4.36 shows two transverse cross sections from the weld shown in Figure 4.34a, where the slightly higher density AA6111 alloy sheet was on the top and the less dense AA5182 sheet was below. The darker regions represent the microstructure of the AA6111 alloy while the lighter regions represent the microstructure of the AA5182 alloy. From Figure 4.36a, it is apparent that the denser AA6111 alloy has been pulled downwards by gravity and the less dense AA5182 alloy has been displaced to the top of the weld pool. The overall appearance of the weld pool suggests that a bulk movement of fluid has occurred as opposed to a stirring action between the two alloys. The region closest to the fusion zone

shows virtually no mixing and consists mostly of AA5182 alloy. Short oxide tails are also apparent in this region.

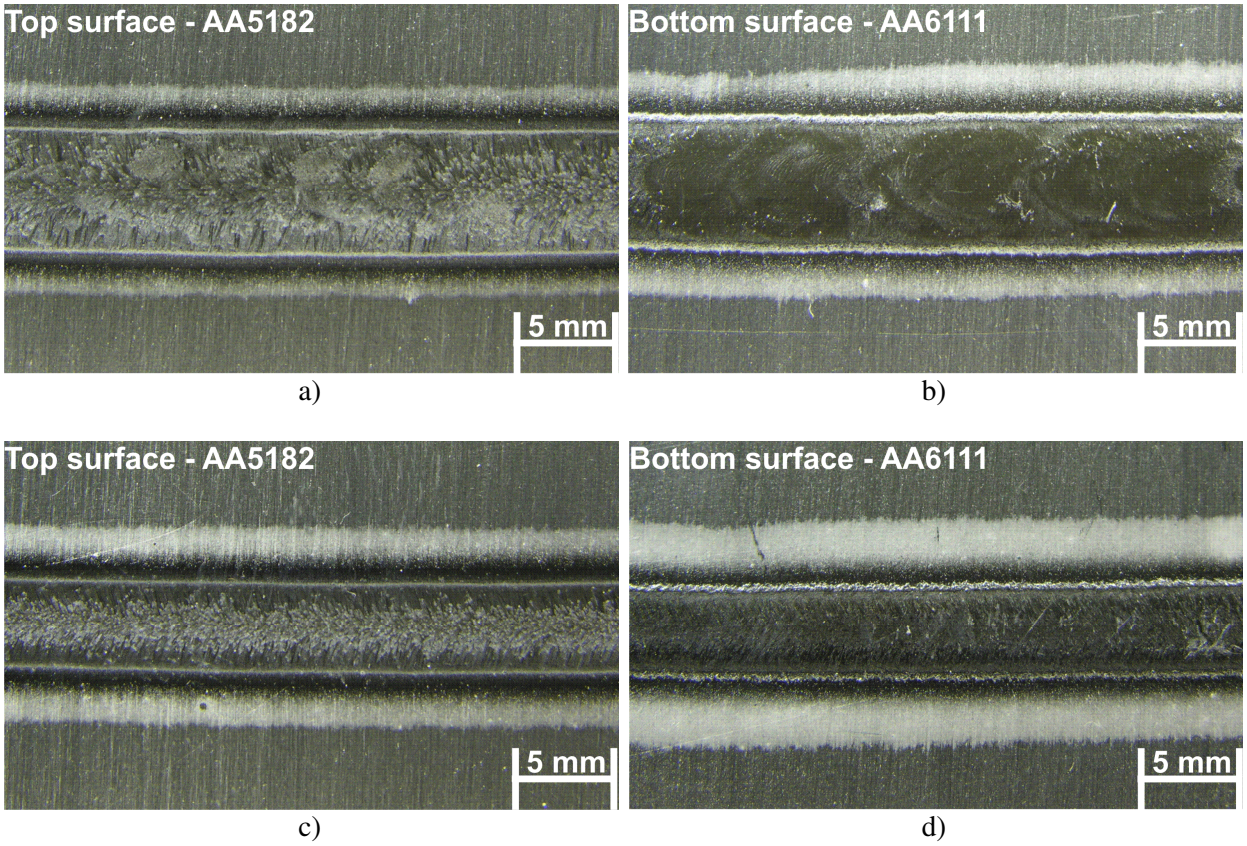

Figure 4.35: Photographs of seam welds produced between 1 mm thick AA5182 and AA6111 using 2 kW welding power and welding speeds of: ***a),b)*** 10 mm/s welding speed; **c*),d)*** 15 mm/s welding speed.

The cross section shown in Figure 4.36b also shows similar movement, but a mild swirling pattern can also be seen in the left corner of the weld pool. Although the force of gravity has pulled a large pocket of AA6111 alloy towards the bottom of the weld pool, much of the AA6111 alloy is interspersed with AA5182 alloy. This suggests that there are other forces in the weld pool strong enough to counteract the force of gravity and keep the denser alloy at the top of the weld pool and push the less dense AA5182 alloy towards the bottom. However, since the weld pool does not display a homogeneous microstructure,

the forces in the weld pool and the resulting fluid flow and mixing is considered to be quite weak. In fact, the fluid flow appears to be overpowered by the buoyancy force of hydrogen gas pores which have nucleated along an oxide tail and caused it to float upwards in the area closest to the fusion zone, trapping a layer of AA6111 alloy at the top of the weld bead.

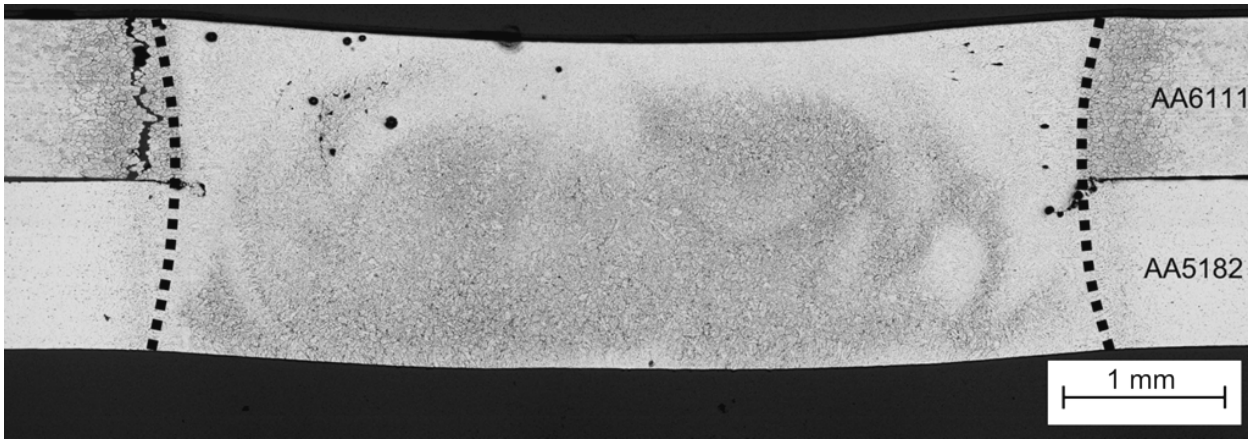

a)

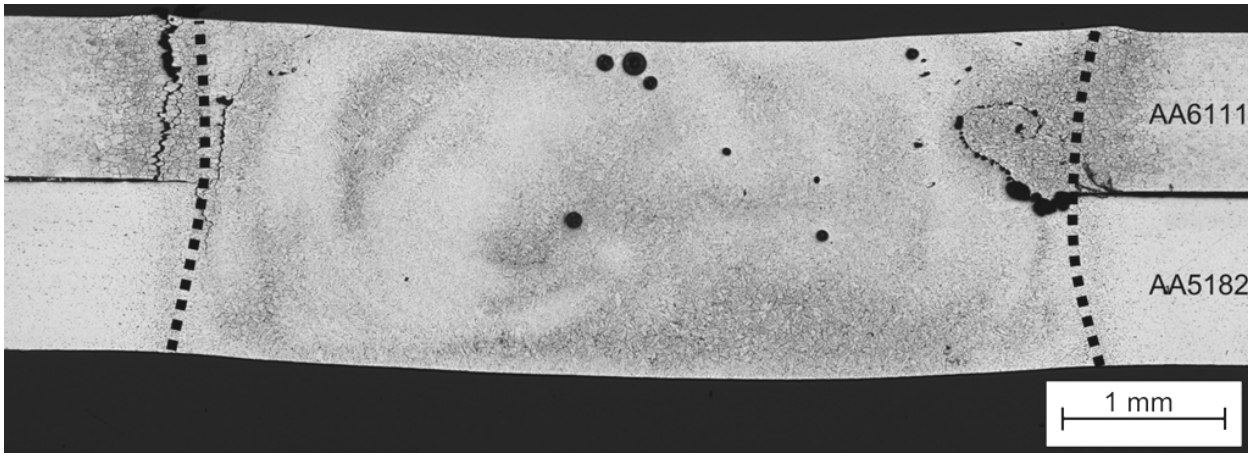

b)

Figure 4.36: Two cross sections of a seam weld produced between 1 mm thick AA6111 and AA5182 sheets with a 10 mm/s welding speed.

Figure 4.37 shows two transverse cross sections from the weld shown in Figure 4.35, where the slightly less dense AA5182 alloy was placed above the more dense AA6111 sheet. Neither of the cross

sections shown in Figure 4.37 displayed any mixing between the two alloys. The denser AA6111 alloy has remained at the bottom of the weld pool while the less dense AA5182 alloy has remained at the top of the weld pool. This suggests that the weld pool is very quiescent with very little fluid flow. However, the oxide tails are quite short although there is very little mixing.

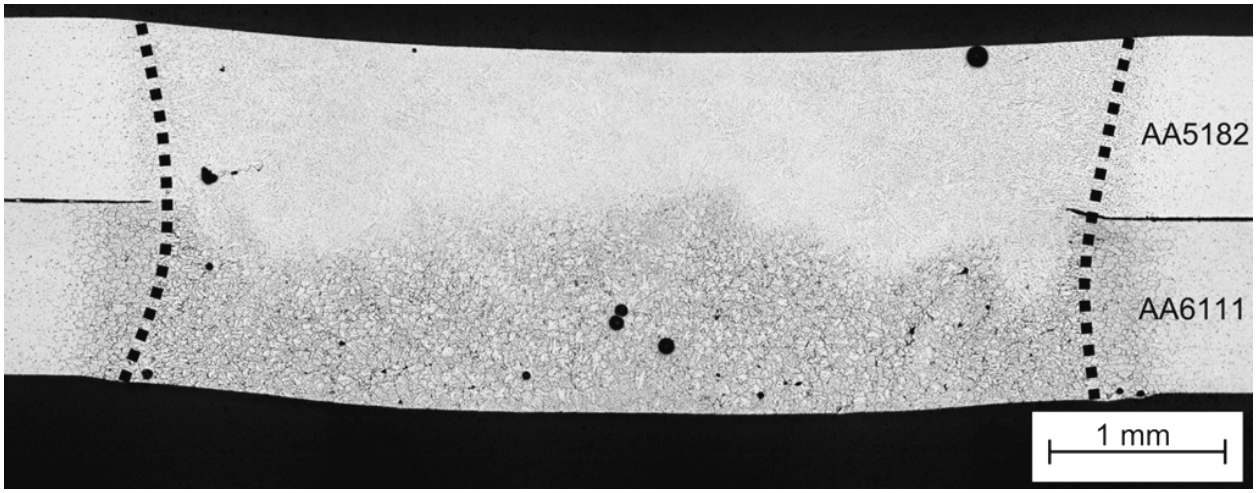

a)

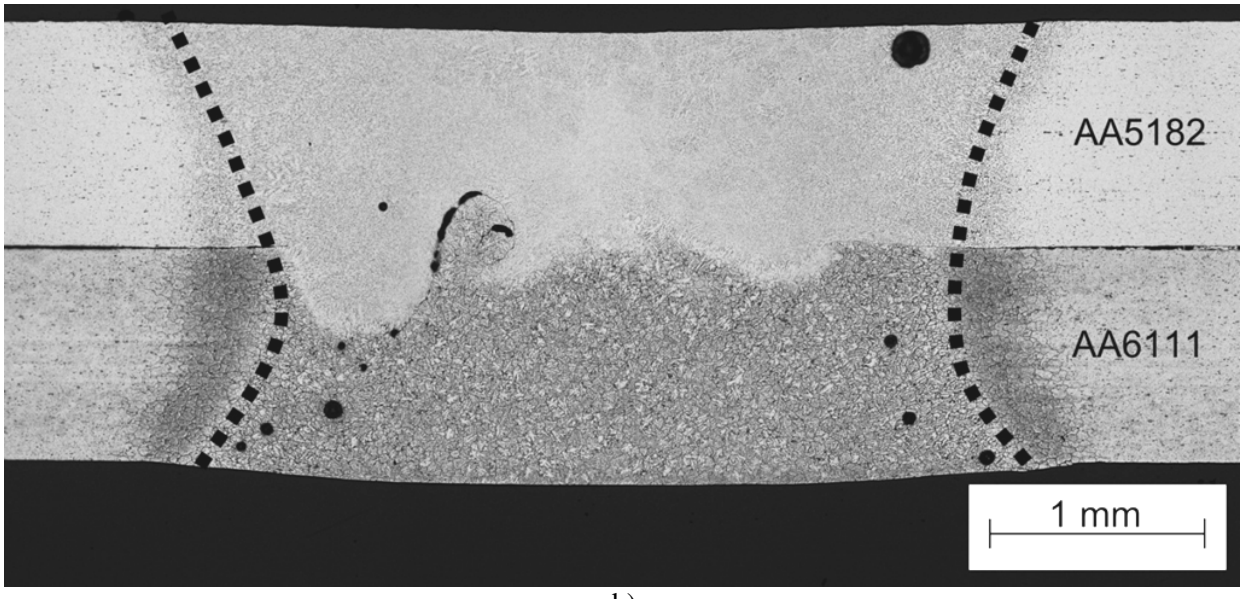

b)

Figure 4.37: Two cross sections of a seam weld produced between 1 mm thick AA5182 and AA6111 sheets with a 2 kW welding power and a welding speed of: ***a)*** 10 mm/s; ***b)*** 15 mm/s.

There appears to be a minor amount of mixing at the interface between the two alloys in the cross-section of the weld pool shown in Figure 4.37b. However, this movement appears to be caused by the movement of the oxide tail which may have been driven by the buoyant nature of the hydrogen gas pores that have nucleated along the oxide tail. The swirling motion of this oxide tail has displaced some of the AA5182 alloy into the bottom of the weld, and carried a small amount of AA6111 alloy into the top half of the weld.

As discussed in Section 2.1.3, Marangoni forces, Lorentz forces, and buoyancy forces are the three main forces that can drive fluid flow in a weld pool. Marangoni forces and Lorentz forces are typically dominant over Lorentz forces, and buoyancy forces are considered to be the weakest of the three driving forces in an arc weld pool. Since the two alloys were not stirred together to produce a homogeneous microstructure, there does not appear to be any clear evidence of strong Marangoni convection or Lorentz force driven fluid flow. The absence of Marangoni convection may be explained by the presence of a solid, immobile aluminum oxide layer on the weld surface. Even though rigorous cleaning of the pre-existing oxide had been performed and cathodic cleaning had been used, an aluminum oxide layer can form when exposed to even trace amounts of oxygen and even a monotomic layer of oxide on the weld pool surface would dampen Marangoni flow in aluminum welds. Lorentz forces also do not contribute to fluid flow in the DSA weld pool because the welding current travels straight through the workpiece since the welding specimen is not part of the welding circuit, and the resultant Lorentz force always acts in the radial direction. If the workpiece was part of the welding circuit, the welding current would no longer travel straight through the welding specimen and the resultant Lorentz force could act in several directions to create a stirring motion in the weld pool. Although a weak buoyancy force was induced in the weld pool when the denser AA6111 sheet was placed above the less dense AA5182 sheet, this force was not strong enough to produce a homogeneous composition in the weld pool. Similar behaviour was

also observed by Howard *et al.* [53] during a study of conduction-mode high-power diode laser welds produced in AA5182 in the lap-fillet configuration. Overall, the minor amount of fluid motion observed in the weld pools appears to have had little effect on oxide formation. However, the presence of gas pores on the oxide tails did appear to influence their movement and growth. Since the gas pores have a tendency to float upwards, they can easily pull and further enlarge the neutrally buoyant oxide tails.

Overall, the DSA weld pools observed in this study were found to be very quiescent. Buoyancy forces brought about by small differences in density due to differences in composition were found to be the primary driver of fluid flow in DSA weld pools formed between dissimilar alloy sheets. This shows that the buoyancy force in the weld pool can be affected by small differences in density due to a slight variation in composition, but is incapable of breaking up the thin oxide layers between the two sheets.

Chapter 5: Summary and Conclusions

The main purpose of this study was to examine the feasibility of producing lap-joint configuration seam and spot welds in thin AA5182 sheet using the double-sided arc welding (DSAW) process. In addition, identifying methods for reducing hydrogen gas porosity and characterizing the fluid flow in DSA weld pools were also studied.

5.1 Effects of Specimen Pre-cleaning on Hydrogen Gas Porosity

The surface of the 1 mm thick AA5182-O aluminum sheet used during this study was saturated with rolling lubricants and possessed a very thick, hydrated aluminum oxide layer that could not be completely removed by degreasing and stainless steel wire brushing. Therefore, more aggressive cleaning techniques were studied to determine their effect on gas porosity formation. Deoxidizing the specimens in a 5% sodium hydroxide solution and desmutting them in a nitric acid solution was found to significantly reduce the amount of gas porosity in welds. Welds produced in specimens that were power wire brushed prior to welding were found to contain slightly more porosity than welds produced in specimens that were manually wire brushed prior to welding. The most effective technique for reducing weld porosity used a combination of degreasing, deoxidizing, and desmutting, followed by manual wire brushing just prior to welding. Ensuring specimen cleanliness was found to be a critical step towards producing good quality welds with minimal porosity.

The effects of shielding gas flow and turbulence in the gas plume on hydrogen gas porosity were also studied. When high shielding gas flow rates were used, welds produced using a short torch-to-workpiece distance were found to contain more gas porosity than welds produced with a longer torch-to-workpiece distance. With a longer torch-to-workpiece distance, the shielding gas plume was wider and would have

possessed lower kinetic energy near the weld pool which would reduce the risk of mixing room air into the gas plume. Although increasing the torch-to-workpiece distance was found to reduce porosity, it also has the undesirable effect of reducing the process efficiency and increasing the torch voltage.

Another method which can improve the distribution of shielding gas is to promote more laminar flow in the shielding cup. The original shielding cup for the top Thermal Arc torch was modified by replacing part of the conical section with a straight section to reduce gas velocity, and by inserting a gas lense to promote more laminar flow. Welds produced using the modified shielding gas cup were found to contain only trace amounts of gas porosity, provided that they were fully cleaned prior to welding. Overall, welds produced using the modified shielding cup with the Thermal Arc torch, a shielding gas flow rate of 10 lpm, and a torch-to-workpiece distance of 2 mm were found to contain the least amount of porosity.

5.2 Feasibility of Spot Welding using the DSAW Process

The feasibility of using the DSAW process to produce spot welds in thin aluminum sheet was investigated to determine whether DSAW could be used as an alternative to RSW. Visually acceptable welds of sufficient diameter were produced using a welding current as low as 50 A and a weld time of one second. These defects were found to reduce the strength and quality of the DSA spot welds. All of the welds produced during this study exhibited crater cracking, solidification shrinkage cracking, and in some cases, solidification shrinkage porosity. By observing the formation and solidification of the weld pool using a laser strobe imaging system, it was determined that these defects were a characteristic of the solidification behaviour of the welds. In the absence of a fresh supply of molten metal, any cavities caused by solidification shrinkage remained unfilled. Hydrogen gas porosity and aluminum oxide entrainment were also present in the welds.

5.3 Feasibility of Seam Welding using the DSAW Process

The feasibility of using the DSAW process for the production of lap-joint configuration seam welding was investigated by determining the range of welding powers and speeds which would produce visually acceptable welds between 1 mm thick AA5182 sheets. Acceptable welds were produced using welding powers ranging from 2 kW to 5 kW, and welding speeds ranging from 10 mm/s to 70 mm/s, which corresponds to a heat input ranging from 78 J/mm to 203 J/mm. Insufficient heat inputs resulted in welds with insufficient fusion between the sheets, while excessive heat inputs created blowholes in the workpiece. All welds were found to exhibit excellent cathodic cleaning on both sides of the workpiece and a beneficial columnar-equiaxed grain transition. Varying amounts of oxide entrainment were seen in the transverse cross-sections of the welds.

No correlation appeared to exist between the welding parameters and the oxide tail length. The oxide tails were reduced in length, but not eliminated by cleaning the specimens using a combination of degreasing, deoxidizing, and manual stainless steel wire brushing. Microhardness testing revealed that there was no significant change in hardness across the base metal, heat affected zone, and fusion zone. The shear strength and % elongation of the O-temper base metal was observed to be at least three times greater than the shear strength and % elongation of the welded specimens. All of the specimens were observed to fail in the weld metal, approximately 1 mm from the fusion zone boundary. In transverse cross-sections, this region corresponds to the area where oxide tails were observed to exist.

5.4 Fluid Flow and Oxide Entrainment in DSA Weld Pools

A series of welds were produced between AA5182 and AA6111 sheet to determine whether any fluid flow exists in the DSA weld pool. The difference in composition would produce a different response to chemical etching and allow any fluid motion in the weld pool to be easily visualized. When the slightly

denser AA6111 sheet was placed on top of the AA5182 sheet, the resulting weld showed some minor swirling in the weld pool as a result of the difference in density between the two alloys. However, the microstructure of the weld was comprised of distinct pockets of AA5182 and AA6111, rather than a homogeneous microstructure which suggests that the fluid flow was weak. Another series of welds were produced by placing the less dense AA5182 sheet on top of the AA6111 sheet. The welds produced in this condition were found to be stagnant and there was no interaction between the two alloys. Overall, the DSA weld pool produced between dissimilar aluminum alloys was observed to be very quiescent, and only weak buoyancy driven fluid flow was found to exist when the difference in density was able to drive fluid flow.

Appendix A – ANOVA Results from Cleaning Experiments

General Linear Model: % Porosity versus Degreasing, De-oxidizing, ...

```
Factor         Type   Levels  Values
Degreasing     fixed       2  no, yes
De-oxidizing   fixed       2  no, yes
Wire Brushing  fixed       3  no, manual, auto
```

Analysis of Variance for % Porosity, using Adjusted SS for Tests

Source	DF	Seq SS	Adj SS	Adj MS	F	P
Degreasing	1	10.0499	10.0499	10.0499	29.62	0.000
De-oxidizing	1	18.9939	18.9939	18.9939	55.98	0.000
Wire Brushing	2	17.0457	17.0457	8.5229	25.12	0.000
Degreasing*De-oxidizing	1	3.0423	3.0423	3.0423	8.97	0.004
Degreasing*Wire Brushing	2	3.4674	3.4674	1.7337	5.11	0.009
De-oxidizing*Wire Brushing	2	8.8777	8.8777	4.4388	13.08	0.000
Degreasing*De-oxidizing* Wire Brushing	2	4.0702	4.0702	2.0351	6.00	0.004
Error	60	20.3569	20.3569	0.3393		
Total	71	85.9041				

```
S = 0.582479   R-Sq = 76.30%   R-Sq(adj) = 71.96%
```

Term			Coef	SE Coef	T	P
Constant			0.91763	0.06865	13.37	0.000
Degreasing						
no			0.37361	0.06865	5.44	0.000
De-oxidizing						
no			0.51362	0.06865	7.48	0.000
Wire Brushin						
no			0.67922	0.09708	7.00	0.000
manual			-0.43506	0.09708	-4.48	0.000
Degreasing*De-oxidizing						
no	no		0.20556	0.06865	2.99	0.004
Degreasing*Wire Brushin						
no	no		0.30680	0.09708	3.16	0.002
no	manual		-0.19395	0.09708	-2.00	0.050
De-oxidizing*Wire Brushin						
no	no		0.49639	0.09708	5.11	0.000
no	manual		-0.23602	0.09708	-2.43	0.018
Degreasing*De-oxidizing*Wire Brushin						
no	no	no	0.33093	0.09708	3.41	0.001
no	no	manual	-0.11391	0.09708	-1.17	0.245

Unusual Observations for % Porosity

Obs	% Porosity	Fit	SE Fit	Residual	St Resid
13	6.20927	3.82376	0.23780	2.38551	4.49 R

19	2.61007	1.38996	0.23780	1.22010	2.29	R
25	2.04908	3.82376	0.23780	-1.77468	-3.34	R

R denotes an observation with a large standardized residual.

Least Squares Means for % Porosity

			Mean	SE Mean
Degreasing				
no			1.2912	0.09708
yes			0.5440	0.09708
De-oxidizing				
no			1.4312	0.09708
yes			0.4040	0.09708
Wire Brushin				
no			1.5969	0.11890
manual			0.4826	0.11890
auto			0.6735	0.11890
Degreasing*De-oxidizing				
no	no		2.0104	0.13729
no	yes		0.5721	0.13729
yes	no		0.8521	0.13729
yes	yes		0.2360	0.13729
Degreasing*Wire Brushin				
no	no		2.2773	0.16815
no	manual		0.6622	0.16815
no	auto		0.9342	0.16815
yes	no		0.9164	0.16815
yes	manual		0.3029	0.16815
yes	auto		0.4127	0.16815
De-oxidizing*Wire Brushin				
no	no		2.6069	0.16815
no	manual		0.7602	0.16815
no	auto		0.9267	0.16815
yes	no		0.5868	0.16815
yes	manual		0.2050	0.16815
yes	auto		0.4202	0.16815
Degreasing*De-oxidizing*Wire Brushin				
no	no	no	3.8238	0.23780
no	no	manual	1.0315	0.23780
no	no	auto	1.1760	0.23780
no	yes	no	0.7308	0.23780
no	yes	manual	0.2930	0.23780
no	yes	auto	0.6924	0.23780
yes	no	no	1.3900	0.23780
yes	no	manual	0.4889	0.23780
yes	no	auto	0.6774	0.23780
yes	yes	no	0.4429	0.23780
yes	yes	manual	0.1170	0.23780
yes	yes	auto	0.1480	0.23780

Appendix B – Comparison of the Average Area Fraction of Porosity in DSA Spot Welds Produced using a Ramp Down Time

Observation	0 sec ramp down time	2 sec ramp down time
1	3.478001	4.255902
2	3.459668	4.519344
3	1.282572	4.509655
4	0.937433	1.689864
5	0.231277	4.559667
Mean:	1.87779	3.906886
STDEV:	1.501047	1.245146
alpha:	0.05	
H0:	avg1 = avg2	
v (DOF):	9.669893 ≈9	
Reject H0 if: T0*>2.262, or T0*<-2.262		
T0*:	-2.326452	
T0* lies outside the range of acceptance, therefore reject H0		
CONCLUSION: avg1 not equal to avg2		

Observation	2 sec ramp down time	4 sec ramp down time
1	4.255902	3.255679
2	4.519344	5.493976
3	4.509655	4.796369
4	1.689864	5.676361
5	4.559667	5.164395
Mean:	3.906886	4.877356
STDEV:	1.245146	0.96662
alpha:	0.05	
H0:	avg1 = avg2	
v (DOF):	9.420917 ≈9	
T0*:	-1.37666	
T0* lies inside the range of acceptance, therefore can't reject H0		
CONCLUSION: avg1 equal to avg2		

Observation	4 sec ramp down time	10 sec ramp down time
1	3.255679	3.04642
2	5.493976	3.439854
3	4.796369	3.332195
4	5.676361	5.118961
5	5.164395	4.713299
Mean:	4.877356	
STDEV:	0.96662	3.930146
alpha:	0.05	
H0:	avg1 = avg2	
v (DOF):	9.978456≈9	
Reject H0 if: T0*>2.262, or T0*<-2.262		
T0*:	1.584978	
T0* lies inside the range of acceptance, therefore can't reject H0		
CONCLUSION: avg1 equal to avg2		

Observation	2 sec ramp down time	10 sec ramp down time
1	4.255902	3.04642
2	4.519344	3.439854
3	4.509655	3.332195
4	1.689864	5.118961
5	4.559667	4.713299
Mean:	3.906886	
STDEV:	1.245146	3.930146
alpha:	0.05	
H0:	avg1 = avg2	
v (DOF):	8.30652 ≈8	
Reject H0 if: T0*>2.306, or T0*<-2.306		
T0*:	-2.6046	
T0* lies outside the range of acceptance, therefore reject H0		
CONCLUSION: avg1 not equal to avg2		

Appendix C – Arc Efficiency and Arc Distribution Values used in the Analytical Thermal DSAW Model

Welding Power (kW)	Welding Speed (mm/s)	Top Torch Arc Efficiency (%), Arc distribution (m)	Top Torch Arc Efficiency (%), Arc distribution (m)
2	10	0.325, 0.0015	0.325,0.00145
	15	0.33, 0.0015	0.33,0.00145
	20	0.33, 0.0015	0.33,0.00145
3	20	0.33, 0.0016	0.33,0.00155
	25	0.335, 0.0016	0.335,0.00155
	30	0.345, 0.0016	0.345,0.00155
	35	0.35, 0.0016	0.35,0.00155
4	30	0.32, 0.00165	0.32,0.0016
	35	0.33, 0.00165	0.33,0.0016
	40	0.33, 0.00165	0.33,0.0016
	45	0.35, 0.00165	0.35,0.0016
	50	0.36, 0.00165	0.36,0.0016
5.1	55	0.34, 0.0017	0.34,0.00165
	60	0.35, 0.0017	0.35,0.00165
	65	0.35, 0.0017	0.35,0.00165
	70	0.38, 0.0017	0.38,0.00165

References

[1] A. Kelkar, R. Roth, and J. Clark, "Automobile Bodies: Can Aluminum Be an Economical Alternative to Steel?," *JOM*, 2001, Vol. 53, No. 8, pp. 28-32.

[2] J. Lamm, "2004 Jaguar XJ & XJR - First Drive," *Road and Track*, p. 43, June 2003.

[3] Automotive Manufacturing Solutions, "Lightweighting the perfect body," *Automotive Manufacturing Solutions*, pp. 44-46, November/December 2009.

[4] F. Stodolsky, A. Vyas, R. Cuenca, and L. Gaines, "Life-cycle energy savings potential from aluminum-intenstive vehicles," SAE, Warrendale, PA, SAE Technical Paper Series 951837.

[5] H. Helms, U. Lambrecht, and U. Hopfner, "Energy savings by light-weighting," IFEU Heidelberg, Heidelberg, 2003.

[6] *ASM Handbook Vol. 2: Properties and Selection: Nonferrous Alloys and Special-Purpose Materials*. Materials Park, OH: ASM Int'l, 1993.

[7] T. Auty and B. Lewinski, "Laser Blank Welding – A Global Perspective," in *ATTCE 2001 Proceedings Volume 3: Manufacturing*, Barcelona, Spain, 2001, pp. 43-50.

[8] H. Zhao, D.R. White, and T. DebRoy, "Current issues and problems in laser welding of automotive aluminium alloys," *International Materials Reviews*, 1999, Vol. 44, No. 6, pp. 238-266.

[9] S. Sasabe, N. Eguchi, and T. Matsumoto, "Laser welding characteristics of aluminium alloys for automotive applications," *Weld. Int'l.*, 2003, Vol. 17, No. 11, p. 870 — 878.

[10] X. Cao, W. Wallace, J.P. Immarigeon, and C. Poon, "Research and Progress in Laser Welding of Wrought Aluminum Alloys. II. Metallurgical Microstructures, Defects, and Mechanical Properties," *Materials and Manufacturing Processes*, 2003, Vol. 18, No. 1, pp. 23-49.

[11] M. Deutsch, "Effects of Nd:YAG laser welding and VPPAW welding process variables on weld geometry and defects of 1.6 mm thick 5182 aluminum," University of Waterloo, Waterloo, MASc Thesis 2001.

[12] A. Punkari, "Variable Polarity Plasma Arc Welding and Dual-Beam Nd:YAG Laser Welding of Aluminum Alloys," University of Waterloo, Waterloo, MASc thesis 2002.

[13] K. , Iwase, T. , Sakamoto, H. , Kasukawa, M. , Chiba, K. and Saeki, H. Shibata, "Welding of aluminium tailored blanks by Nd: YAG lasers," *Weld. Int'l.*, 2003, Vol. 17, No. 4, pp. 282-286.

[14] L. R. Morris, "Formability of Aluminum Sheet Alloys," in *Aluminum Transformation Technology and Applications*, C.A. Pampillo, Ed. Metals Park, OH: American Society for Metals, 1982, pp. 549–582.

[15] M.J. Cieslak and P.W. Fuerschbach, "On the Weldability, Composition, and Hardness of Pulsed and Continuous Nd:YAG Laser Welds in Aluminum Alloys 6061,5456, and 5086," *Metall. Trans. B*, 1988, Vol. 19, No. 2, pp. 319-329.

[16] A. Haboudou, P. Peyre, A.B. Vannes, and G. Peix, "Reduction of porosity content generated during Nd:YAG laser welding of A356 and AA5083 aluminium alloys," *Materials Science & Engineering A*, 2003, Vol. 363, No. 1-2, pp. 40-52.

[17] *Welding Handbook Volume 2*, 8th ed. Miami, FL: American Welding Society, 1991.

[18] M.K. Yadava, R.S. Mishra, Y.L. Chen, B. Carlson, and G.J. Gran, "Study of friction stir joining of thin aluminium sheets in lap joint configuration," *Sci. Technol. Weld. Join.*, 2010, Vol. 15, No. 1, pp. 70-75.

[19] S. A. David, W. M. Thomas, E. Lara-Curzio, S. S. Babu G. M. D. Cantin, "Friction Skew-stir welding of lap joints in 5083–0 aluminium," *Sci. Technol. Weld. Join.*, 2005, Vol. 10, No. 3, pp. 268-280.

[20] C. Lee et al., "Lap joint properties of FSWed dissimilar formed 5052 Al and 6061 Al alloys with different thickness," *J. Mater. Sci.*, 2008, Vol. 43, No. 9, pp. 3296–3304.

[21] W.M. Thomas, K.L. Johnson, and C.S. Wiesner, "Friction Stir Welding - Recent Developments in Tool and Process Technologies," *Advanced Engineering Materials*, 2003, Vol. 5, No. 7, pp. 485-490.

[22] L. Cederqvist and A. P. Reynolds, "Factors Affecting the Properties of Friction Stir Welded Aluminum Lap Joints," *Weld. J.*, 2001, Vol. 80, No. 12, pp. 281–287.

[23] V. Soundararajan, E. Yarrapareddy, and R. Vovacevic, "Investigation of the Friction Stir Lap Welding of Aluminum Alloys AA 5182 and AA 6022," *J.Materials Engineering and Performance*, 2007, Vol. 16, No. 4, pp. 477-484.

[24] *ASM Handbook Vol. 6: Welding Brazing and Soldering*. Materials Park, OH: ASM Int'l, 1993.

[25] S. Fukumoto, I. Lum, E. Biro, D.R. Boomer, and Y. Zhou, "Effects of Electrode Degradation on Electrode Life in Resistance Spot Welding of Aluminum Alloy 5182," *Weld. J.*, 2003, Vol. 82, No. 11, pp. 307s - 312s.

[26] C.L. Tsai, "Advances in the Resistance Welding of Automotive Aluminum," *JOM*, May 1997, Vol. 49, No. 5, pp. 28-30.

[27] A. Fujiwara and S. Sasabe, "Welded joint strength of thin aluminium structures," *Welding International*, 2002, Vol. 16, No. 11, pp. 851-859.

[28] I. Lum, S. Fukumoto, E. Biro, D.R. Boomer, and Y. Zhou, "Electrode Pitting in Resistance Spot Welding of Aluminum Alloy 5182," *Metall. Mater. Trans. A*, 2004, Vol. 35, No. 1, pp. 217-226.

[29] B.H. Chang, D. Du, Q. Chen, and Y. Zhou, "Studies on the effects of pitting morphology in resistance spot welding of aluminum alloy," *Sci. Technol. Weld. Join.*, 2007, Vol. 12, No. 1, pp. 67-72.

[30] E.P. Patrick, J.R. Auhl, and T.S. Sun, "Understanding the Process Mechanisms Is Key to Reliable Resistance Spot Welding Aluminum Auto Body Components," SAE, Warrandale, PA, SAE Technical Paper No. 840291, 1984.

[31] M. Rashid, S. Fukumoto, J.B. Medley, J. Villafuerte, and Y. Zhou, "Influence of Lubricants on Electrode Life in Resistance Spot Welding of Aluminum Alloys," *Weld. J.*, 2007, Vol. 86, No. 3, pp. 62s-70s.

[32] M. A. R. Yarmuch and B. M. Patchett, "Variable AC Polarity GTAW Fusion Behavior in 5083 Aluminum," *Weld. J.*, 2007, Vol. 86, No. 7, pp. 196s-200s.

[33] M. M. Mossman and J. C. Lippold, "Weldability Testing of Dissimilar Combinations of 5000 and 6000-Series Aluminum Alloys," *Weld. J.*, 2002, Vol. 81, No. 9, pp. 188s-194s.

[34] S. Subramaniam, D.R. White, J. E. Jones, and D.W. Lyons, "Experimental Approach to Selection of Pulsing Parameters in Pulsed GMAW," *Weld. J.*, 1999, Vol. 78, No. 5, pp. 166s-172s.

[35] C. Huang and S. Kou, "Liquation Cracking in Partial-Penetration Aluminum Welds: Effect of Penetration Oscillation and Backfilling," *Weld. J.*, 2003, Vol. 82, No. 7, pp. 184s-194s.

[36] Y. Shi, X. Liu, Y. Zhang, and M. Johnson, "Analysis of Metal Transfer and Correlated Influences in Dual-Bypass GMAW of Aluminum," *Weld. J.*, 2008, Vol. 87, No. 9, pp. 229-s -

236-s.

[37] B. Zheng, H.J. Wang, Q.I. Wang, and R. Kovacevic, "Control for Weld Penetration in VPPAW of Aluminum Alloys Using the Front Weld Pool Image Signal," *Weld. J.*, 2000, Vol. 79, No. 12, pp. 363-s - 371-s.

[38] Y.M. Zhang, S.B. Zhang, and M. Jiang, "Sensing and Control of Double-Sided Arc Welding Process," *Journal of Manufacturing Science and Engineering*, 2002, Vol. 124, No. 3, pp. 695-701.

[39] Y.M. Zhang and S.B. Zhang, "Method of arc welding using dual serial opposed torches," US Patent no. 5,990,446, Nov 23, 1999.

[40] Y.M. Zhang, C. Pan, and A.T. Male, "Solidification Behavior of Al-Mg Aluminum Alloy Using Double-Sided Arc Welding Process," *J. Mater. Sci. Letters*, 2000, Vol. 19, No. 10, pp. 831-833.

[41] Y.M. Zhang, C. Pan, and A.T. Male, "Improved Microstructure and Properties of 6061 Aluminum Alloy Weldments Using a Double-Sided Arc Welding Process," *Metall. and Mat. Trans. A*, 2000, Vol. 31, No. 10, pp. 2537-2543.

[42] Y.M. Zhang, S.B. Zhang, and M. Jiang, "Keyhole Double-Sided Arc Welding Process," *Weld. J.*, 2002, Vol. 81, No. 11, pp. 249s-255s.

[43] Y.M. Zhang and S.B. Zhang, "Double-Sided Arc Welding Increases Weld Joint Penetration," *Weld. J.*, 1998, Vol. 77, No. 6, pp. 57-61.

[44] S. Kou, *Welding Metallurgy*, 2nd ed. Toronto: John Wiley & Sons, 2003.

[45] Y. Kwon and D.C. Weckman, "Double sided arc welding of AA5182 aluminum alloy sheet," *Sci. Technol. Weld. Join.*, 2008, Vol. 13, No. 6, pp. 485-495.

[46] J.A. Moulton and D.C. Weckman, "Double-Sided Arc Welding of AA5182-O Aluminum Sheet for Tailor Welded Blank Applications," *Weld. J.*, 2010, Vol. 89, No. 1, pp. 11s-23s.

[47] Y. Kwon, "Double-Sided Arc Welding of AA5182 Aluminum Alloy Sheet," University of Waterloo, Waterloo, MASc thesis 2003.

[48] T. Okada, Y. Iwamoto, Y. Wakino, H. Yamamota, and K. Okazaki, "The effects of polarity in TIG arc welding of aluminum with thryistor controlled power source," *J. Light Met. Weld. Constr.*, 1982, Vol. 16, No. 12, pp. 537-543.

[49] P. W. Fuerschbach, "Cathodic Cleaning and Heat Input in Variable Polarity Plasma Arc Welding

of Aluminum," *Weld. J.*, 1998, Vol. 77, No. 2, pp. 76s-85s.

[50] Robert W. Messler, *Principles of Welding*, 1st ed. Berlin: Wiley-VCH, 2004.

[51] S. Kou and D.K. Sun, "Fluid flow and weld penetration in stationary arc welds," *Metallurgical Transactions* , Feb 1985, Vol. 16A, pp. 203-213.

[52] H. Dong, H. Gao, and L. Wu, "Numerical simulation of heat transfer and fluid flow in a double-sided gas-tungsten arc welding process," *Proc. Instn Mech. Engrs, Part B: J. Engineering Manufacture*, 2003, Vol. 217, No. 1, pp. 87-97.

[53] K. Howard, S. Lawson, and Y. Zhou, "Welding Aluminum Sheet Using a High-Power Diode Laser," *Weld. J.*, 2006, Vol. 85, No. 5, pp. 101s-110s.

[54] Jeffrey A. Moulton, "Double-Sided Arc Welding of AA5182 Aluminum Tailor Welded Blanks," University of Waterloo, Waterloo, MASc thesis 2008.

[55] J.F. Lancaster, *The Physics of Welding*, 2nd ed., J.F. Lancaster, Ed. Willowdale, ON: Pergamon Press Canada, 1986.

[56] *ASM Handbook Vol 15: Casting*. Materials Park, OH: ASM Int'l, 1993.

[57] A.M. Samuel and F.H. Samuel, "Various aspects involved in the production of low-hydrogen aluminium castings," *J. Mat. Sci.*, 1992, Vol. 27, No. 24, pp. 6533-6563.

[58] H.L. Saunders, *Welding Aluminum: Theory and Practice*, 4th ed.: The Aluminum Association, 2002.

[59] J. Campbell, *Castings*, 2nd ed. Oxford, UK: Elsevier Butterworth-Heineman, 2003.

[60] D.A. Johnson, P. Orakwe, and E. Weckman, "Experimental examination of welding nozzle jet flow at cold flow conditions," *Sci. Technol. Weld. Join.*, 2006, Vol. 11, No. 6, pp. 681-687.

[61] C.D. Donaldson and R.S. Snedeker, "A Study of Free Jet Impingement, Part 1, Mean Properties of Free and Impinging Jets," *J. Fluid Mech.*, 1971, Vol. 45, No. 2, pp. 281-319.

[62] Bruce R. Munson, F. Donald Young, and Theodore H. Okiishi, *Fundamentals of Fluid Mechanics*, 5th ed. Hoboken, NJ: John Wiley & Sons Inc., 2006.

[63] CAN/CSA – W117.2/M87, *Safety in Welding, Cutting and Allied Processes*. Toronto, ON: Can. Standard Assoc., 1987, Section 5.3.2.2.

[64] *ASM Handbook Vol. 20: Materials Selection and Design*. Materials Park, OH: ASM Int'l, 1993.

[65] G.F. Vander Voort, *Metallography Principles and Practice*. Materials Park, OH: ASM Int'l, 1999.

[66] ASTM E 92 - 82, *Standard Test Method for Vickers Hardness of Metallic Materials*. West Conshohocken, PA: ASTM Int'l, 2003.

[67] ASTM E 8M-04, *Standard Test Methods for Tension Testing of Metallic Materials*. West Conshohocken, PA: ASTM Int'l, 2004.

[68] AWS C1.1-66, *Recommended Practices for Resistance Welding*. New York City, NY, USA: American Welding Society, 1966.

[69] *Welding Handbook Volume 1*, 8th ed. Miami, FL: American Welding Society, 1991.

[70] AWS D8.14M/D8.14:2000, *Specification for Automotive and Light Truck Components Weld Quality — Aluminum Arc Welding*. Miami, FL, 2000.

[71] CAN/CSA – W59.2-M1991, *Welded Aluminum Construction*. Toronto, ON: Can. Standards Assoc., 1991.

[72] Aluminum Company of America, *Welding Alcoa Aluminum*. Pittsburgh, PA: Aluminum Company of America, 1958.

[73] Bill Christy, Personal Communications, Novelis, Kingston, ON, Sept 2009.

[74] Minitab Inc., Minitab 15, 2007, (software), State College, PA.

[75] Miller Electric. (2010, August) Miller - Gas Lens Basics for TIG (GTAW) Applications. [Online]. http://www.millerwelds.com/resources/articles/index.php?page=article122.html

[76] AWS D8-9-97, *Recommended Practices for Test Methods for Evaluating the Resistance Spot Welding Behavior of Automotive Sheet Steel Materials*. Miami, FL: American Welding Society, 1997.

[77] AWS D8.7-88, *Recommended Practices for Automotive Weld Quality – Resistance Spot Welding*. Miami, FL: American Welding Society, 1988.

[78] P. Patnaik, *Handbook of Inorganic Chemicals*, 1st ed., K. McComb, Ed. New York City, New York: McGraw-Hill, 2002.

[79] Parametric Technology Corporation, Mathcad 14.0, 2007, (software), Needham, MA.

[80] Y. Kwon and D.C. Weckman, "Analytical thermal model of conduction mode double sided arc

welding," *Sci. Technol. Weld. Join.*, 2008, Vol. 13, No. 6, pp. 539-549.